MASARYKOVA UNIVERZITA
PŘÍRODOVĚDECKÁ FAKULTA
ÚSTAV TEORETICKÉ FYZIKY A ASTROFYZIKY

Diplomová práce

BRNO 2025   BC. MICHAELA ĎURÍŠKOVÁ

Zkoumání kvantové gravitace: testy přesnosti prostřednictvím analýzy vysokoenergetických jevů

Diplomová práce

Bc. Michaela Ďuríšková

Bibliografický záznam

Bibliographic Entry

Abstrakt

Předkládáme studii zaměřenou na fenomenologii kvantové gravitace, teorie předpovídající kvantovou strukturu časoprostoru, která se projevuje na Planckově škále. Cílem této práce je hledání časových zpoždění indukovaných kvantovou gravitací v datech z gama záblesků (GRB), která mohou vznikat v důsledku modifikované propagace fotonů kvantovaným časoprostorem. Pro analýzu jsou využita data z družice Fermi Gamma-ray Space Telescope. Vytváříme dataset všech GRB s měřeným červeným posuvem, které byly detekovány družicí Fermi v období od roku 2008 do roku 2024. Pro finální vzorek 23 GRB provádíme analýzu a stanovujeme časová zpoždění mezi detektory Fermi-GBM a Fermi-LLE/Fermi-LAT v několika energetických intervalech. Analýza je provedena pomocí HERMES delays softwaru, založeného na metodě křížové korelace. Na závěr porovnáváme námi experimentálně stanovená časová zpoždění s teoretickými předpověďmi. Získané výsledky neprokazují statisticky významný důkaz časových zpoždění indukovaných kvantovou gravitací, přičemž naměřené hodnoty jsou dominovány vnitřními emisními vlastnostmi samotných GRB. Závěrem navrhujeme možná vylepšení pro budoucí studie.

Abstract

We present a study focused on the phenomenology of quantum gravity, a theory predicting the quantum structure of space-time manifesting at the Planck scale. The aim of this study is to search for quantum gravity-induced time delays in gamma-ray burst (GRB) data, arising from modified photon propagation through a quantized space-time. For the analysis, data from the Fermi Gamma-ray Space Telescope are utilized. We first create a dataset of all GRBs with known redshift detected by Fermi between 2008 and 2024. For a final sample of 23 GRBs, we conduct the analysis and estimate time delays between the Fermi-GBM and Fermi-LLE/Fermi-LAT instruments across multiple energy ranges. The analysis is performed using the HERMES delays software, based on a cross-correlation technique. Finally, we compare our experimentally estimated time delays with theoretical predictions. The obtained results show no statistically significant evidence of quantum gravity-induced time delays, with the measured values dominated by intrinsic GRB emission properties. In conclusion, possible improvements for future studies are discussed.

ZADÁNÍ
DIPLOMOVÉ PRÁCE

Akademický rok: 2024/2025

Ústav:	Ústav teoretické fyziky a astrofyziky
Studentka:	Bc. Michaela Ďuríšková
Program:	Fyzika
Specializace:	Astrofyzika

Ředitel *ústavu* PřF MU Vám ve smyslu Studijního a zkušebního řádu MU určuje diplomovou práci s názvem:

Název práce:	Zkoumání kvantové gravitace: testy přesnosti prostřednictvím analýzy vysokoenergetických jevů
Název práce anglicky:	Probing Quantum Gravity: Precision Tests via High-Energy Phenomena Analysis
Jazyk práce:	angličtina

Oficiální zadání:

The work utilises gamma-ray bursts (GRBs) to investigate quantum gravity. The research begins with a review of current quantum gravity theories and their implications. Emphasizing GRBs as prominent high-energy astrophysical phenomena, the study aims to analyze these events to uncover potential quantum gravitational effects. Observational data from GRBs will be examined using advanced analytical techniques and numerical simulations. The goal is to identify any deviations from theoretical predictions that could suggest quantum gravity signatures. The findings will be critically assessed to discuss their implications for quantum gravity theories, and future research directions and observational methods will be proposed based on the results.

Vedoucí práce:	Mgr. Samuel Kováčik, Ph.D.
Datum zadání práce:	18. 5. 2024
V Brně dne:	4. 4. 2025

Zadání bylo schváleno prostřednictvím IS MU.

Bc. Michaela Ďuríšková, 19. 5. 2024
Mgr. Samuel Kováčik, Ph.D., 1. 11. 2024
Mgr. Dušan Hemzal, Ph.D., 27. 11. 2024

Acknowledgement

In the first place, I would like to express my sincere gratitude to my supervisor, Samuel Kováčik, for his continuous support, guidance, and valuable insights throughout the course of this thesis. Special thanks go to the entire High Energy Astrophysics group for the opportunities they have provided me. Thanks to their support, I was able to gain valuable knowledge about high-energy phenomena and contribute to operations on the GRBAlpha satellite.

My sincere thanks go to Wladimiro Leone. Thank you for granting me the opportunity to be the first user of the delays software. I am also especially thankful to Luciano Burderi and Anastasia Tsvetkova for their insightful feedback and for always being available for discussion and advice. The collaboration with the HERMES team helped me grow both professionally and personally as a researcher.

I would also like to sincerely thank the organizers and lecturers of the first Quantum Gravity School held in Bad Honnef, Germany. Their inspiring lectures and discussions significantly deepened my understanding of the field of experimental quantum gravity.

I am deeply grateful to my family and loved ones for their unwavering love, understanding, and support throughout my studies. My heartfelt thanks go to Lukáš — your presence and constant support have meant more to me than words can express.

Prohlášení

Prohlašuji, že jsem svoji diplomovou práci vypracovala samostatně pod vedením vedoucího práce s využitím informačních zdrojů, které jsou v práci citovány.

Brno 5. května 2025

. . . .
Bc. Michaela Ďurísková

Contents

Introduction

Understanding the nature of space-time remains one of the main challenges in modern physics. While Einstein's general relativity successfully describes the universe on cosmological scales, quantum mechanics explains the behavior of microscopic particles through probabilistic wave functions and the uncertainty principle. Even if the two theories work perfectly separately, unifying them appears, for now, to be impossible. Various approaches attempt to construct a theory combining the two worlds, like string theory, the most prominent example of them all. Despite significant theoretical progress and the development of numerous approaches, a complete theory of quantum gravity has not been found.

The idea of the phenomenological quantum gravity has arisen in recent years. Quantum gravity phenomenology aims to prove quantum gravity through experiments, despite the lack of knowledge of the fundamental theory. According to quantum gravity, space-time possesses an inner, quantum structure. This underlying structure may give rise to a modified dispersion relation and subsequently, to potentially observable effects. The difficulty lies in the near impossibility of detecting such effects, as they are expected to manifest at the Planck scale, far beyond the reach of current laboratory experiments. Fortunately, the universe itself provides natural sources capable of testing these effects, as they reach enormous energies, such as gamma-ray bursts, pulsars, or active galactic nuclei, and various cosmic messengers, including photons, neutrinos, or gravitational waves. These astrophysical sources, together with their associated cosmic messengers, offer a unique opportunity to explore and search for quantum gravity signatures.

In this work, we focus on the search for quantum gravity-induced time delays in the arrival times of photons from cosmological gamma-ray bursts. By analyzing the arrival times of photons of different energies and various redshifts, we aim to observe any deviation from standard physics and therefore, contribute to the ongoing effort to search for evidence of the quantum nature of space-time.

Firstly, we introduce the theoretical background of quantum gravity and its phenomenological models and observable effects. The second chapter presents gamma-ray bursts as promising astrophysical sources for testing these effects. The following chapter is dedicated to an overview of relevant gamma-ray detectors and their capabilities. The methodology used to identify time delays in the gamma-ray bursts data, along with the data analysis process, is presented in the fourth and fifth chapters. The final chapter presents the results of the analysis and compares them with theoretical expectations. Lastly, we discuss possible interpretations of the obtained results and suggest directions for future improvement.

Quantum theory of gravity

1.1 Successes of general relativity and the standard model

General relativity, a theory of space and time itself describing gravity using differential geometry, was formulated by Einstein more than 100 years ago, in 1915 (Einstein, 1915). Together with quantum physics, the theories are considered as two keystones of modern physics. An essential finding of the last century was the description of space-time with Einstein's field equations (Clifton et al., 2012):

$$G_{\mu\nu} = \frac{8\pi G}{c^4} T_{\mu\nu},\tag{1.1}$$

where $T_{\mu\nu}$ is the energy-momentum tensor, which ensures the inclusion of matter and energy in the field equations, and $G_{\mu\nu}$ is the Einstein tensor. $G_{\mu\nu}$ may be also rewritten as:

$$G_{\mu\nu} = R_{\mu\nu} - \frac{1}{2} g_{\mu\nu} R,\tag{1.2}$$

where $g_{\mu\nu}$ is the metric describing the geometry of given space-time, $R_{\mu\nu}$ is a Ricci tensor derived from the Riemann tensor, $R_{\mu\nu} = R^{\alpha}_{\mu\alpha\nu}$. The Riemann tensor expresses the curvature of space-time, thereby reflecting the presence of the gravitational field. The Riemann tensor can be expressed in terms of the Levi-Civita connection (Christoffel symbols) (Misner et al., 1973). Lastly, the Ricci scalar R represents the scalar curvature of space-time (Wald, 1984).

The formulated theory of gravity, together with the ΛCDM model describing the structure and evolution of our universe (Abdalla et al., 2022; Saridakis et al., 2021), has experienced numerous successes in recent years. The most remarkable tests validating general relativity include the observation of the shadow of a supermassive black hole in the center of the elliptical galaxy M87 caused by gravitational light bending (Event Horizon Telescope Collaboration et al., 2019) or the observation of gravitational waves from a black hole merger by LIGO and Virgo (Abbott et al., 2016). Both of these discoveries were awarded the Nobel Prize in Physics.

Although the theory of gravity and quantum mechanics separately achieved great success in the era of modern physics, when we try to implement gravity into the quantum world, or vice versa, mathematics breaks down. Physicists have been striving to unravel this quantum gravity problem for more than 90 years (Amelino-Camelia, 2002), but so far, with no success.

1.2   The road to quantum gravity

Over the past few decades, physicists have developed various mathematical models for the quantum theory of gravity. Among the most well-known approaches to quantizing general relativity are string theory, which treats particles as vibrating strings, and provides a quantum model of graviton (Barbón, 2004), or loop quantum gravity, which replaces strings with discrete loops and offers a non-perturbative, background-independent formulation of general relativity, including its conventional matter couplings (Rovelli, 1998). Other quantum-gravity approaches include the generalized uncertainty principle (Maggiore, 1993), asymptotic safety (Niedermaier & Reuter, 2006) or spin foams (Perez, 2013). Rainbow gravity assumes the geometry, speed of light, matter fields, Newtonian gravitation constant, and mass are dependent on the energy (Junior et al., 2020). The causal set theory proposes a discrete space-time, with the space-time continuum substituted by locally finite causal sets (Surya, 2019). The noncommutative approach implements Heisenberg's uncertainty principle and thereby prohibits the exact localization of space-time points (Doplicher et al., 1995; Kováčik & Prešnajder, 2013).

All the different approaches to quantum gravity share one key feature. They all are expected to become relevant at the Planck scale, in other words, at energies in the order of Planck energy $E_{\text{Pl}} = 1.22 \times 10^{28}$ eV or Planck length, $l_{\text{Pl}} = 1.6 \times 10^{-35}$ m (Sarkar, 2002). This scale, derived from the four fundamental physical constants, is expected to be a threshold for unveiling the quantum nature of space-time.

1.3   Quantum gravity phenomenology

The phenomenology of quantum gravity strives for a new approach by combining the theory with experiments, despite the lack of information about the fundamental theory (Amelino-Camelia, 2002). Because we predict that quantum space-time should manifest at the Planck scale, the most pertinent tools to experimentally examine quantum gravity are the ultra-high-energy cosmic messengers, such as cosmic rays, neutrinos, gamma rays (this topic is further explored in the following chapter), or even gravitational waves (Alves Batista et al., 2023). This requires the mutual interest in collaboration between theorists and experimentalists.

The hypothesis of quantum space-time is frequently compared to a crystal lattice to simplify visualization, however, the actual structure is expected to be far more sophisticated. When light passes through a lattice, photons with distinct energies propagate differently due to their interaction with the medium. We can also utilize another analogy applied in our everyday world. Imagine a newly paved asphalt road. When driving a car, the journey appears smooth and flat. However, if we change the scale and place a toy car on the same road, its irregularities become apparent, revealing its inner structure. The large wheels barely notice the bumps, while the small ones are strongly affected. Similarly, cosmic photons propagate through space-time, and if they possess sufficiently short wavelengths, the microscopic structure of quantum space-time will affect their propagation.

1.3.1 Phenomenological models

After introducing the fundamental mathematical models of quantum gravity in the section 1.2, we will now focus on and summarize some of the phenomenological frameworks and their predictions, striving to derive the observational consequences of quantum gravity. With the help of work by Addazi et al. (2022), the models (among others) include:

- Lorentz invariance violation (LIV): General relativity and the standard model are governed by assuming symmetries, whether it is space-time or internal symmetries. On the other hand, quantum gravity approaches tend to deform them (Amelino-Camelia et al., 2011), or directly break them (Hořava, 2009). The form of the operators, previously influenced by the symmetries, will change. Subsequently, by breaking or violating the Lorentz invariance, one can derive several modifications of phenomena relevant to astrophysics, such as modification of particle interactions or modification of their time of flight. From now on, we will adopt the LIV as our phenomenological model in this work.

- Doubly (deformed) special relativity (DSR): DSR theories present relativistic transformations between inertial observers. They preserve the invariance of the speed of light, and introduce an invariant Planck scale, making both observer-independent (Amelino-Camelia & Ahluwalia, 2002). Their results also include deformed dispersion relation, and deformed energy-momentum conservation, as stated in Garay (1995) and Kowalski-Glikman & Nowak (2003).

- Generalized uncertainty principle (GUP): This theory assumes the Heisenberg uncertainty principle breaks down at the Planck scale (Das & Vagenas, 2009). GUP theory proposes the modified uncertainty principle, which should be valid at all scales (Maggiore, 1993). Subsequently, the modification results in a modified dispersion relation, and a change in photon velocities, where superluminal motions are allowed (Majhi & Vagenas, 2013).

- Noncommutative geometry: Noncommutative geometry applies to spaces where the simplifying assumption of coordinate commutativity is not valid (Connes, 2007). The theory assumes the noncommutative space-time operators are ruled by a parameter related to the Planck scale, and provides mathematical formulations of space-time at this scale, where it cannot be represented as a differentiable manifold (Addazi et al., 2022).

1.3.2 Planck-scale modified dispersion relation

The Lorentz invariance violation-induced modified dispersion relation, along with the two most prominent potential observable effects, time delays of photons and threshold anomalies, was previously introduced in the author's bachelor thesis (Ďuríšková, 2023). Nevertheless, in the following two subsections, we will revisit the key concepts and equations of the aforementioned phenomena. We emphasize that for a better interpretation of the expressions, the four fundamental physical constants c, G, h, and k_b are equal to 1.

Several quantum gravity phenomenological models, including the deformation/violation of the Lorentz invariance approach, result in the modification of the energy-momentum dispersion relation. The standard dispersion relation,

$$E^2 = m^2 + \vec{p}^2, \tag{1.3}$$

is deformed and acquires the following form (for massless particles, mass $m = 0$) (Amelino-Camelia, 2002):

$$E^2 = m^2 + \vec{p}^2 + f(\vec{p}^2, E, m; L_{\text{Pl}}), \tag{1.4}$$

where L_{Pl} is the Planck length. Hence, one can see that deviations from the standard model of physics are dependent on the Planck scale. The velocity of photons, derived from the modified in-vacuo dispersion relation, may be written as (Amelino-Camelia et al., 1998):

$$v_\gamma = c \left(1 - \eta \frac{E}{E_{\text{Pl}}} \right), \tag{1.5}$$

where E_{Pl} is the Planck energy and η decides whether we consider a superluminal ($\eta = -1$) or subluminal ($\eta = +1$) effect. In other words, the in-vacuo dispersion relation is not compatible with Einstein's second special relativity postulate about the constant speed of light for all inertial observers. LIV proposes the breakdown of special relativity at the Planck scale.

Similarly, in noncommutative approaches, thus in space-times where space-time coordinates do not commute:

$$[x_\mu, x_\nu] = i\theta_{\mu\nu}, \tag{1.6}$$

the modified dispersion relation eventually adopt the same structure (Amelino-Camelia, 2005):

$$m^2 \simeq E^2 - \vec{p}^2 - \lambda E \vec{p}^2. \tag{1.7}$$

This clearly demonstrates that different approaches lead to an analogous dispersion relation. The modified dispersion relation, written in terms of the free Hamiltonian and some additional assumptions, has the following form:

$$\hat{H}_0 = \frac{1}{m\lambda^2} \left(1 - \sqrt{1 - \frac{\lambda^2 \hat{p}^2}{1 + \lambda^2 \hat{p}^2}} \right) = \frac{\hat{p}^2}{2m} - \frac{3\hat{p}^4}{8m}\lambda^2 + O(\lambda^4), \tag{1.8}$$

where λ, included in both 1.7 and 1.8 expressions represent a deformation related to the Planck scale.

1.3.3   Quantum space-time observable effects

Because quantum space-time phenomenology postulates the existence of a modified dispersion relation, this modification leads to quantum gravity effects on cosmic messengers. Two of the most prominent observable consequences of quantum space-time are anomalous threshold reactions and arrival time delays of cosmological particles. The following subsection will focus in greater detail on arrival time delays.

In case of anomalous threshold reactions, this framework aims to explain the detection of ultra-high energy photons, such as those observed in the GRB 2201009A event, with energies on the order of teraelectronvolts (TeV) (Huang et al., 2022). According to the standard model, the detection of such ultra-energetic photons should be significantly suppressed due to their annihilation, because of interactions with the cosmic microwave background (CMB) or extragalactic background light (EBL) photons (Li & Ma, 2023). The quantum space-time modification of the threshold relation proposes an explanation for the observation of these ultra-high-energy photons. A more detailed view of the phenomenological aspects can be found in the author's co-authored publication Kováčik et al. (2025).

Time delays for photons in-vacuo

A significant consequence of the modified dispersion law is the energy-dependent arrival time delays for cosmic messengers. The formula for the Lorentz-violation-induced time delay of a cosmological massless high-energy particle was introduced for the first time in the work of Jacob & Piran (2008).

Assuming the simultaneous emission of different-energy photons from the astrophysical source and a flat ($\Omega_k = 0$), homogenous, isotropic, expanding space-time filled with matter density Ω_m and dark energy density Ω_Λ (Ellis et al., 2000), described by the Friedmann-Lemaître-Robertson-Walker (FLRW) metric:

$$ds^2 = -c^2 dt^2 + a^2(t) \left[\frac{dr^2}{1 - kr^2} + r^2 \left(d\theta^2 + \sin^2\theta \, d\phi^2 \right) \right], \tag{1.9}$$

where $a(t)$ is the scale factor, the arrival time difference formula acquires the following form (Alves Batista et al., 2025):

$$\tau_{\mathrm{QG}} = \eta \, \frac{1+n}{2H_0} \frac{E_h^n - E_l^n}{E_{\mathrm{QG}}^n} \int_0^z \frac{(1+z')^n}{\sqrt{\Omega_m (1+z')^3 + \Omega_\Lambda}} \, dz', \tag{1.10}$$

where H_0 is the Hubble parameter at present, E_{QG} is the expected Planck energy, E_h and E_l is the energy of high/low energy redshifted photon detected by the detector at present, n is the order of quantum gravity correction and η has the same meaning as in the relation 1.5, being positive for subluminal and negative for superluminal propagation.

The search for time delays in astrophysical GRB data will be the main focus of the experimental part of this work, considering the linear $n = 1$ quantum gravity correction.

Gamma-ray bursts as quantum gravity tools

2.1 Introduction to gamma-ray bursts

Gamma-ray bursts (GRBs) are very short and intense non-repeating flashes of gamma-ray photons (Piran, 1999), discovered unexpectedly in 1967 by VELA satellites controlling the nuclear test ban treaty (Klebesadel et al., 1973). With the total energy release of 10^{51} erg (Frail et al., 2001), GRBs are considered one of the universe's most energetic events.

After their discovery in the late sixties, the scientific community developed numerous ideas and models about the origin of GRBs. By the end of the 1980s, the idea of GRBs originating in the galactic halo of the Milky Way dominated (Fishman et al., 1978; Beurle et al., 1981). A decade later, the Burst and Transient Source Experiment (BATSE) onboard the newly launched Compton Gamma-Ray Observatory found that gamma-ray bursts are distributed isotropically, yet not homogeneously. The distribution is uniform to large distances, but then the number density decreases (Meegan et al., 1991; Fishman et al., 1991). Finally, the proof of their cosmological origin was delivered after the launch of the Italian-Dutch BeppoSAX satellite (Costa et al., 1997), which detected for the first time afterglows from several GRBs (Metzger et al., 1997; Kulkarni et al., 1998). Consequently, it was possible to determine positions in the sky and associate them with galaxies, proving their extragalactic origin.

2.2 Flavors of GRBs

By analyzing multiple light curves, one can categorize GRBs into two types based on their time duration and spectral hardness (Kouveliotou et al., 1993). The plot 2.1 presented by Kouveliotou et al. (1993) clearly illustrates the bimodal distribution of detected GRBs. In the following two subsections, we will explore this classification in more detail. However, beyond these two well-known subgroups, recent studies propose additional subcategories, as presented, for example, in the work of Mészáros & Řípa (2019).

2.2.1 Short GRBs

An essential distinguishing feature of short GRBs is their duration, defined by T_{90} being less than 2 seconds. Here, T_{90} stands for the time interval during which 90% of the total counts are detected, centered in the middle of the burst. It is believed that they originate

from compact object binary mergers (neutron star-neutron star or a neutron star-black hole merger), although a number of questions still remain unanswered (Berger, 2014). However, as stated in Abbott et al. (2017), on August 17, 2017, the short GRB 170817A was for the first time associated with the gravitational wave event GW170817, providing direct evidence of binary neutron star mergers as the progenitor of short GRBs.

Another key characteristic of short GRBs is their harder non-thermal spectra in comparison with soft, non-thermal spectra of long GRBs. Various approaches in the past proposed to associate short GRBs with soft gamma-ray repeaters, but the idea was swept away due to differences in the hardness of the spectra (Kouveliotou et al., 1987; Berger, 2014).
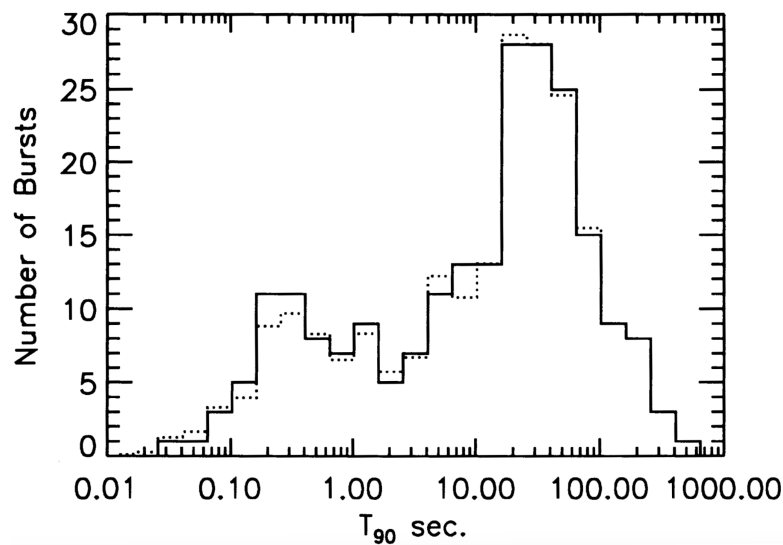
Figure 2.1: The plot from Kouveliotou et al. (1993) is showing a clear bimodal distribution of T_{90} for 222 GRBs. The dividing line between the two types is traditionally at $T_{90} = 3$ seconds.

2.2.2 Long GRBs

Long GRBs are, on the other hand, named after their duration of $T_{90} > 2$ seconds. They are often associated with active star formation (only in blue star-forming galaxies). The progenitor is a core collapse of a massive star (Woosley, 1993).

As presented in the work of Zhang (2025), recent findings of unusual GRBs complicate the distinction between the two categories and eliminate the possibility of a clear separation. One of the examples is a short-duration GRB 200826A with a sharp 1-second pulse but associated with a collapsar (Ahumada et al., 2021). Another example is a long GRB 211211A characterised by main emission lasting ~ 13 seconds and extended emission with duration ~ 55 seconds, but surprisingly associated with a kilonova (Rastinejad et al., 2021).

2.3 The fireball model

The fireball model is a widely adopted model used to describe the formation of a GRB. The fundamental component is the hidden inner engine, which can be, according to our current knowledge, either a core-collapse supernova or a binary merger, as we described in the previous subsections. The GRB is produced due to dissipation of the kinetic energy of an ultrarelativistic flow from the engine (Piran, 2004). The whole phenomenon can be divided into two parts. The prompt emission, or in other words, the production of the GRB itself, and the afterglow, which generates photons of longer wavelengths. We will now focus on the two parts of the phenomenon in more detail.

The formation of a gamma-ray burst during the prompt phase is caused by the energy dissipation inside the ultrarelativistic inhomogeneous outflow. The shells of ejected material have different Lorentz factors, causing the shells to collide with each other and resulting in the internal shock emitting gamma-rays and other lower-energy rays, usually X-rays (Piran, 2004). The situation is well illustrated in figure 2.2. Although this description of the prompt emission is broadly accepted, it is important to emphasize that besides this matter-dominated model, different models of prompt emission also exist. For instance, the electromagnetic model of GRBs applies a magnetic field as the main mechanism in the dynamics of the ejecta (Lyutikov & Blandford, 2003). Various models are discussed in detail in the work of Zhang (2014).

Afterglow is characterised by the collision of the slowing down shells of the ejecta with the surrounding medium, creating an external shock. This process is accompanied by the emission of lower energy photons, including X-ray, optical, and radio (Sari et al., 1998; Sakamoto et al., 2007). The X-ray counterpart comes first and is the most prominent. The first X-ray afterglow was discovered by the Beppo-SAX satellite (Costa et al., 1997). The optical and infrared afterglow then comes hours to days after. The detection of the afterglow is important for the position identification of the host galaxy of the burst, and therefore the estimation of the burst's redshift (Piran, 1999, 2004).
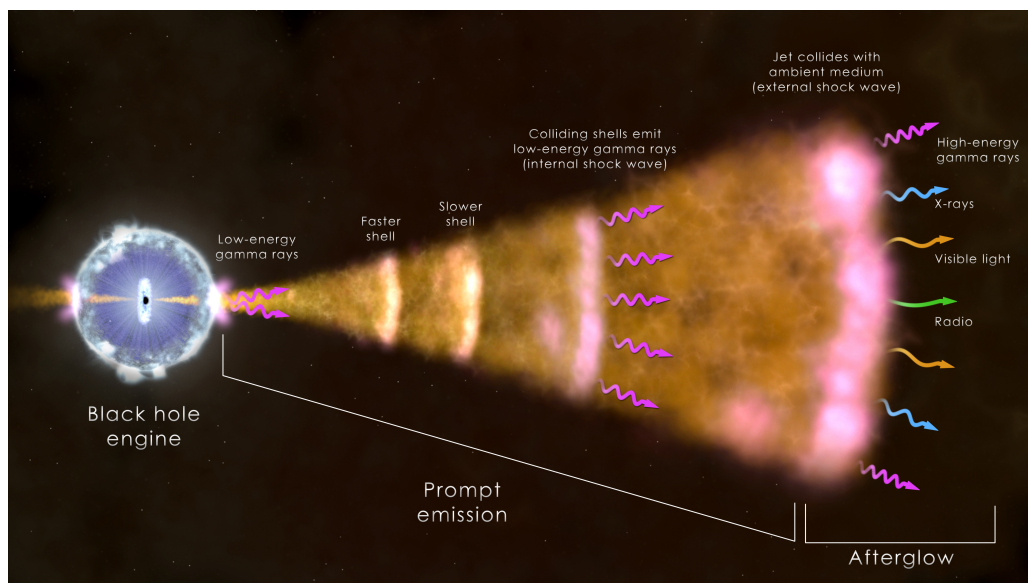

Figure 2.2: A schematic illustration of the fireball model. Image obtained from: NASA [e1]

2.4 Important plots

To analyze various types of GRBs observed in recent years, it is essential to visualize the detected and measured properties through graphical representations, enabling a more comprehensive interpretation. This short section provides an introductory overview of the key plots employed in this study, especially in the experimental part in the second half of the thesis. The two important plots are:

- **Light curve** – is the photon flux of a certain energy range plotted as a function of time, to see the temporal evolution of the emission. Usually, for detectors counting individual photon events (e.g., GRBAlpha, Fermi Gamma-ray Space Telescope), the flux is expressed as a count rate (counts per second), since these instruments detect discrete times of arrival of photons. An example of a light curve for a recent GRB 250204B detected by GRBAlpha can be found in Duriskova et al. (2025).
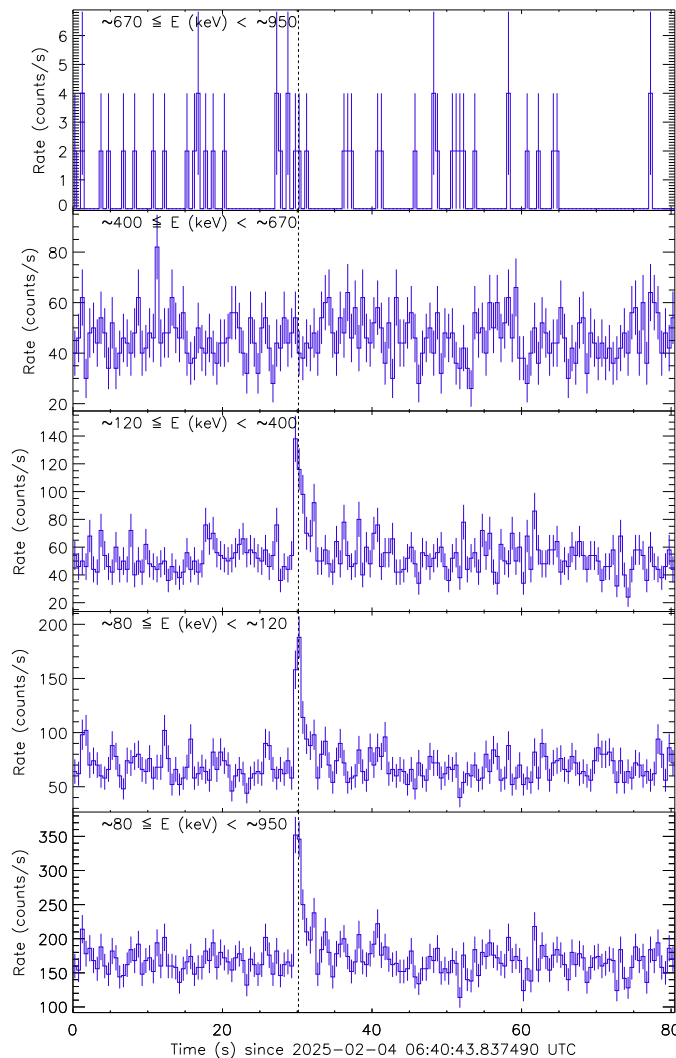
**Figure 2.3:** Light curves for 4 different energy bands of GRB 250204B detected by GRBAlpha nanosatellite (Duriskova et al., 2025). The lowest plot shows a light curve of the whole energy range detectable by GRBAlpha.

- **Counts spectrum** – The energy spectrum is presented as photon flux as a function of energy and is often characterised by Band function ([Band et al., 1993](#)):

$$N(\nu) = N_0 \begin{cases} (h\nu)^\alpha \exp\left(-\frac{h\nu}{E_0}\right), & \text{for } h\nu < H, \\ ([\alpha - \beta)E_0]^{\alpha-\beta}(h\nu)^\beta \times \exp(\beta - \alpha), & \text{for } h\nu > H, \end{cases}$$

where $H \equiv (\alpha - \beta)E_0$. In contrast, the counts spectrum represents the raw, unmodified plot of detected photon counts as a function of detected energy. It is obtained directly from the instrument without any correction. The example of a counts spectrum for GRB 221009A detected by GRBAlpha is shown in figure [2.4](#) ([Řípa et al., 2023](#)). One can also ask how the spectral energy distribution (SED) differs from the aforementioned expressions. SED is a broader concept that combines measurements across multiple wavelength bands (radio, optical, X-ray, gamma-ray, etc.) to represent the total energy output of a source across the electromagnetic spectrum.
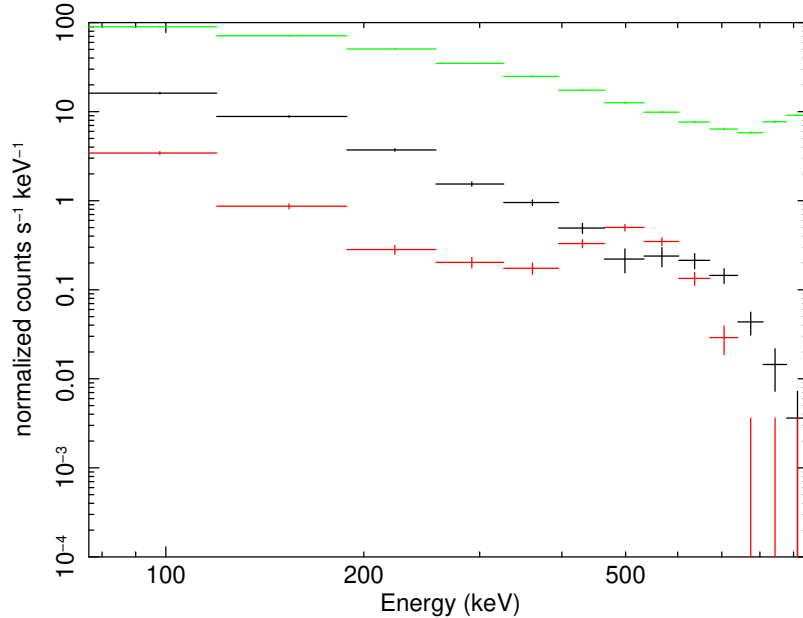
Figure 2.4: Example of a counts spectrum of GRB 221009A measured by GRBAlpha. In black is shown the detected counts spectrum minus the background, in red the background, and in green the detected count spectrum after subtracting the background, revealing spectral hardening at the highest energies around the GRB peak. ([Řípa et al., 2023](#))

2.5 GRBs as a window to quantum gravity

To experimentally probe quantum gravity features, we need to reach scales as close to the Planck scale as possible. In other words, the energy in the orders of Planck energy ($\sim 10^{28}$ eV) ([Planck, 1900](#)) must be achieved in order to uncover and potentially study the quantum nature of space-time. This remains an unattainable task for state-of-the-art particle accelerators we currently have, such as the Large Hadron Collider, which probe

energies in the orders of tens of TeV, well below the Planck energy scale (Kováčik et al., 2025). Fortunately, high-energy transient events like GRBs allow us to search for quantum gravity in the sky, as they present some of the most energetic events observed in the universe (Piran, 1999). While their energies do not reach the Planck energy scale either, they have one significant advantage – their cosmological distance. Deviations from the standard model of classical physics, like the presented dispersion for photons *in-vacuo*, are expected to be minuscule according to theoretical predictions. However, the infinitesimal effect accumulates over immense cosmological distances (Amelino-Camelia et al., 1998).

The interest in quantum gravity phenomenology rose in the scientific community after the recent detection of exceptionally bright GRB 221009A (Veres et al., 2022; Huang et al., 2022), which is considered to be a once-in-10,000-year event (Burns et al., 2023). Since October 9, 2022, open questions regarding the possibility of observing such an energetic event without modifying the standard model of physics remain unanswered. Various scientific papers attempt to search for quantum gravity-induced deviations in the GRB 221009A data (e.g., in the paper of Zhu & Ma (2023) or the author's bachelor thesis Ďuríšková (2023)) or attempt to explain the observation of such a burst with the threshold anomaly approach, as in the paper of Li & Ma (2023).
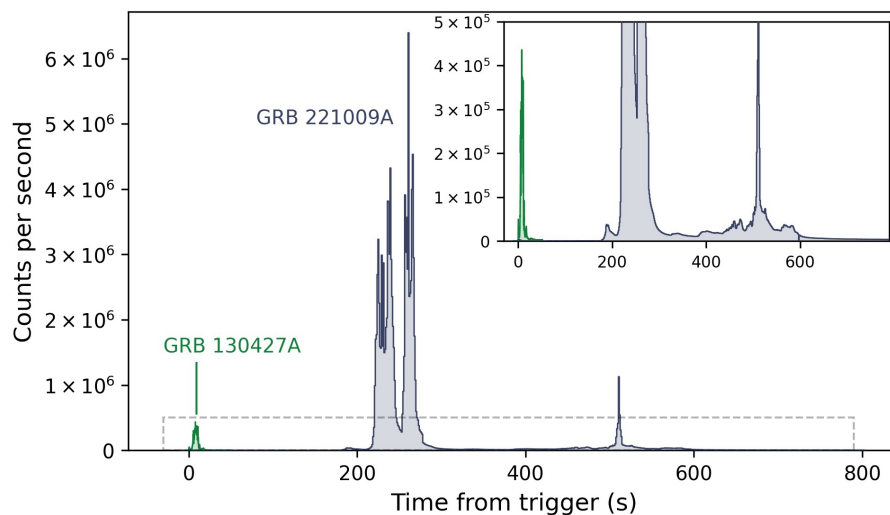
Figure 2.5: GRB 221009A, detected on October 9, 2022, compared to the previous record holder, GRB 130427A. Image obtained from: Adam Goldstein, USRA [e2]

2.5.1 Intrinsic lags problem

Spectral lags are energy-dependent time delays arising from the intrinsic spectral evolution of a GRB. They are believed to originate at the source, causing photons of different energies to be emitted at distinct times. In light curves, the phenomenon is presented as a peak migration and pulse broadening at lower energies (Norris et al., 2000). The phenomenon was first introduced 30 years ago by Cheng et al. (1995). They analyzed light curves from the BATSE Large Area Detector in the 25–50 keV and 100–300 keV energy bands using a cross-correlation technique, finding that low-energy photons exhibit a time delay relative to higher energy photons. Since then, numerous studies have aimed to understand the origin

of spectral lags (Norris et al., 2000; Chen et al., 2005).

In general, two types of lags can be observed. Positive lags result from low-energy photons arriving later than high-energy ones and may originate from electron cooling (Schaefer, 2004), Compton reflection (Ryde, 2005), or the relativistic curvature effect (Shen et al., 2005; Qin et al., 2004; Peng et al., 2011). On the other hand, negative lags are much more rare, and it is believed that they are caused by inverse Comptonization in a hot medium (Peng et al., 2011; Chakrabarti et al., 2018). Moreover, according to Norris et al. (2001), short GRBs appear to have a zero spectral lag. We note that, although the scientific community strives to explain the spectral lag phenomenon, the question of its origin remains unanswered to this day.

The reader may now deduce that detecting and confirming quantum gravity-induced time delays is a challenging task, primarily due to the contribution of other effects, such as the aforementioned spectral lag phenomenon. Subsequently, the total observed delay can be expressed as the sum of two components:

$$\tau_{\text{total}} = \tau_{\text{QG}} + \tau_{\text{intrinsic}}. \tag{2.11}$$

At first glance, one might assume that separating the delay caused by the quantum structure of space-time from intrinsic delay is impossible. However, a key distinguishing feature is that quantum gravity-induced time delays depend on redshift, while intrinsic spectral lags do not. Consequently, if time delay measurements are available across a range of redshifts, the two effects can be disentangled.

2.5.2 Other suitable astrophysical sources and messengers

It is important to emphasize that gamma-ray bursts are not the only gamma-ray sources at cosmological distances that the universe provides. Other suitable sources include active galactic nuclei (AGNs) and pulsars. AGNs provide high-energy gamma rays in the orders of hundreds of GeV, and TeV flares. Thanks to this and their rapid flux variations and cosmological distances, AGNs present an effective option for searching for quantum gravity features (Wei & Wu, 2021; Levy et al., 2022). Pulsars, on the other hand, offer the advantage of stability and therefore a precise periodic flux variation. Subsequently, the longer we observe the source, the more the sensitivity to LIV is improved (Wei & Wu, 2021). An example of constraining quantum gravity features using Crab pulsar can be found in the work of Gaug et al. (2017).

Besides gamma rays, electromagnetic radiation in general, LIV may also be investigated through the observation of other cosmic messengers. Neutrinos are considered as privileged messengers, due to their ultra-high energy, electric neutrality, and weak interaction. Therefore, they reach us from cosmological distances without being affected by background fields. Moreover, as they're not affected by any side effects, they point directly to the source. Cosmic rays, on the other hand, are positively charged high-energy particles, so their trajectories may be diverted by intergalactic and galactic magnetic fields. This makes it more difficult to point to their sources, compared to neutrinos or gamma rays (Addazi et al., 2022).

GRB detectors

To study potential manifestations of quantum gravity features in GRBs, it is important to choose a suitable observational instrument. A gamma-ray detector should not only possess appropriate technical characteristics, such as a broad energy range or a high temporal resolution, but should also provide convenient access to GRB data. In this chapter, we provide a short overview of the currently operational missions both in space and on the ground, sensitive to the high-energy gamma-ray part of the electromagnetic spectrum. We compare the key attributes of these detectors and comment on their relevance for utilizing the instrument for searching for quantum gravity effects. This comparison serves as the basis for justifying the selection of the datasets used in this thesis, and helps identify which missions are suitable for searching for quantum gravity features using GRB observations.

3.1   Space-based telescopes

One of the main advantages of gamma-ray telescopes located in space is their ability to directly detect astrophysical transients, in contrast to ground detectors, where the interaction with the Earth's atmosphere needs to be considered. Among the currently operating gamma-ray missions in space, the Fermi Gamma-ray Space Telescope (Thompson & Wilson-Hodge, 2022) and the Neil Gehrels Swift Observatory, developed by NASA and launched in 2004 (Gehrels et al., 2004), represent the most prominent examples of gamma-ray instruments. The International Gamma-Ray Astrophysics Laboratory (INTEGRAL) (Winkler et al., 2003), operated by the European Space Agency, also belonged to this group of leading gamma-ray missions. On March 4, 2025, the mission officially ended after more than 22 years of operation (Ferrigno, 2025).

In addition to these missions, several other gamma-ray space observatories contribute to GRB science. Other missions include, for instance, AstroSat, India's first telescope capable of observing a broad interval of wavelengths (Singh et al., 2014), Gravitational wave high-energy Electromagnetic Counterpart All-sky Monitor mission (GECAM), composed of two microsatellites launched in December 2020, and one additional microsatellite launched in July 2022 (Wang et al., 2024), the Space Variable Objects Monitor (SVOM), which is a constellation of four space and three ground instruments, developed by Chinese-French collaboration (Bernardini et al., 2021), Konus, composed of two large scintillators onboard Wind spacecraft (Aptekar et al., 1995), Calorimetric Electron Telescope (CALET), an experiment for high-energy astroparticle physics developed by Japanese-Italian-American collaboration and positioned on International Space Station (Asaoka et al., 2019), and the smallest gamma-ray observatory, GRBAlpha (Pál et al., 2023). In the following

subsections, we introduce two of the instruments mentioned above, Fermi as an example of a large-scale, high-precision observatory, and GRBAlpha, as a demonstration of CubeSat capabilities. These are presented together with the third and newest mission, HERMES, launched in March 2025, which represents a novel approach based on constellations of nanosatellites.

3.1.1 GRBAlpha

The GRBAlpha CubeSat was launched in March 2021 and continues to operate successfully to this day. Due to its compact size, with dimensions of 10 centimeters, it is considered one of the smallest astrophysical observatories. The detector of GRBAlpha serves as an in-orbit demonstration for the future CubeSats Applied for Measuring and Localising Transients (CAMELOT) mission.

The gamma-ray detector is composed of a thallium-activated cesium-iodine (CsI(Tl)) crystal scintillator, wrapped in the Enhanced Specular Reflector (ESR) reflective foil. The detection principle of a scintillator is based on the absorption of a gamma-ray photon by the crystal, which leads to the excitation of atoms. These subsequently undergo spontaneous de-excitation, generating a flash of light. The light from the scintillation is then detected by Multi-Pixel Photon Counter (MPPC) silicon photomultipliers (SiPMs), attached to the crystal in two arrays. The resulting analog signal is then converted by a digital-analog converter (DAC), and the data acquisition is ensured thanks to a field programmable gate array (FPGA) and the main microcontroller unit (MCU) (Pál et al., 2020, 2023).

GRBAlpha possesses an energy range from 80 keV to 950 keV and provides a time resolution of 1 second. While GRBAlpha successfully demonstrates that the smallest CubeSats can detect very high-energy and exotic phenomena, such as GRBs, its energy and temporal characteristics are not sufficient for studying potential quantum gravity effects. This result was originally obtained as part of the author's bachelor's thesis (Ďuríšková, 2023).

3.1.2 Fermi Gamma-ray Space Telescope

As detailed in the work of Thompson & Wilson-Hodge (2022), the Fermi Gamma-ray Space Telescope, previously known as the Gamma-ray Large Area Space Telescope (GLAST), was launched on June 11, 2008, into low-Earth orbit with the main objective of surveying the gamma-ray sky. The telescope consists of two separate instruments, the Gamma-ray Burst Monitor and the Large Area Telescope. We focus on the two GRB detection instruments in the following subsections. It is important to note that both instruments are designed with extensive fields of view, subsequently allowing them to observe the whole sky. The Large Area Telescope observes with a cadence of approximately three hours, while the Gamma-ray Burst Monitor observes with a cadence of around one hour.

Large Area Telescope (LAT)

Fermi-LAT covers energy ranges from 20 MeV up to at least 300 GeV. The detection principle of this instrument lies in the conversion of a gamma ray into an electron-positron pair, making the LAT a pair-conversion telescope. The detector can be divided into three

main components. Firstly the precision converter-trackers, which are pairs of single-sided silicon strip detectors and have the shape of 16 towers in a 4×4 array. Here, the incident high-energy gamma ray converts into an electron-positron pair. The instrument then reconstructs the arrival direction of the gamma ray by tracking the particles. The measurement of the detected energy and discrimination of background is performed by the calorimeter, where the modules are organized in the same 4×4 grid of 16 towers. Every calorimeter module consists of 96 CsI(Tl) crystals. The last subsystem is the anticoincidence detector. It is designed to reject charged-particle background, subsequently, its key requirement is to achieve high detection efficiency of charged particles. The data is then collected and processed by the Data Acquisition System (DAQ). A notable feature of the Fermi-LAT instrument is its time resolution of one microsecond (Thompson & Wilson-Hodge, 2022; Atwood et al., 2009).

Finally, it is important to note that the extended data of lower LAT energies, ranging from 3 MeV to 10 GeV, is referred to as the LAT Low-Energy data (LLE).

Gamma-ray Burst Monitor (GBM)

The primary purpose of the GBM scientific instrument is to extend the energy range of Fermi's Large Area Telescope to lower energies and to calculate burst locations onboard. This enables the spacecraft to reorient itself and observe emissions from bright bursts using the more energetic LAT instrument (Thompson & Wilson-Hodge, 2022).

Similarly to GRBAlpha, the GBM also employs the scintillation crystal technique for the detection of GRBs. Specifically, the GBM consists of twelve thallium-activated sodium iodide (NaI(Tl)) detectors, grouped by three detectors and located at each corner of the spacecraft, as well as two bismuth germanate (BGO) detectors, located each on opposite sides of the spacecraft. NaI(Tl) scintillators have an energy range spanning from 8 keV to 1 MeV and are primarily utilized to find the GRB direction. On the other hand, BGO detectors cover energies from 200 keV to approximately 40 MeV, which overlaps with the energy range of both NaI(Tl) detectors and the LAT instrument and therefore are used for cross-calibration purposes (Meegan et al., 2009; Thompson & Wilson-Hodge, 2022). All the locations and orientations of both types of GBM detectors are illustrated in figure 3.1.

The visible scintillation light, produced as a result of the interaction of high-energy gamma photons with the scintillator material and the production of secondary particles that excite atoms in the scintillator material, is converted due to photomultiplier tubes (PMTs) into an electric signal. The signal is then processed by the Data Processing Unit (DPU) and results in three different data types: CSPEC, CTIME, and individual counts as time-tagged event data, TTE. A key characteristic of the Fermi GBM instrument, particularly relevant for quantum gravity studies, is its exceptional timing resolution of just two microseconds (Meegan et al., 2009; Thompson & Wilson-Hodge, 2022).

The Fermi Gamma-ray Space Telescope remains, to this day, one of the most powerful and sophisticated instruments for detecting gamma-ray photons from highly energetic phenomena. The exceptionally broad energy coverage, ranging from approximately 8 keV to beyond 300 GeV, and an excellent temporal resolution of both its instruments in microseconds, make Fermi the most advanced tool for studies of high-energy events. It is unambiguous that Fermi provides one of the most suitable options for investigating

potential energy-dependent time delays caused by in-vacuo dispersion. Consequently, the experimental part of this work is dedicated to analyzing Fermi data to identify such quantum gravity-induced time delays.
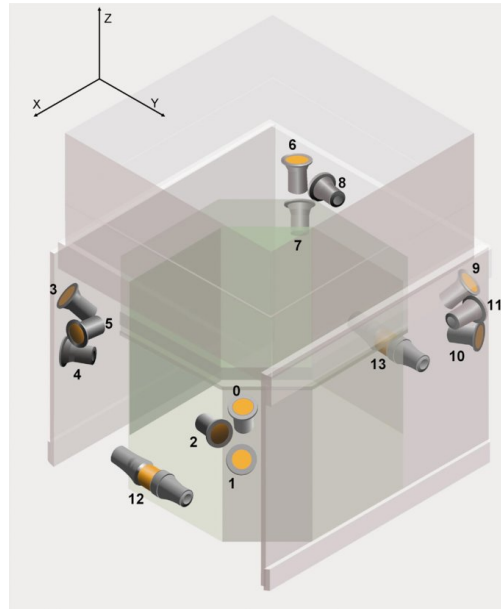
Figure 3.1: The locations and orientations of the GBM detectors on the Fermi spacecraft. The NaI(Tl) detectors, numbered from 0 to 11, are grouped into sets of three at each corner of the spacecraft, while the BGO detectors (12 and 13) are located on opposite sides of the spacecraft. The picture is sourced from the work of Meegan et al. (2009).
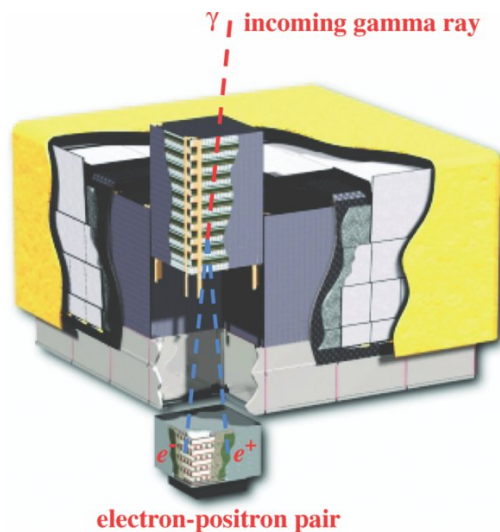
Figure 3.2: Schematic diagram of the Fermi-LAT instrument, located on the top of the spacecraft. The diagram shows a conversion of the incident gamma-ray photon into an electron-positron pair. The scheme is taken from the work of Atwood et al. (2009).

3.1.3 HERMES-TP/SP

High Energy Rapid Modular Ensemble of Satellites Technologic and Scientific Pathfinder (HERMES-TP/SP) serves as a demonstrator to a future ambitious astrophysical mission Gamma-ray Astronomy International Laboratory for Quantum Exploration of Space-Time (GrailQuest), which will launch a large constellation of nanosatellites dedicated to, for the first time, probing the quantum structure of space-time (Burderi et al., 2020).

HERMES consists of six 3U nanosatellites, the first two of which were successfully launched into orbit on March 15, 2025. The mission's main objectives are to investigate the central engine of GRBs, to localize detected high-energy transients applying the triangulation method, and potentially, to search for signatures of a quantum space-time structure (Fiore et al., 2020).

The payload is equipped with a double-detection mechanism. Firstly, the soft X-ray photons are directly detected and absorbed by a solid-state silicon detector, named the silicon drift detector (SDD). The detection of hard X-rays and gamma rays is provided by the already-mentioned scintillation technique. In this case, a novel type of scintillator material not previously used in space applications, the cerium-doped gadolinium aluminum gallium garnet (GAGG:Ce) crystal was selected. A visible light produced by the interaction of high-energy photons with a scintillator crystal is then detected and converted to an electrical signal thanks to the same SDD, operating in this configuration as a photodiode (Evangelista et al., 2020; Fiore et al., 2020; Guzman et al., 2020). A schematic overview of the HERMES detector is presented in figure 3.3.

The HERMES constellation is characterized by its remarkable temporal resolution of less than 250 nanoseconds, and an energy band sensitive to an interval ranging from 5 keV to 500 keV (Evangelista et al., 2020). The HERMES delays software was employed in this thesis as a methodological tool for the search for quantum gravity-induced time delays.
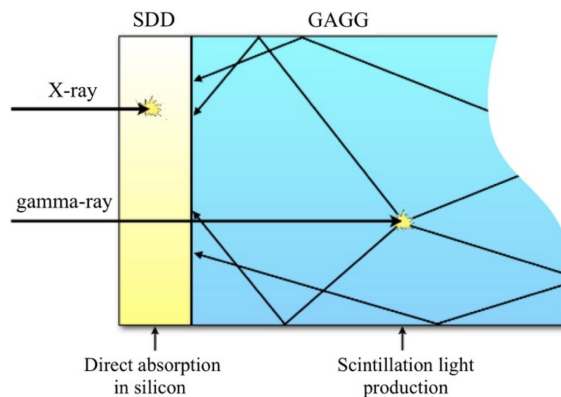

Figure 3.3: A schematic illustration of the HERMES detector. SDD is used to directly detect X-rays from cosmic sources, as well as acting as a photodiode to detect visible light from the GAGG scintillator. The scheme is sourced from the work of Fiore et al. (2020).

3.2 Ground-based telescopes

In contrast to space-based telescopes, which detect the incoming gamma-ray photons directly, ground-based telescopes rely on an indirect detection method, utilizing the Earth's atmosphere as a part of the detection process. In general, we can divide the ground-based very high-energy telescopes into two types, according to the medium where the detection is realised – Imaging Atmospheric Cherenkov Telescopes (IACTs) or water Cherenkov telescopes.

The most prominent examples of IACTs include The High Energy Stereoscopic System (H.E.S.S), an array of Cherenkov telescopes located in Namibia, which has been operational since 2003. Due to its location, the array primarily focuses on high-energy emitters in the Milky Way and the Galactic Center region. H.E.S.S consists of four 12-meter reflector telescopes and one 28-meter reflector telescope in the center of the array (Pühlhofer et al., 2023). Another representative example of an atmospheric Cherenkov telescope array is the Very Energetic Radiation Imaging Telescope Array System (VERITAS), which has been operational since February 2005. It consists of four reflector telescopes, each having twelve meters in diameter. The array is located in Arizona, United States (Holder et al., 2006). The Major Atmospheric Gamma Imaging Cherenkov telescope (MAGIC) has been in operation since October 2004 in La Palma, Canary Islands, Spain. Its reflector dish is seventeen meters in diameter and is composed of diamond-milled aluminum mirrors (Bigongiari, 2005; Bigongiari et al., 2004). In 2009, the second MAGIC telescope, identical to the first one, MAGIC-II, became operational, making the two telescopes a stereoscopic system (Tridon et al., 2010). An ambitious future project is the Cherenkov Telescope Array (CTA). The CTA will consist of more than 50 IACTs built in two locations, in La Palma, Spain, and near Paranal, Chile. Compared to current IACTs, CTA is expected to be five to ten times more sensitive across all energies and is expected to outperform Fermi-LAT in short-term sensitivity by several orders of magnitude (Gueta, 2022). The most prominent example of a water Cherenkov telescope utilized in gamma-ray astronomy is the High Altitude Water Cherenkov (HAWC) observatory, located in Mexico. HAWC is composed of an array of 300 water Cherenkov detectors, each equipped with four PMTs (Mostafa & HAWC Collaboration, 2016).

Despite the differences in design and medium where the detection is realised, all ground-based Cherenkov telescopes rely on the same detection principle. Very high-energy gamma-ray photons cannot be detected directly by space-based telescopes, as their energies are sufficient enough to penetrate the detector material without interaction. The high-energy gamma-ray photon enters the Earth's atmosphere and interacts with atmospheric particles, resulting in an extensive air shower composed of secondary particles. These secondary particles, predominantly electrons and positrons, produce additional photons via bremsstrahlung, resulting in the development of a cascade (Matthews, 2005). A crucial part of this process is the emission of Cherenkov radiation, which occurs when charged particles travel faster than the phase velocity of light in the given medium. The first detection of atmospheric Cherenkov light was made in 1953, in the work of Galbraith & Jelley (1953). The short flashes of Cherenkov light, lasting a few nanoseconds, are then collected by mirrors of the IACTs, or detected directly in water tanks in the case of water Cherenkov telescopes. Photons are detected by PMTs and converted into an electrical

signal, which is then further processed and analyzed to reconstruct the properties of the incident gamma-ray photon (Holder et al., 2006).

The main advantage of using ground-based Cherenkov telescopes for searching for quantum gravity features is the exceptionally high-energy detection capability, ranging for every of the aforementioned telescope arrays from several tens of GeV to several tens or even hundreds of TeV (Terzić et al., 2021). However, one also needs to take into account the indirect nature of the detection technique, affecting the accuracy of the arrival time reconstruction of the incoming gamma-ray photons, or a nontrivial complex discrimination between gamma-ray events and extensive air showers induced by cosmic-ray hadrons. Moreover, unlike space-based telescopes or water Cherenkov telescopes, IACTs are also highly dependent on favorable weather and atmospheric conditions. Observations are usually limited during conditions such as rain, snow, high humidity, strong moonlight, or cloud coverage. A more detailed discussion of probing quantum gravity effects using IACTs can be found in the work of Terzić et al. (2021).

Methodology

Delays software, developed by the Italian HERMES science team to estimate delays in astrophysical data, is the analytical tool employed in this thesis. The author's co-authored publication focused on the detailed description of the delays software has been recently submitted and accepted by the *Astronomy & Astrophysics* journal. Following its publication, the complete Python package will be made publicly available via the GitHub platform.

In the following section, we will summarize the key methods implemented in the HERMES delays software.

4.1 Delays software

The HERMES delays software was created in response to the increasing demand for delay estimation in astrophysical data, with a primary focus on GRB observations. Delays analyzed by the software may be categorized into two types: temporal delays and energy-dependent delays. The estimation of the temporal delays is crucial for finding the position of the transient event in the sky via the triangulation method. The exact localisation of high-energy events in the sky using the triangulation technique is the main focus of the HERMES-TP/SP mission, which was launched in March 2025 (Sanna et al., 2020).

Energy-dependent delays, on the other hand, are delays that can be found in the light curves of different energy bands of the detector. This delay estimation may be useful for investigating the emission mechanism of GRBs (Tsvetkova et al., 2017; Giuliani et al., 2008), probing the AGN geometry and the size of the accretion disk (Zaječek et al., 2020), or searching for a possible quantum gravity-induced in-vacuo dispersion effect.

This delays software is based on cross-correlation function techniques. However, a critical preliminary step before applying these methods is the continuous construction of the light curve from the observed data.

4.1.1 Light curve building

Gamma-ray detectors do not measure the intensity of the signal directly. Instead, they are counting individual photon events. In other words, the detector measures the time when the photon was detected, and its energy. The output after the detection of a transient event, like a GRB, is the time of arrival (ToA) list of photons. However, the use of the term photon is rather a simplification, because one can not say with absolute precision if the detector measured one photon of a certain energy or two photons simultaneously, both with part of that energy. From now on, we will replace the word photon with the word count, referring

to an event that interacted and was counted by the detector.

In this software, we employ a continuous representation of the light curve to estimate delays using the cross-correlation function (discussed more in the following subsection). While traditional light curves, such as the one shown in figure 2.3, are typically displayed as discrete, histogram-like plots representing the number of counts detected in fixed time bins (e.g., one-second bins for GRBAlpha), we opt for a continuous approach for smoother estimation of time delays.

To generate a continuous light curve with a statistically uniform representation, the software first derives each rate point r_i of the light curve by fixing the number of counts N. The following relation can be established for each rate point:

$$r_i = \frac{N}{\Delta t_i}, \tag{4.12}$$

where Δt_i is the time interval within which N counts are detected. It is evident that to maintain the fixed number of counts for each rate point of the light curve, the temporal bin size must be, on the contrary, variable. In other, more simplified words, during the detection of a transient event, the detector must wait varying amounts of time to collect an exact number of counts for each bin. Each obtained rate point is then plotted, and a continuous light curve is finally achieved by linearly connecting all the rate points $r_i(t_i)$.

It is important to emphasize that increasing the number of counts results in a decrease in the temporal resolution of the light curve, and vice versa. The situation is well demonstrated on the GRB 240825A example shown in figure 4.1, where we initially considered $N = 1000$ for light curve building, and then we reduced N to 100. This leads to an important consideration, whether it is better to keep N as small as possible, in order to take advantage of the detector's temporal resolution, or to keep N higher to improve the rate accuracy and to reduce the variability due to Poissonian fluctuations. Therefore, one of our key tasks will be to find a balanced compromise between the two aforementioned outcomes. However, achieving this balance will be particularly difficult at very high energies, where the number of detected counts significantly decreases.

4.1.2   Modified double pool method

The modified double pool (MDP) method is a robust method that allows obtaining the time delay between light curves of two different energy ranges with significantly short computation time. Before describing the process of delay estimation, defining the cross-correlation function is needed.

Cross-correlation function

The cross-correlation function is widely used in signal processing to find a resemblance between two signals. In astrophysics, the cross-correlation may be used to investigate the relation between galaxies and predicted gravitational-wave background (Cañas-Herrera et al., 2020), to study a relation between soft and hard light curves of X-ray sources (Ding et al., 2016), or for measuring line formation in the photosphere of the sun (Faurobert et al., 2012).
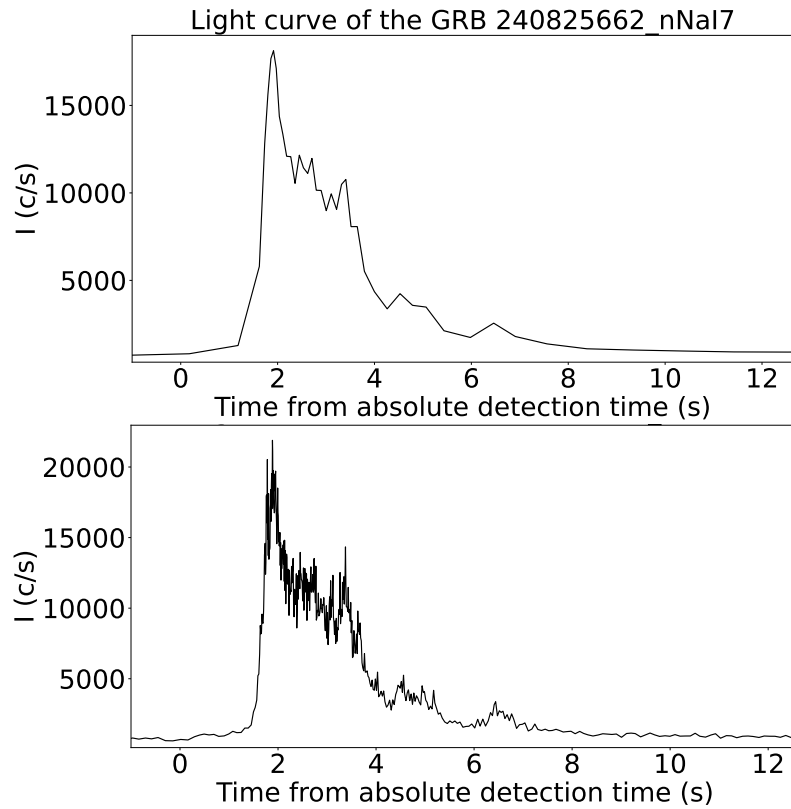
Figure 4.1: The comparison of GRB 240825A light curves for fixed number of counts $N = 1000$ (top) and $N = 100$ (bottom). A noticeable decline in temporal resolution is present when the accuracy of the rate measurement is increased. Fermi-GBM energy channel 7 data were used for the plot, in the energy range 10–100 keV.

After the derivation of two continuous light curves – functions $f_1(t)$ and $f_2(t)$, assuming the first one is measured by a high-energy detector A, and the second one by a low-energy detector B, the unnormalized cross-correlation is defined as:

$$\text{CCF}_{1,2}(\tau) = \int_{-\infty}^{\infty} f_1(t) f_2(t+\tau)\, d\tau, \tag{4.13}$$

where the expected time delay τ between the two functions is defined as the argument at which the cross-correlation function reaches its maximum (MIT, 2008). In our case, the limits of the integral are constrained by the duration of a GRB. A simple example demonstrating the application of the cross-correlation technique on two Gaussian functions, shifted by a specific value, can be found in figure 4.2.

One may already question the applicability of the cross-correlation method on real GRB data, where the association between diverse structures in light curves is less evident, potentially resulting in multiple peaks in the obtained cross-correlation. For this reason, the software allows to fit the most probable maximum of a cross-correlation with the Gaussian profile. The fitted mean of the Gaussian consequently represents the best estimate of the delay. However, the user of the software needs to carefully decide which of the cross-correlation peaks represents the true maximum.
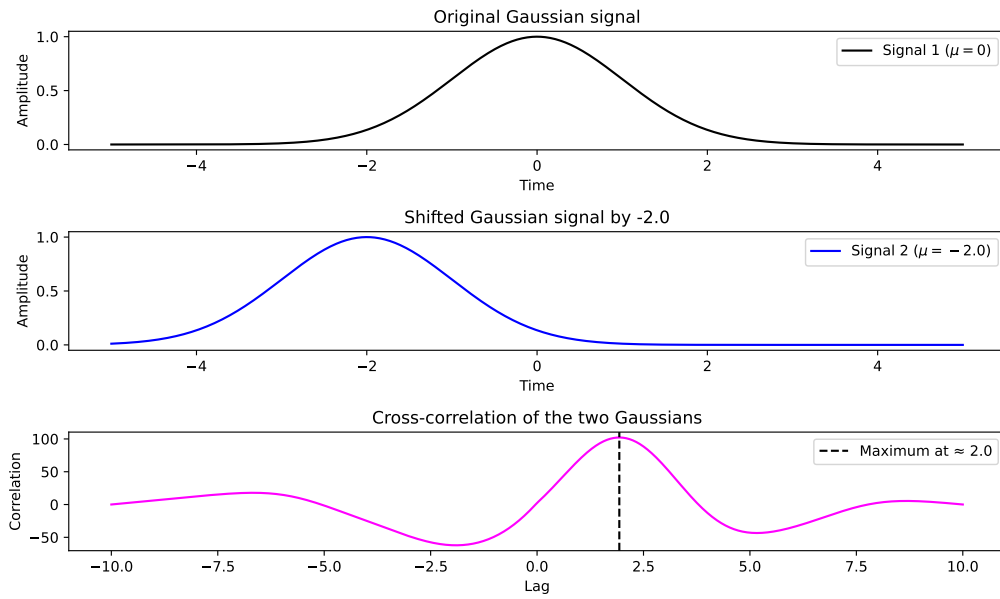
Figure 4.2: A simple example of an application of the cross-correlation function of two identical Gaussian profiles, shifted by a value of 2. The maximum of the resulting cross-correlation represents the shift required to align one function with the other.

The first step of the modified double pool method is the splitting of the ToAs list of the detector into two independent halves. This splitting is done with the help of a random distribution RND(0,1), which generates random numbers between 0 and 1. Each ToA point is associated with one of the two sub-lists, depending on the outcome of the distribution. If a generated random number is smaller than 0.5, the value from the initial ToAs list goes to the first ToAs sub-list. Analogically, if the random number is bigger than 0.5, the ToA value goes to the second sub-list. Due to this random splitting procedure, we obtain two datasets with half the size of the initial dataset. In other words, this splitting in two halves corresponds to a situation where we would have two detectors at the same spatial position, detecting the same GRB event, but each with half of the effective area of the original detector. Since the division has a random nature, it is possible to repeat the splitting procedure as many times as we wish, to obtain a pool of sub-ToAs lists. Each result will always have a different division of ToA values. From each sub-ToAs list, we are capable of deriving a light curve, as described in section 4.1.1. If we would try to cross-correlate the two light curves from the same detector, the maximum would fluctuate around the (expected) zero value, with the fluctuations having a pure statistical origin.

Let's now consider a second detector, measuring the same GRB event, but in a higher/lower energy band. The ToA's list of the second detector undergoes the same procedure as the first one. Subsequently, we possess, for instance, hundreds of light curves for both of the detectors, and we are able to cross-correlate each one with another. The situation is for better comprehensibility illustrated in figure 4.3. The outcome of all the cross-correlations will not be just one, but hundreds of delays estimated. The result of the analysis is therefore a histogram of all calculated delays, centered around the true value of the delay. Consequently, the modified double pool method represents a very robust technique for delay estimation, taking into account statistical fluctuations.
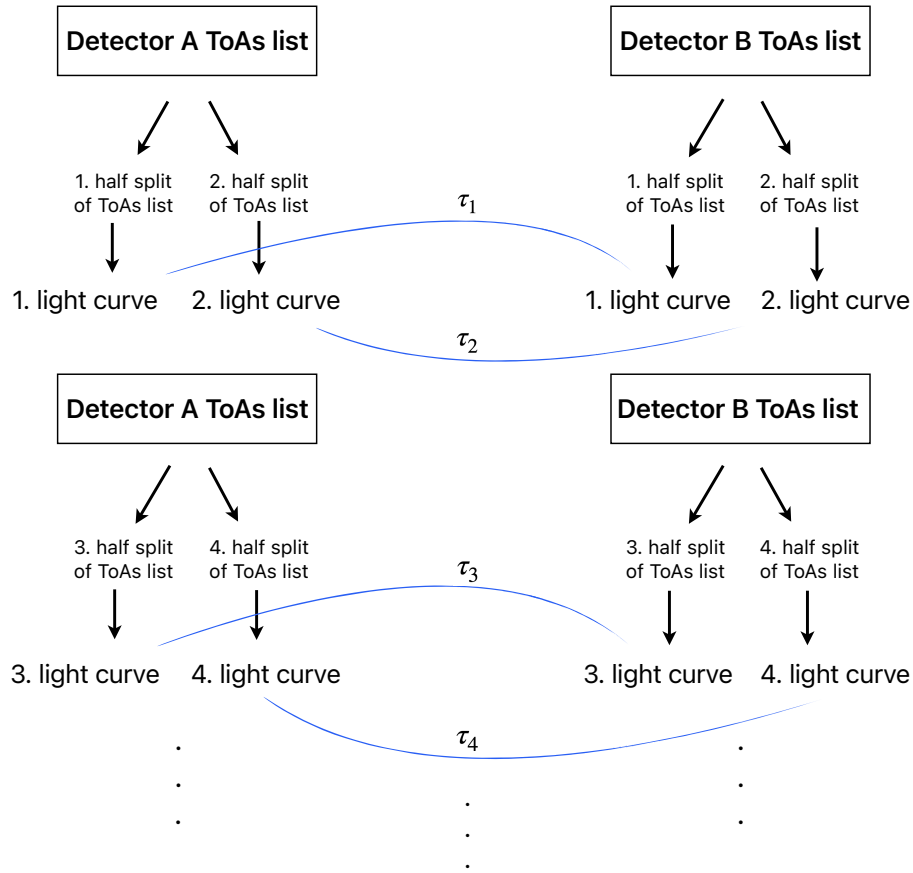
Figure 4.3: Scheme of the modified double pool method splitting procedure. Thanks to a random splitting, we obtain a pool of light curves for each detector A and detector B. The result of the splitting and cross-correlating is a histogram of delays centered around the most probable value.

4.2 Energy range width

In our case, the software is utilized to search for quantum gravity features. Because the in-vacuo dispersion effect is expected to be minuscule, in orders of milliseconds for the MeV range of energies, we need to adopt a very conservative way of how to select the detected energies. The suggestion is as follows – since we will estimate the delay between the arrival of high-energy photons and low-energy photons, the gap between them needs to be big enough, taking into account the operating GRB space detectors, at least by the 10^3 order of energy.

However, another problem appears when dealing with experimental data. We cannot simply choose one exact energy we want to work with for both low-energy and high-energy detectors, because we are not going to gather enough data. In this case, we are obliged to work with energy ranges. At the same time, the chosen energy range should be narrow enough for the time delay within this energy range to be negligible. Subsequently, the

relation for an energy range width will have the following form:

$$v = \frac{E_{\text{max}} - E_{\text{min}}}{E_{\text{mean}}},$$ (4.14)

where E_{min} is the lowest energy of the chosen energy interval, E_{max} is the highest energy and E_{mean} is the mean value of the energy interval. Theoretically, the value of the v parameter should be, at maximum, 0.1, to assume the negligibility of time delays within the chosen energy interval. However, the choice of the v parameter will be highly dependent on the number of counts present in the selected energy range.

Data analysis process

Taking into account the available gamma-ray space telescopes and their parameters, the Fermi Gamma-ray Space Telescope emerges as the most prominent choice for selecting data suitable for quantum gravity studies. We decided to consider Fermi-GBM (only NaI(Tl) detectors) as our low-energy detector, whereas Fermi-LLE and Fermi-LAT are utilized as our high-energy detectors.

5.1 Data retrieval

The first step in obtaining the required dataset was to identify all GRBs with known redshift detected by the Fermi space telescope during its operational period. Since Fermi was launched on June 11, 2008, (Thompson & Wilson-Hodge, 2022), we collected data spanning from that date up to the present. Unfortunately, since there is no catalog listing all detected Fermi GRBs with measured distance, we needed to collect them manually, with the help of NASA's General Coordinates Network (GCN), where science teams report detections of astrophysical transients observed by various telescopes. By reviewing hundreds of GCN pages and checking redshift estimations in scientific literature, we collected in total of 60 GRBs. The complete dataset, including each GRB's trigger time, coordinates, and redshift, is provided in Appendix A.

The next step involved downloading the relevant data files (.fit and .fits) from the three Fermi detectors. These files were obtained from the official NASA Fermi Gamma-ray Space Telescope page. For GBM data, we conducted searches by the GRB identifier (bn name) and then from 12 channels selected the TTE data channel in which the GRB peak was most prominent. In the case of the LLE detector, the search was also performed using the bn GRB name, but in this case, there was no need to choose between multiple channels. Unfortunately, available data for the LLE detector only covered the period from August 25, 2008, to June 27, 2022, which prevented us from accessing observations from the last two years, 2022 to 2024.

Retrieval of LAT data was carried out using a different approach. We employed the known GRB coordinates (as reported in GCN circulars), along with defined observation dates and a search radius. We set observation dates to always start 5 minutes before the GRB trigger time, and end 5 minutes after the trigger time, all in the MET (Mission Elapsed Time) time system. The search radius was always set to 60 degrees. In the case of GRB coordinates, we used the LAT-determined positions by default. However, in cases where LAT coordinates were not available (because the LAT detector did not trigger on the burst), we took the coordinates provided by GBM instead.

5.1.1 Dataset reduction

It is important to emphasize that not every GRB was detected by all three detectors. Most of the time, only two of the three detectors triggered on the burst, with GBM triggering most of the time, as it is covering the lowest energies. This is not, in principle, a problem, as we only need two detectors for comparison. However, in the GRB 181201A and GRB 210822A cases only one, LAT detector triggered on the burst, excluding these two GRBs from the analysis. A similar problem came with the following GRBs: GRB 090102, GRB 091024, GRB 091127, GRB 100728A, GRB 100728B, GRB 110213A, GRB 120729A, and GRB 151027A, where only the GBM detector was triggered and provided data, which hindered our ability to conduct analysis on these events.

Another problem appeared in the case of GRB 130925A, GRB 190829A, and GRB 201216C. For these events, the GBM detector triggered on the bursts, but unfortunately, even though LAT detected them, the flux at higher energies was not strong enough to reach the trigger threshold. In Appendix A, these cases are marked in the Fermi-LAT column as "no (upper limit)". After the visualisation of raw data in a counts map with the astronomical imaging and data visualization application, DS9, we decided not to include these GRBs in the analysis. An example of a count map for GRB 130925A is presented in figure 5.1, where detected counts are mostly background, without a significant increase of flux in a circular shape presenting a transient event.
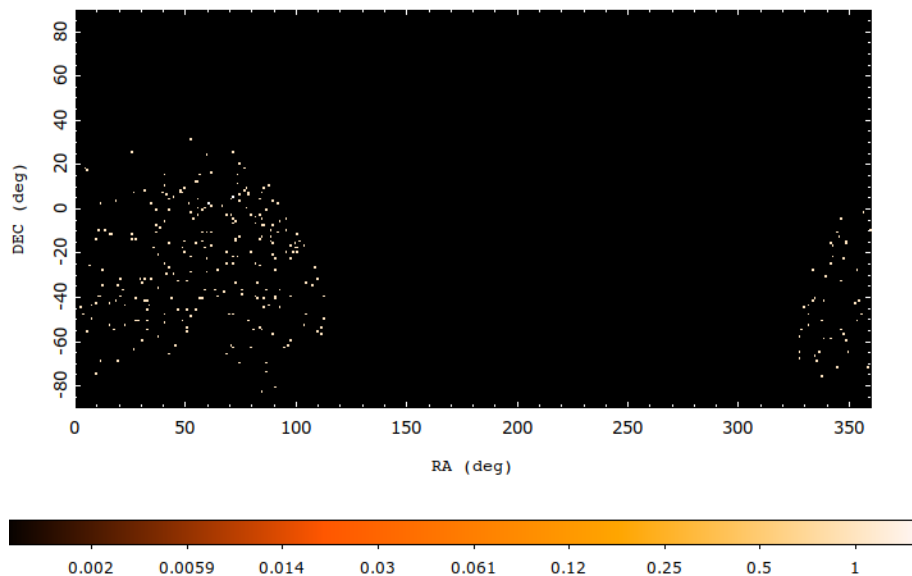
Figure 5.1: GRB 130925A raw counts map, as seen by the Fermi-LAT detector, visualised using the DS9 visualisation tool. The data with its dominating uniform distribution of background noise completely obscures the presence of counts originating from the burst. Since the light curve reconstruction is very uncertain due to very limited data available, we decided not to consider the LAT upper limit GRBs, GRB 130925A, GRB 190829A, and GRB 201216C.

A particularly unusual case was encountered with GRB 120711A. After inserting the GRB parameters from the Fermi GCN circular into the Fermi-LAT data retrieval page, downloading the selected files, and visualizing the data in DS9, we discovered that almost no data were available for this event. The situation is illustrated in figure 5.2. Unfortunately, since Fermi-LLE also did not detect the event, GRB 120711A was excluded from the analysis.
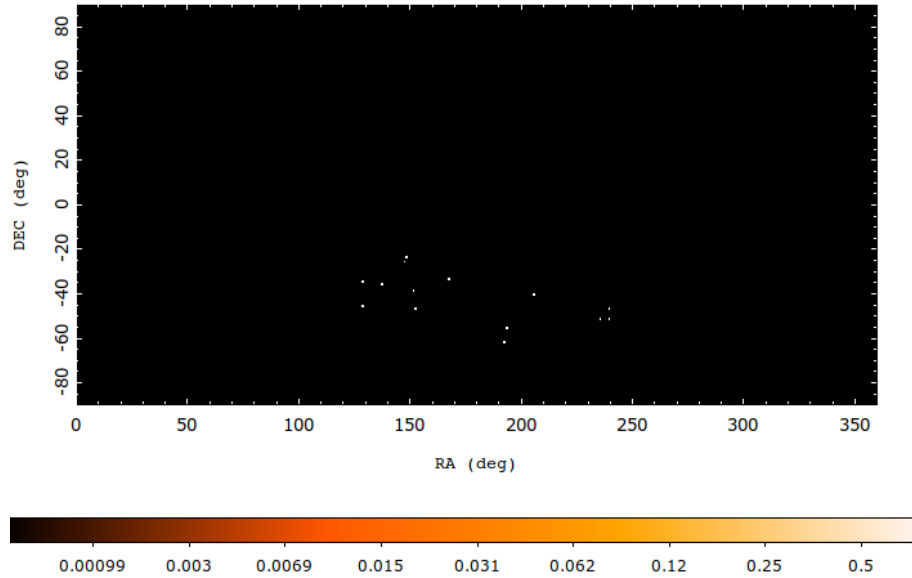

Figure 5.2: A visualised GRB 120711A event detected by Fermi-LAT detector. Even though the GCN circulars number 13452 (Kocevski et al., 2012) and 13444 (Tam et al., 2012) report the detection of a bright burst, the number of detected counts is too low to construct a light curve with sufficient resolution. Therefore, the GRB 120711A is also not considered for the analysis, since there is also no Fermi-LLE data for this burst.

We may now see that even though we initially compiled a dataset consisting of 60 GRBs, the number of GRBs decreased significantly after the implementation of the aforementioned conditions. In total, 14 GRBs were labeled as unusable, resulting in a final sample of 46 GRBs ready to be analyzed. Since figures 5.1 and 5.2 show situations for insufficient GRBs for the analysis, it is useful to also present representative examples of GRB data visualisation. Among others, GRB 131108A fulfills the criteria. Raw data visualisations of GRB 131108A from both Fermi-LAT and Fermi-LLE detectors are shown in figure 5.3. It is important to note that all count maps in this subsection are displayed on a logarithmic scale.

5.2   Data analysis

After the careful selection of suitable GRBs for analysis, we can now proceed with the analysis of the data and estimation of time delays. The methodology employed for the analysis was described in detail in the previous chapter.
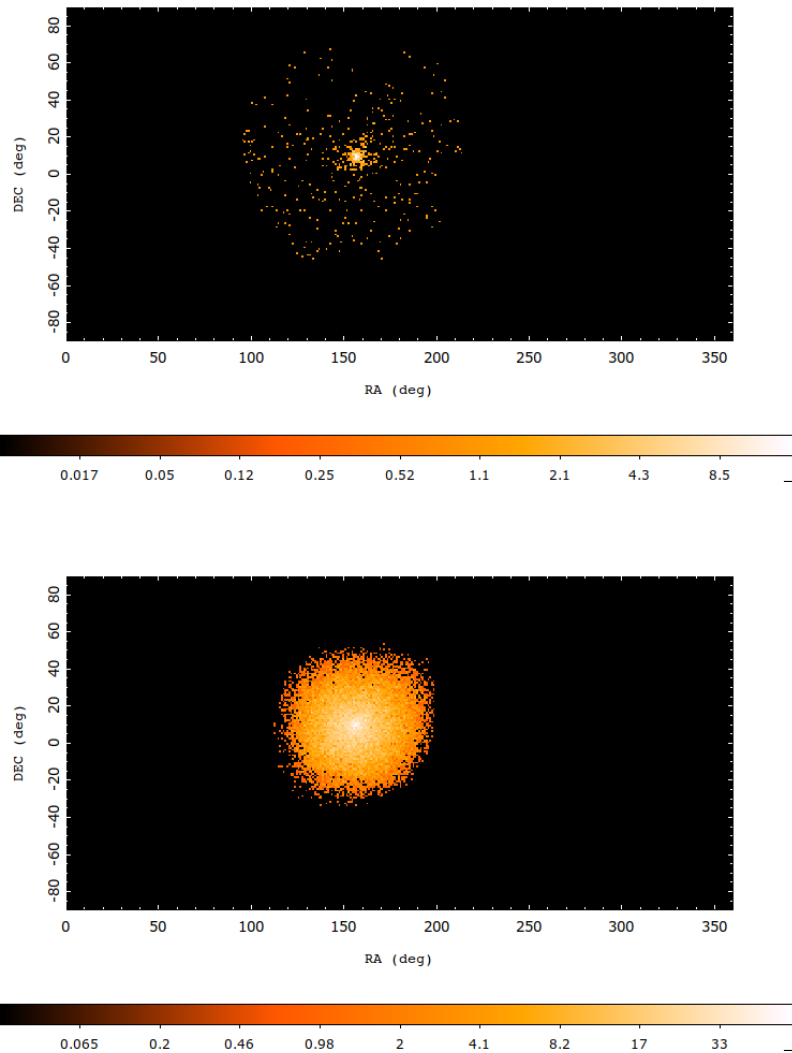
Figure 5.3: The raw count maps of GRB 131108A as observed by the Fermi-LAT detector (top) and Fermi-LLE detector (bottom). Unlike other visualised GRB examples, in this case, a circular increase in counts around the GRB position center is clearly visible, confirming the detection of the GRB event.

5.2.1   Energy range selection and additional data reduction

The first step of the analysis involves selecting appropriate energy ranges for all GRBs and all three detectors, with a sufficient number of counts for light curve construction. Simultaneously, the selected energy intervals must be narrow enough to ensure negligible delays within the band, as described in section 4.2.

Since Fermi-GBM detects the lowest energies, the quantum gravity-induced time delays are expected to be orders of magnitude smaller than the delays we aim to investigate in the MeV range, and therefore, we may choose a slightly wider energy range. Taking into account the instrument's energy coverage and a sufficient number of counts in the energy

interval, we decided to always adopt a 10–100 keV energy range for the GBM detector. The optimal energy bands for the LLE and LAT detectors were found automatically by the software. The software worked in the following way – we inserted the desired energy range width ν, the software made a table of sliced energy bands from the data, together with the number of counts within the energy band. Subsequently, we chose the 3-5 most optimal energy bands with the highest number of counts, and we did this for every GRB.

As we may expect, not every GRB possessed enough counts in the energy bands, especially in LAT data. While with the LLE detector, we were able to choose energy bands with hundreds of counts and reconstruct light curves with sufficient resolution, in the case of the LAT detector we had tens of counts, or in some cases, even smaller. In this situation, it was impossible to conduct an adequate analysis, and therefore, we faced a dilemma. The only way to collect more counts in the bands would be to radically increase the ν parameter to 0.7, or even 1, but this option did not correspond with our requirement of narrow energy bands to ensure the negligibility of delays. Consequently, we were forced to exclude several more LAT GRBs from the analysis.

GRB name	LAT energy ranges [MeV]	ν_{LAT}
GRB 080916C	50.4–64.8, 107.1–137.7, 292.7–376.3	0.25
GRB 081024B	–	–
GRB 090323	–	–
GRB 090328	–	–
GRB 090510	52.6–67.6, 86.9–111.8, 237.5–305.4	0.25
GRB 090902B	72.4–93.0, 119.6–153.8, 254.2–326.8	0.25
GRB 090926	39.9–51.3, 84.8–109.0, 180.2–231.7	0.25
GRB 100724B	–	–
GRB 110721A	–	–
GRB 110731A	–	–
GRB 130427A	–	–
GRB 130518A	–	–
GRB 131108A	49.8–64.1, 105.9–136.2, 136.2–175.1	0.25
GRB 131231A	–	–
GRB 140206B	–	–
GRB 140619B	–	–
GRB 141028A	–	–
GRB 150403A	–	–
GRB 160509A	38.6–49.6, 63.8–82.0, 82.0–105.5	0.25
GRB 170214A	49.9–64.1, 106.0–136.3, 175.2–225.3	0.25
GRB 170405A	–	–
GRB 180720B	–	–
GRB 240825A	40.0–51.4, 51.4–66.1, 85.0–109.2, 140.4–180.6	0.25

Table 5.1: A final table with all the GRBs and their chosen LAT energy bands, used in the analysis. For several GRBs, we would need to have a ν parameter close to 1 to possess enough counts in the energy bands. Therefore, these GRBs were excluded, as marked in the table with a dash (–).

GRB name	LLE energy ranges [MeV]	ν_{LLE}
GRB 080916C	15.2–19.5, 25.1–32.3, 41.5–53.4	0.25
GRB 081024B	15.2–19.5, 25.1–32.3, 19.5–25.1	0.25
GRB 090323	10.5–13.5, 13.5–17.4, 17.4–22.3	0.25
GRB 090328	10.4–12.7, 15.5–19.0, 23.2–28.3	0.20
GRB 090510	8.2–10.1, 12.3–15.1, 27.5–33.6, 61.3–74.9	0.20
GRB 090902B	9.8–12.0, 14.6–17.9, 21.8–26.7, 32.6–39.9, 59.6–72.8	0.20
GRB 090926	13.8–16.8, 20.5–25.1, 30.7–37.5, 45.8–56.0, 68.5–83.7	0.20
GRB 100724B	8.3–10.2, 12.4–15.2, 18.6–22.7, 33.9–41.4	0.20
GRB 110721A	7.2–8.8, 10.8–13.2, 16.1–19.7, 19.7–24.1	0.20
GRB 110731A	7.2–9.2, 11.8–15.2, 19.5–25.1, 41.5–53.4	0.25
GRB 130427A	6.0–6.6, 8.9–9.9, 14.7–16.3, 24.3–26.8, 36.2–40.0	0.10
GRB 130518A	8.6–11.6, 11.6–15.7, 15.7–21.2	0.30
GRB 131108A	7.1–8.7, 8.7–10.6, 10.6–12.9, 12.9–15.8, 19.3–23.6, 23.6–28.8	0.20
GRB 131231A	6.0–7.7, 9.9–12.7, 16.3–21.0	0.25
GRB 140206B	5.9–7.3, 8.9–10.8, 13.2–16.2, 24.2–29.5	0.20
GRB 140619B	7.2–9.2, 11.8–15.2, 25.1–32.3	0.25
GRB 141028A	5.7–6.9, 8.5–10.4, 15.5–18.9, 28.3–34.5	0.20
GRB 150403A	8.1–10.0, 12.2–14.9, 40.6–49.6	0.20
GRB 160509A	11.2–13.7, 16.7–20.5, 25.0–30.6, 37.3–45.6, 55.8–68.2	0.20
GRB 170214A	11.2–13.7, 16.7–20.5, 25.0–30.6, 37.3–45.6	0.20
GRB 170405A	15.2–19.5, 25.1–32.2, 41.5–53.3	0.25
GRB 180720B	11.2–13.7, 16.7–20.5, 25.0–30.6, 37.4–45.7	0.20
GRB 240825A	not detected by LLE	–

Table 5.2: A final table with all the GRBs and their chosen LLE energy bands, used in the analysis. Although we expected to work with $\nu = 0.1$, in reality, we managed to apply 0.1 and have enough counts to construct a light curve only in one case, GRB 130427A. In all other cases, we were obliged to increase the ν parameter, typically to 0.2 and 0.25. For one event, GRB 130518A, we applied $\nu = 0.3$.

Our final sample of GRBs, together with their chosen energy bands, is presented in tables 5.1 and 5.2. Therefore, the final number of analyzed GRBs was reduced by 50%, to 23 GRBs.

5.2.2 Cross-correlation and fitting procedure

After a successful estimation of all energy bands, the next step was to construct light curves for both the low-energy detector (GBM) and high-energy detector (LLE or LAT), for every GRB. As described in section 4.1.1, we needed to specify the number of counts N we aim for every light curve. Usually, for GBM light curves, N varied in the order of hundreds, while for high-energy detectors, N varied in the order of single counts, typically 2 to 10 counts, due to already few initial data. An example of a constructed GBM and LAT light curve for GRB 160509A can be found in figure 5.4.
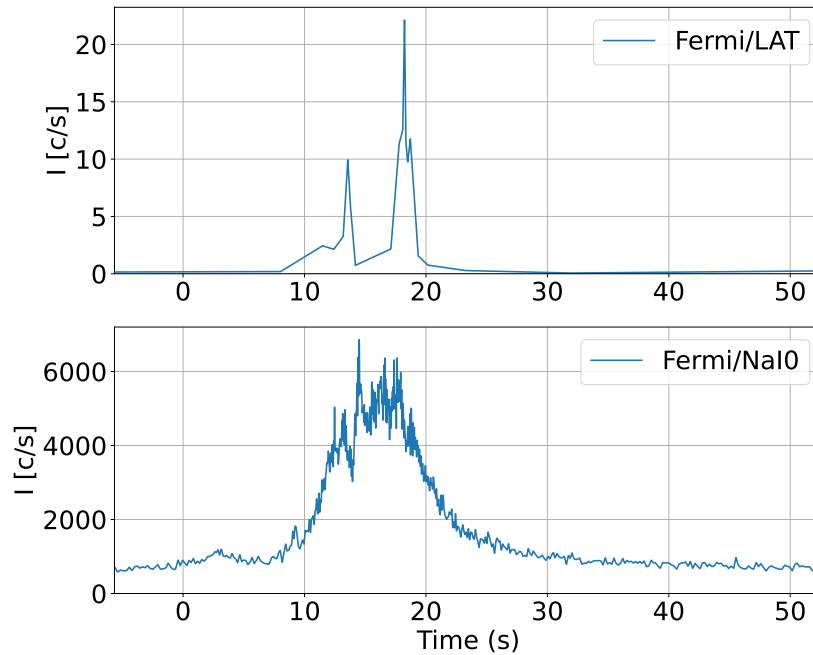
Figure 5.4: LAT ($N = 2$) and GBM/NaI ($N = 150$) light curves for GRB 160509A. Energy ranges selected in this case are 10–100 keV channel 0 for GBM and 38.6–49.6 MeV for LAT.

After a successful estimation of N for both detectors, the software continued with the determination of the delay between the two light curves with the use of a cross-correlation function. The cross-correlation for GRB 160509A is illustrated in figure 5.5. In this case, the maximum is at 0.87 seconds, representing a 0.87 seconds delay between the energy intervals 10–100 keV and 38.6–49.6 MeV.

It is important to emphasize that not every cross-correlation resulted in one clearly visible peak, as seen in figure 5.5. In most cases, the cross-correlation function produced multiple peaks, typically due to complex and diverse light curve morphology. That is why the fitting of the correct peak is indispensable. The Gaussian fitting of the peak is shown in the cross-correlation plot in blue. In the case of figure 5.5, we fitted the only peak present, ending up with a slightly different maximum value. The reason behind this is to remain conservative and consider every fluctuation that might be present near the peak. However, the role of the Gaussian fitting is more clearly demonstrated in the case of GRB 180720A. Here, multiple peaks are visible, each potentially corresponding to a true value of the delay between the two energies. When such a situation occurs, the user's role is to determine which is the most probable peak representing the time delay, by simply looking at the light curves. The most probable peak is then fitted with a Gaussian function. The other function of the Gaussian fitting is to specify the region of the cross-correlation that the software should consider in the next derived light curves. It is necessary to repeat that we only examine and analyze the first light curves from the scheme in figure 4.3. For all subsequent light curves, the code automatically searches for the peak within the area defined by the Gaussian fit.
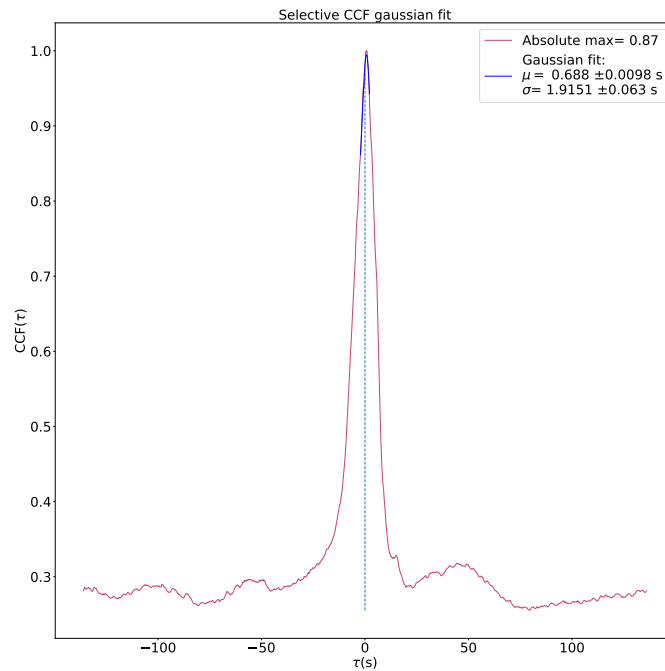
Figure 5.5: Cross-correlation for GRB 160509A LAT (38.6–49.6 MeV) and GBM (10–100 keV). Only one clearly distinguishable maximum can be observed, representing the time delay.
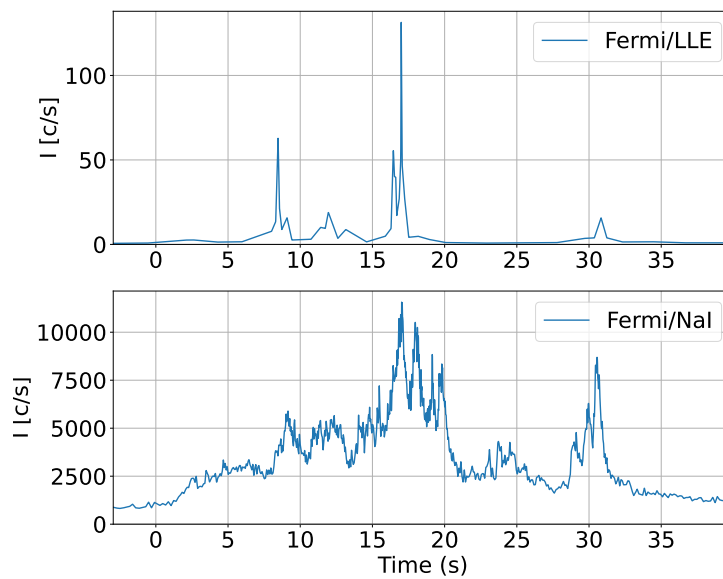

Figure 5.6: LLE ($N = 3$) and GBM/NaI ($N = 200$) light curves for GRB 180720A. Energy ranges selected in this case are 10–100 keV channel 7 for GBM and 25.0–30.6 MeV for LLE.
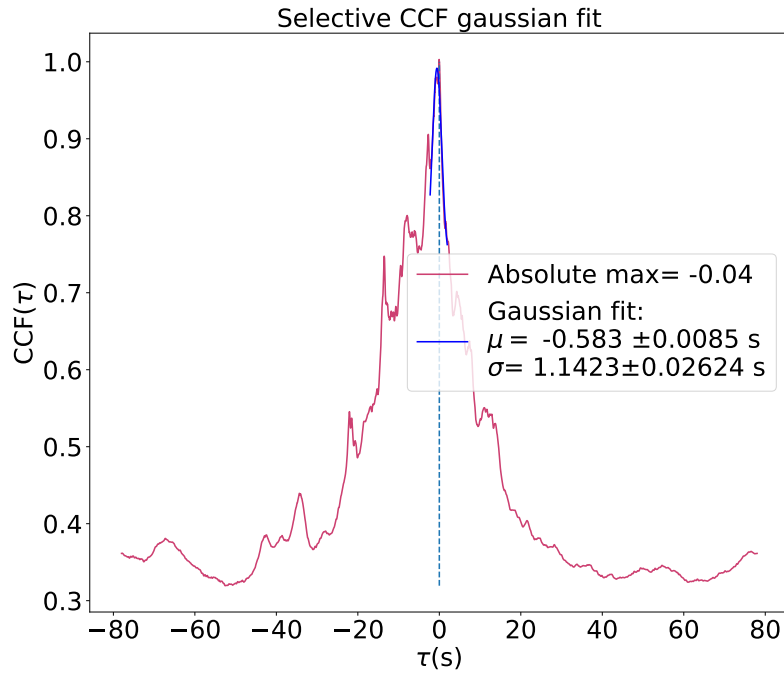
Figure 5.7: Cross-correlation for GRB 180720A LLE (25.0–30.6 MeV) and GBM (10–100 keV). Unlike the GRB 160509A case, in this example, multiple peaks appear in the cross-correlation function. The estimation of the most probable peak corresponding to a specific value of time delay is done with the help of Gaussian fitting. By looking at the GRB 180720A light curves in figure 5.6, one may assume that the most significant peaks of the GRB were detected simultaneously by both detectors. Consequently, the selected peak for Gaussian fitting in the cross-correlation function was the one located around zero.

5.2.3 Repeated random splitting

The analysis outlined in the previous section applies only to the first light curve of the GBM detector and the first light curve of the LAT/LLE detector, as illustrated in the scheme 4.3. In order to obtain a robust estimation of time delays and to minimize the influence of statistical fluctuations, this procedure must be repeated multiple times. Fortunately, the process of splitting the ToAs lists, constructing the light curves, and performing the cross-correlation for all derived light curves is done automatically by the code. The search area for the most probable time delays is defined by our Gaussian fit of the cross-correlation function. In this study, the number of derived light curves was consistently set to 500, corresponding to 250 random splittings of the ToAs lists into two halves, derivations of light curves, and cross-correlation of all the light curves one with another. Consequently, the result of every analysis is a histogram, centered around the true value of the delay. Examples of results for our already mentioned GRBs – GRB 160509A and GRB 180720A – are shown in figures 5.8 and 5.9. Additional examples of cross-correlation functions and their resulting histograms for eight LAT-GBM GRBs and eight LLE-GBM GRBs are provided in Appendix B.
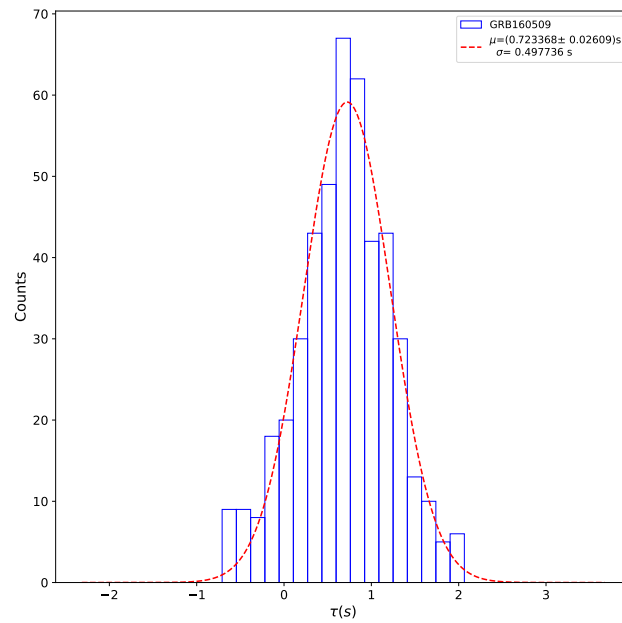
Figure 5.8: Resulting histogram of GRB 160509A LAT (38.6–49.6 MeV) GBM (10–100 keV) analysis. The final estimated time delay is 0.72 ± 0.50 seconds.
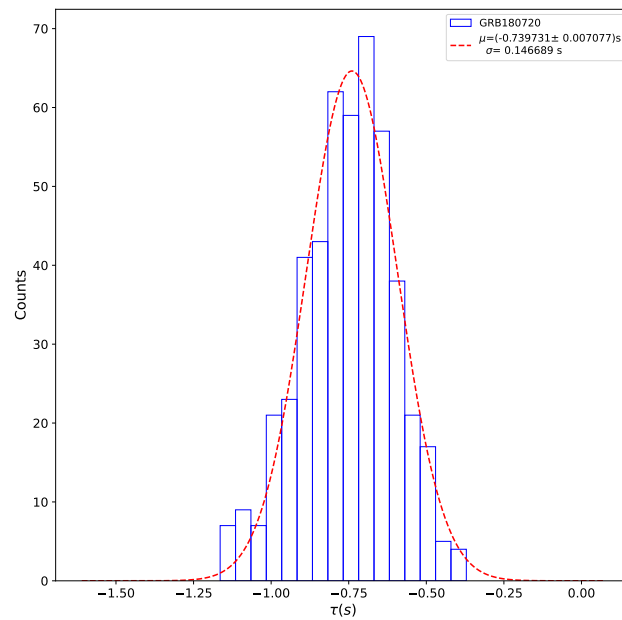

Figure 5.9: Resulting histogram of GRB 180720A LLE (25.0–30.6 MeV) GBM (10–100 keV) analysis. The final estimated time delay is -0.74 ± 0.15 seconds.

5.2.4 Selected GRBs

After a detailed analysis of each GRB and its respective energy bands, as presented in tables 5.1 and 5.2, we now investigate how the observed delay changes with increasing energy. Given that the quantum structure of space-time is expected to be unveiled and manifest at sufficiently high energies, approaching the Planck scale, we expect a more dominant delay at higher energy bands. Consequently, an increasing trend in the delay plotted as a function of energy is theoretically expected.

However, despite this assumption, our analysis has revealed various outcomes. The following pages present analyses of six GRBs that demonstrate the observed variations in delay behavior. We note that E_{mean} plotted on the x-axis of the resulting plots represents a geometric mean of the minimum and maximum boundaries of a given energy band.

The first case, the GRB 180720A LLE-GBM analysis presented in figure 5.10 demonstrates an increasing trend, however, all three measured delays have negative values. This indicates that photons of higher energies arrived earlier than those in the 10–100 keV energy range detected by the GBM detector. Moreover, the delay approaches zero for higher energies.

Next example, GRB 110731A LLE-GBM in figure 5.11 exhibits a decreasing delay of LLE photons with increasing energy, which aligns with the theoretical trend expected from quantum gravity models, but with a negative value of the parameter η.

The third case, GRB 090510 LLE-GBM (figure 5.12), follows the expected pattern, with increasing values of delay for higher energies. It is important to emphasize that the magnitude of the delay value is essential to examine the quantum gravity-induced delays. We will focus on the comparison with theoretical predictions in the following chapter.

The fourth example, GRB 080916C LAT-GBM analysis in figure 5.13 shows another example of an increasing trend. However, in this instance, the estimation of delay is affected by a larger uncertainty than in the case of GRB 090510. The uncertainty is reflected in the value of the slope of the linear fit and its associated error, with the uncertainty exceeding the value of the slope itself. Consequently, we cannot definitively conclude whether high-energy photons were detected later or earlier than low-energy photons.

GRB 160509A, plotted for both LAT-GBM and LLE-GBM (figure 5.14) again demonstrates this increasing trend. Moreover, delays observed in the LAT-GBM analysis directly align with those from the LLE-GBM analysis, confirming the consistency between the two analyses.

Finally, the GRB 131108A LLE-GBM and LAT-GBM analyses in figure 5.15 both present a case where the measured delays appear randomly distributed, without a clear trend. Furthermore, delays in the LAT energy bands do not follow up with those in the LLE energy bands.

All the demonstrated GRBs and their delay evolution raise important questions regarding the accurate representation of dependencies in the analysis, as well as potential systematic uncertainties arising from detector characteristics, or the correctness of our software. Since plotting the dependence of delays on energy for every value of a redshift (or, in other words, for each GRB separately) yields unsatisfactory results, due to the apparent randomness of the resulting slopes, we adopt an alternative approach to investigate the dependence of delay on energy and redshift. The strategy is outlined in the following subsection.
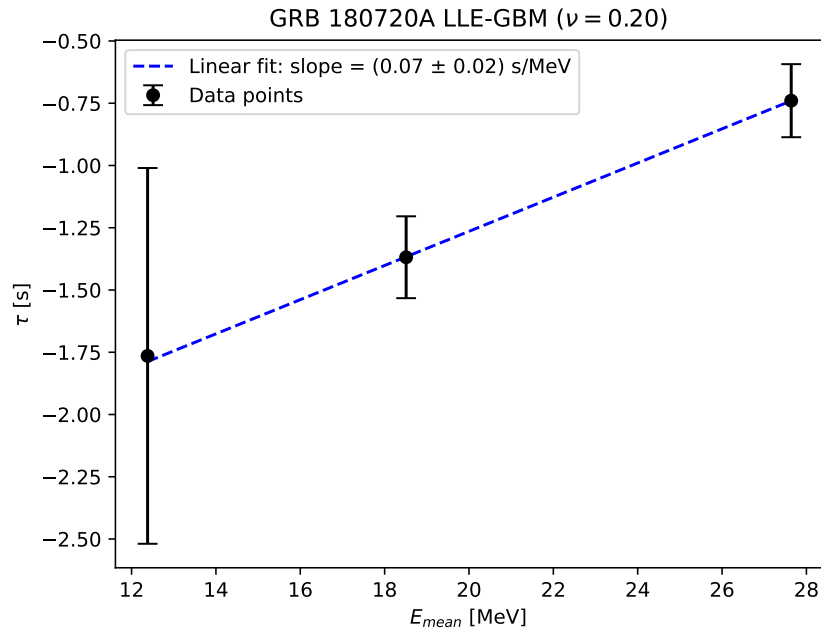
Figure 5.10: Resulting delays from GRB 180720A LLE-GBM analysis plotted as a function of energy. This case illustrates a scenario in which high-energy photons arrive earlier than their low-energy counterparts, with a decline in delay as energy increases.
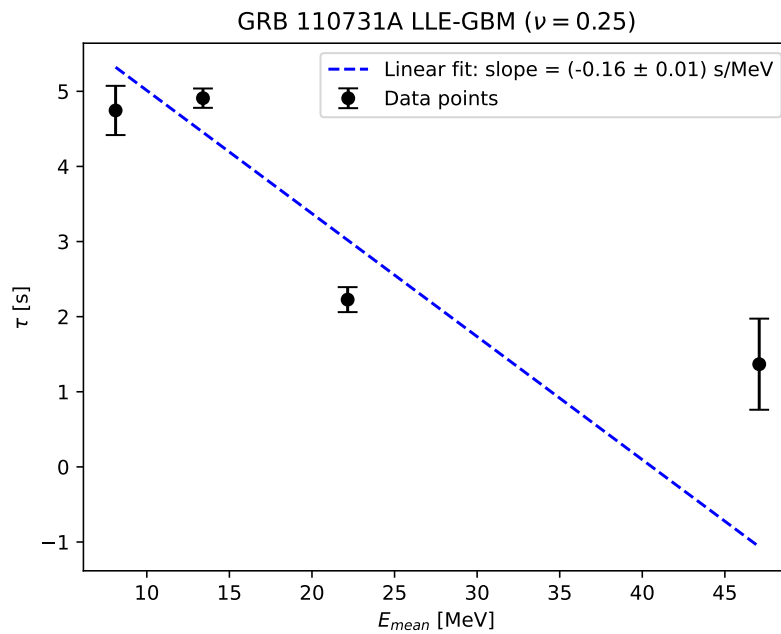
Figure 5.11: Obtained delays from GRB 110731A LLE-GBM analysis plotted as a function of energy illustrate a case in which the delay of high-energy photons diminishes with increasing energy. This behavior differs from the standard predictions of quantum gravity models with positive η, and may instead point to the presence of alternative effects or a scenario with negative η.
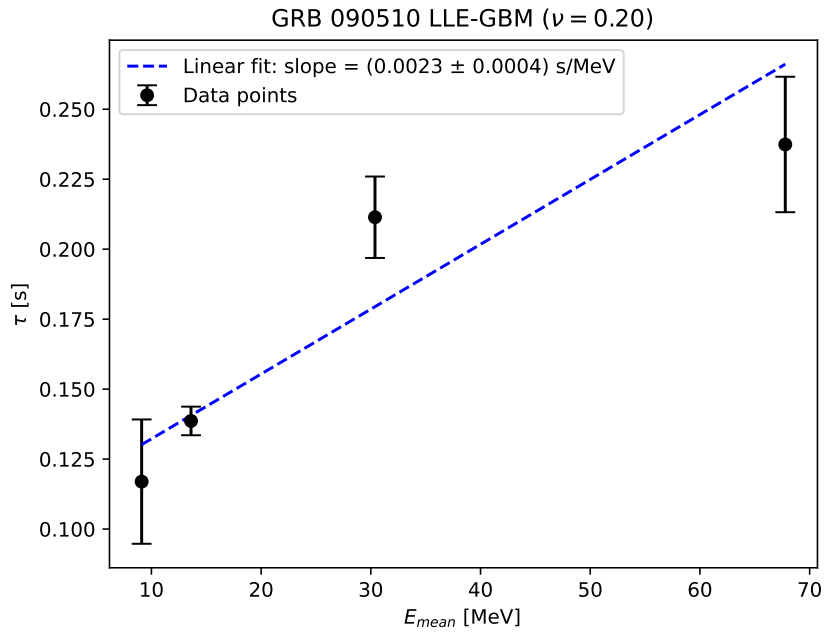
Figure 5.12: Resulting delays from GRB 090510 LLE-GBM analysis plotted as a function of energy, demonstrate a behavior consistent with theoretical expectations – high-energy photons arrive later than their lower-energy counterparts. However, the magnitude of the observed delays exceeds what would be expected from the quantum gravity-induced dispersion effect alone.
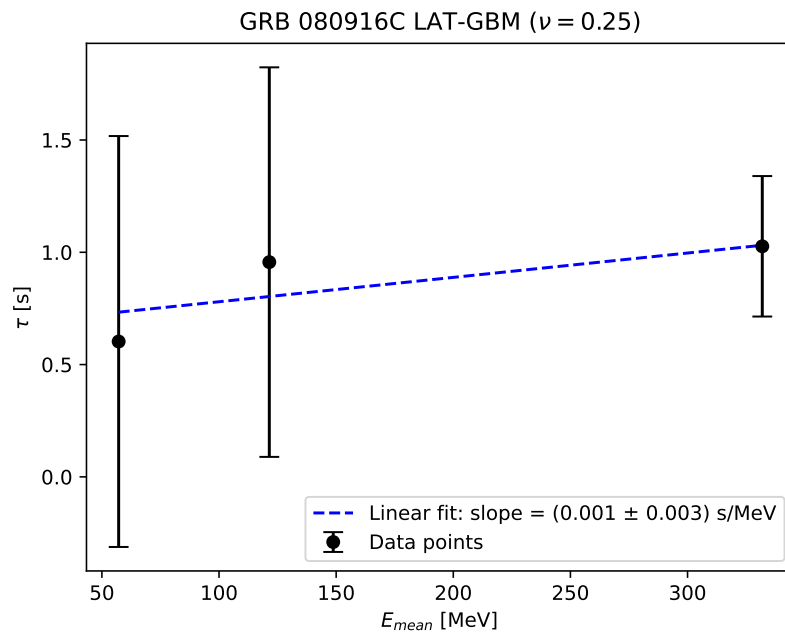
Figure 5.13: Obtained delays from GRB 080916C LAT-GBM analysis plotted as a function of energy. The uncertainty of measured delays dominates in the plot, resulting in an ambiguous value of the slope. In this situation, no clear increasing or decreasing trend can be resolved.
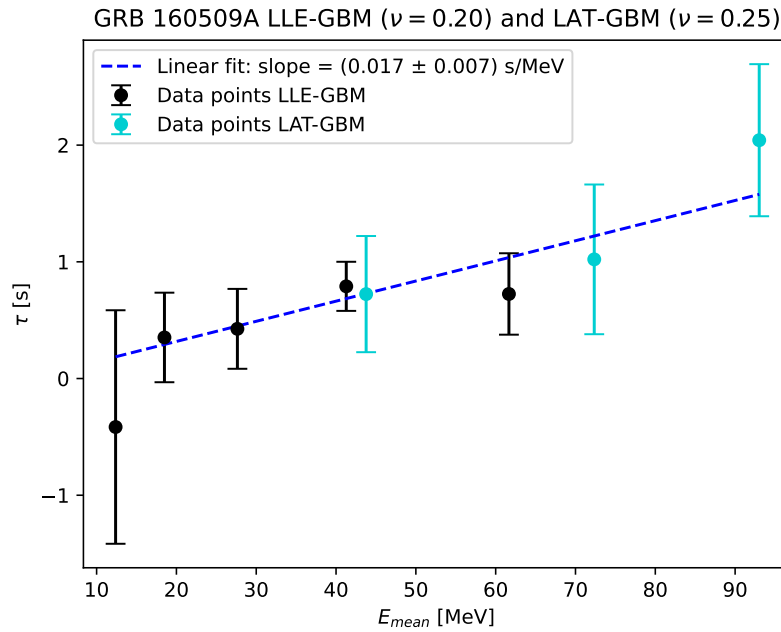
Figure 5.14: Resulting delays from GRB 160509A LLE-GBM and LAT-GBM analysis plotted as a function of energy. In comparison with the GRB 090510 case, this example similarly exhibits more prominent delay values than expected from quantum gravity models. However, delays from LAT-GBM analysis follow smoothly the LLE-GBM delays, validating the consistency of the analysis.
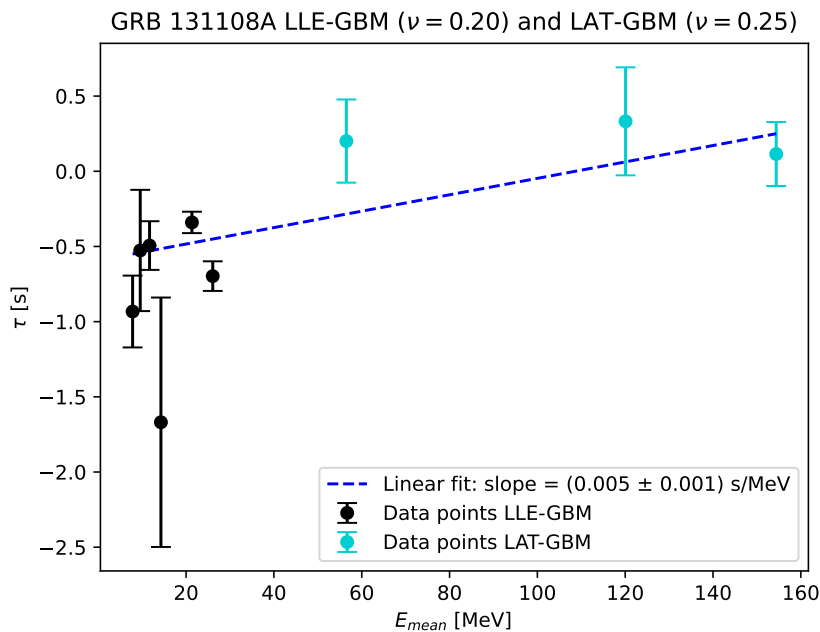
Figure 5.15: Resulting delays from GRB 131108A LLE-GBM and LAT-GBM do not exhibit any clear trend for either instrument. Moreover, the LAT-GBM delays do not align linearly with the LLE-GBM delays, suggesting a possible inconsistency between the datasets.

5.3 Visualisation of time delays

The visualisation of the measured time delays and their comparison with theoretical predictions represents a nontrivial challenge. Since quantum gravity-induced time delays are expected to depend on both photon energy and redshift, it is necessary to adopt a more sophisticated strategy for plotting the delays as a function of these two quantities in order to reveal any potential quantum gravity signature. In this subsection, we adopt an alternative approach – plotting firstly the delays as a function of redshift, and subsequently as a function of energy.

The preliminary step of obtaining the final plot is to apply a cosmological correction. Given that GRBs are at cosmological distances from us, the effects of general relativity cannot be neglected. As a result of cosmological time dilation, all obtained time delays τ must be divided by a cosmological factor in the following way,

$$\tau_{\text{corrected}} = \frac{\tau}{1+z}, \tag{5.15}$$

where z is the redshift of the source. Similarly, the photon energies we detect correspond to the observer's frame, and not the rest frame of the GRB. Consequently, photons that travel cosmological distances have their energies redshifted, and they need to be corrected by multiplying the energies with the cosmological factor:

$$E_{\text{rf}} = E_{\text{obs}}(1+z), \tag{5.16}$$

where E_{rf} is the energy in the GRB rest frame and E_{obs} is the energy measured by a detector.

Following the application of cosmological corrections, the next step involves constructing energy bins. In principle, we take the entire energy range we worked with in our analysis and divide it into discrete intervals, or in other words, energy bins. Each energy bin needs to have a sufficient width to contain a fixed number of measured delays. Therefore, for each of these energy bins, we can plot the corrected delays as a function of redshift. According to theoretical expectations, the delay should exhibit a linear dependence on redshift. Consequently, we perform a linear fit to each of these plots and extract the corresponding slope, which characterizes the significance of the redshift dependence.

As a result, we obtain a set of slope values, one for each energy bin. These slopes possess information about the redshift dependence of delays for various energy scales. The next step is to plot the obtained slope values as a function of energy, where the energy is represented by the geometric mean of the lower and upper bounds of each energy bin. Applying this approach, we reduce the originally complex problem to a two-step approach. We first characterize the delay–redshift dependence within specific energy intervals and then analyze how this dependence evolves across different energy scales. In other words, we recover a representation of the measured delays as a function of both redshift and energy. According to quantum space-time predictions, the dependence should exhibit a linear trend (we adopt the first-order modification of photon propagation through quantum space-time). In the final step, we compare our measured dependence with the theoretical predictions derived from relation 1.10. The full implementation of this methodology, along with a presentation of the resulting plots and comparison with theoretical expectations, is provided in the following chapter.

Results and discussion

6.1 Experimental results

By implementing the method described at the end of the previous chapter, we obtained a total of 29 discrete energy bins. The idea behind selecting the appropriate number of delay points per energy bin is as follows: for the lowest (already cosmologically corrected) energies, ranging from 8 MeV to 20 MeV, the number of measured delays was relatively low. Since at least three data points are needed to determine whether a linear trend is present (rather than simply connecting two points), we selected three delay values in each of the first two energy bins as a minimum requirement. Energies between 20 MeV and 200 MeV yielded the highest number of measured delays. This allowed us to define 21 energy bins within this interval, each containing four estimated delays. The issue of a limited number of measured delays reemerged at higher energies, from 200 MeV to 1775 MeV. For these high-energy regions, it was necessary to widen the bins in order to ensure that each contained at least three delay points. All resulting energy bins, together with the number of included data points, are presented in table 6.3. We note that the highest energy bin needed to span from 700 MeV to up to 1775 MeV to cover the final three measured delays. This choice contradicts our initial assumption of the need for narrow energy bins, however, since the total number of measured delays was lower than initially expected, we aimed to make use of every available experimental delay estimate.

The subsequent step involved plotting and performing linear fits of the delay as a function of redshift for each of the 29 defined energy bins. Examples for three energy bins, 28.57–30.38 MeV, 64.09–70.01 MeV, and 201.86–231.51 MeV are shown in figures 6.1, 6.2, and 6.3. Among these, only the plot in figure 6.2 displays a clear linear increasing trend, however, delays span in orders of seconds. In contrast, the plot in figure 6.3 exhibits a decreasing trend, which corresponds to the theoretical prediction but with the opposite sign of the parameter η. Most of the remaining cases, including that shown in figure 6.1, appear to exhibit a random distribution of delay values with respect to redshift, rather than any systematic increase. All 29 estimated slopes, along with their associated uncertainties, can be found in the table 6.3. A χ^2 test was additionally performed to evaluate the agreement between the experimental results and the linear model. Based on the values of the reduced chi-squared, which is a χ^2 divided by degrees of freedom (DoF), it is evident that the linear model does not adequately describe the data in most cases. This outcome is understandable, given the largely random nature of the delay distributions across energy bins.

In the final step, we plotted slope values as a function of mean bin energy. The resulting plot is provided in figure 6.4. A linear fit to the data yielded a slope of $(7.00 \pm 9.01) \times$

10^{-4} s/MeV, where the uncertainty exceeds the value of the slope itself. As a result, the final slope value corresponds to a statistical significance of only 0.8σ, and is therefore consistent with the absence of any systematic trend. After performing a χ^2 test, the following values were obtained: $\chi^2 = 298.31$, DoF $= 27$, resulting in a reduced χ^2 value of $\chi^2/\text{DoF} = 11.05$. This indicates a significant deviation from the model, suggesting that the model is not compatible with the experimental data.

To further investigate the influence of the highest-energy bin, which spans a particularly wide interval, we repeated the linear fit excluding this bin (figure 6.5). The resulting slope slightly changed to $(1.81 \pm 1.53) \times 10^{-3}$ s/MeV, uncovering a positive trend, however, the result remains statistically insignificant, corresponding to a significance of only 1.2σ. The fit quality worsened, as indicated by the χ^2 test results: $\chi^2 = 404.73$, DoF $= 26$, and a reduced χ^2 value of $\chi^2/\text{DoF} = 15.57$, pointing to stronger incompatibility between the model and the data.
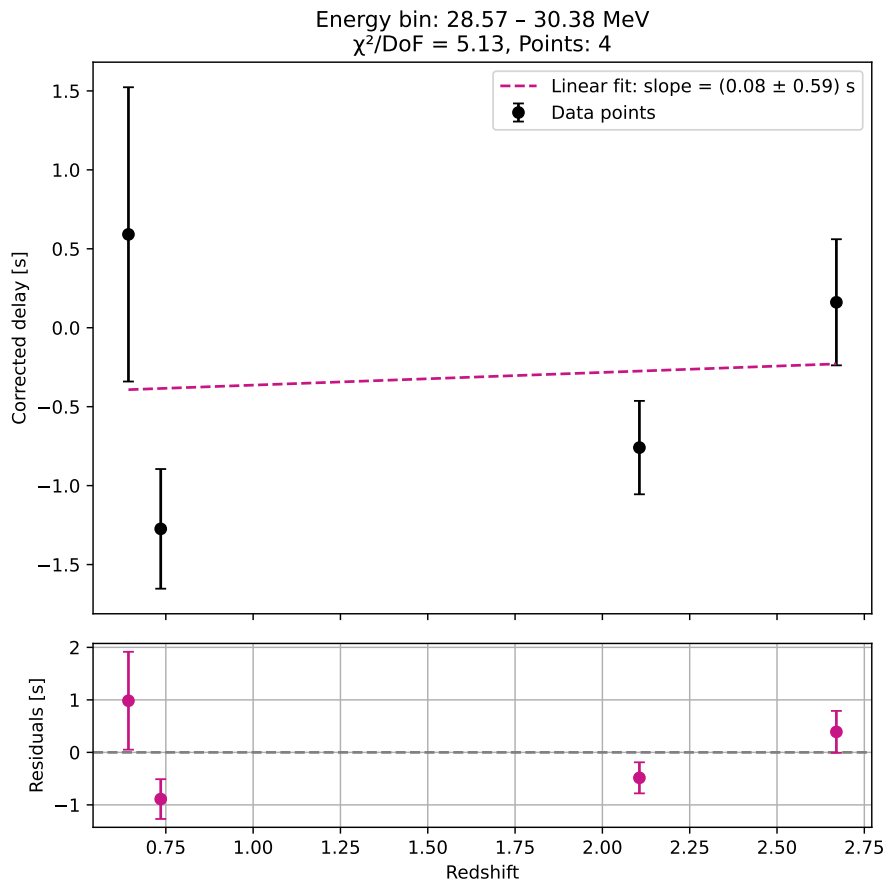
Figure 6.1: The cosmologically corrected delays for the energy bin 28.57–30.38 MeV plotted as a function of redshift. The distribution appears to be random across the range of redshifts, with no evident systematic trend. A linear fit was performed, and the resulting slope uncertainty exceeded the slope value itself, highlighting the inconclusiveness of the result. It is important to emphasize that, unfortunately, this kind of random distribution was characteristic for the majority of the energy bins analyzed.
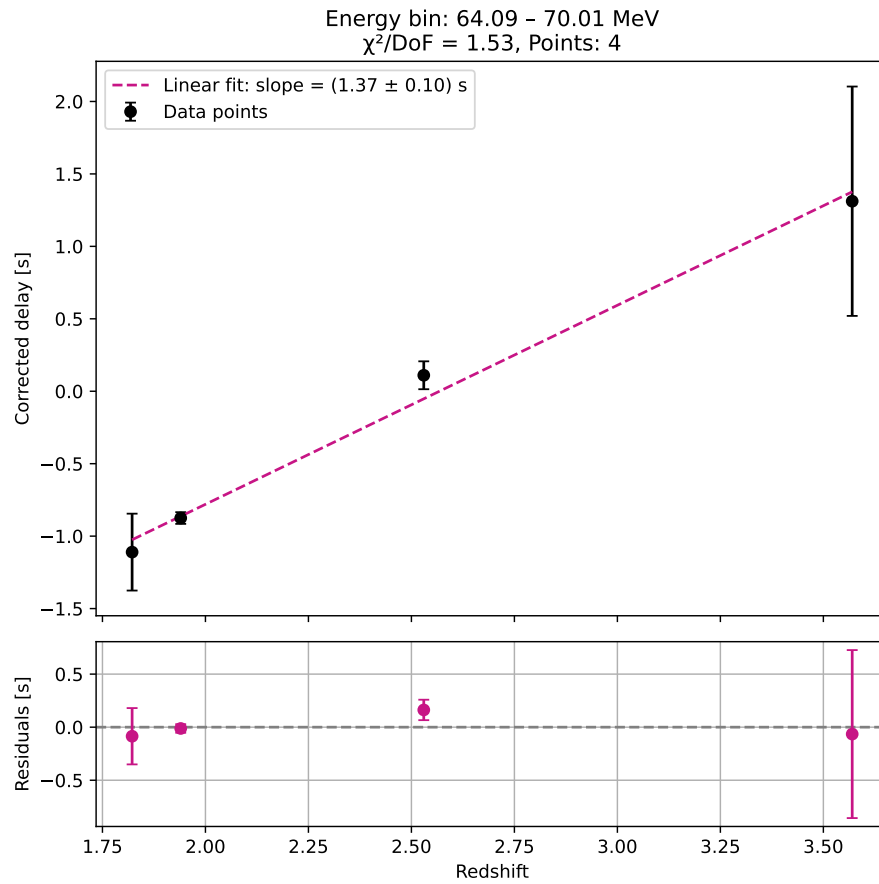
Figure 6.2: The cosmologically corrected delays for the energy bin 64.09–70.01 MeV plotted as a function of redshift. After performing a linear fit and a reduced χ^2 test, we ended up with a value of reduced $\chi^2 = 1.53$, representing the most satisfactory fit among all the analyzed energy bins. However, quantum gravity-induced time delays for this energy range are expected to be on the order of 10^{-3} seconds, indicating that our observed delays may have a different origin. This idea is also supported by the fact that, for the first two redshifts, the estimated delays are negative, which is in contradiction with the expected behavior in the subluminal scenario of quantum gravity phenomenology.
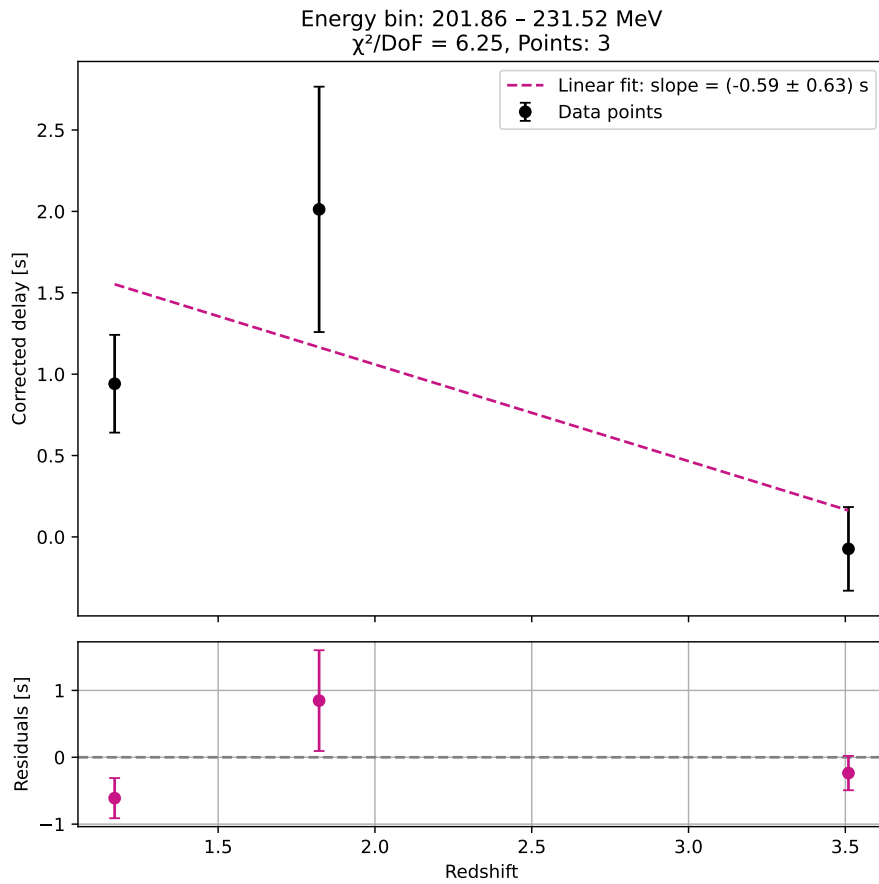
Figure 6.3: The cosmologically corrected delays for the energy bin 201.86–231.52 MeV plotted as a function of redshift. In this high-energy example, only three delays were adopted in the interval, due to a limited number of estimated delays. The distribution of the delays suggests a negative trend, however, taking into consideration the slope value with its associated uncertainty, we may conclude that we see a random distribution of delays, without being able to precisely comment on an increase or decrease of the delay values.

Table 6.3: A table of the 29 selected energy bins. For each bin, the table lists the slope obtained from a linear fit along with its corresponding uncertainty, as well as the number of data points presented in the bin. Additionally, the reduced χ^2 value is provided for each case, offering insight into the compatibility between the experimental data and the linear model.

Energy bin [MeV]	Slope [s]	Slope error [s]	$\frac{\chi^2}{\text{DoF}}$	Number of points
8.41–17.33	0.13	3.53	2836.95	3
18.37–20.48	-5.22	17.12	7.36	3
20.69–24.46	-0.43	0.31	13.15	4
25.90–26.87	-0.21	0.12	864.87	4
28.57–30.38	0.08	0.59	5.13	4
30.55–31.21	0.76	0.59	68.69	4
32.49–35.10	-0.13	0.26	41.37	4
36.52–40.14	-0.87	0.50	104.84	4
42.68–45.64	0.21	0.34	5.75	4
45.72–48.53	0.04	0.28	3.39	4
49.16–52.43	0.01	0.59	967.66	4
54.46–57.81	0.30	0.75	2883.19	4
59.97–63.77	-0.46	0.35	49.32	4
64.09–70.01	1.37	0.10	1.53	4
70.54–77.59	-0.26	0.03	1.26	4
78.84–89.58	-0.07	0.36	134.11	4
90.00–96.68	0.10	0.24	44.67	4
97.56–101.83	-0.39	1.50	96.61	4
104.04–113.46	-0.10	0.03	0.34	4
116.42–130.48	0.03	0.36	839.16	4
133.81–152.32	0.03	0.15	6.01	4
157.01–180.31	-0.07	0.17	16.82	4
185.91–199.61	-0.08	0.24	8.23	4
201.86–231.52	-0.59	0.63	6.25	3
235.15–264.19	-0.04	0.01	0.25	3
298.63–382.73	0.35	0.37	13.49	3
408.27–512.54	1.28	2.00	330.56	3
524.92–649.81	-0.10	0.23	25.54	3
701.34–1775.67	-0.05	2.43	324.43	3
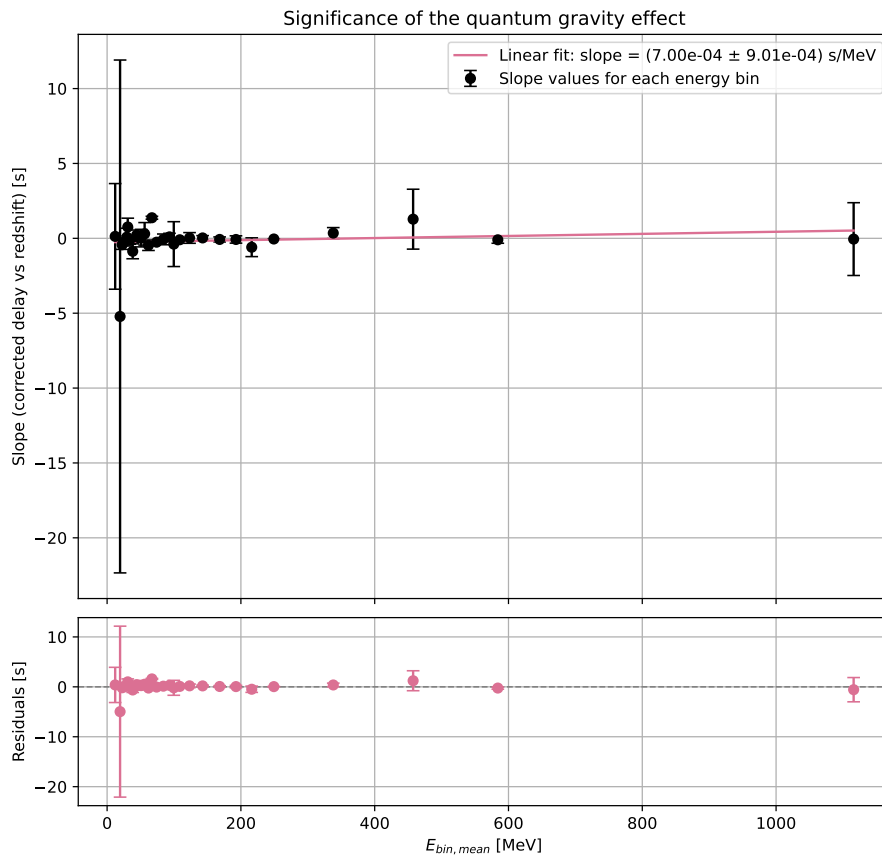
Figure 6.4: Final experimental result of slopes plotted as a function of mean bin energy. According to theory, delays should exhibit an increasing linear trend with both redshift and energy. However, taking into account the final slope value and its associated uncertainty, we conclude that no systematic trend is observed. Moreover, since the uncertainty exceeds the value of the slope itself, the trend may be positive, negative, or statistically consistent with zero. The corresponding significance of the result is approximately 0.8σ, indicating a lack of statistical significance. Additionally, we tried to fit the slope values excluding the highest-energy data point (figure 6.5), to evaluate whether the final slope value would show any improvement. The results of the corresponding χ^2 test are as follows: $\chi^2 = 298.31$, DoF $= 27$, and a reduced χ^2 value of $\chi^2/\text{DoF} = 11.05$.
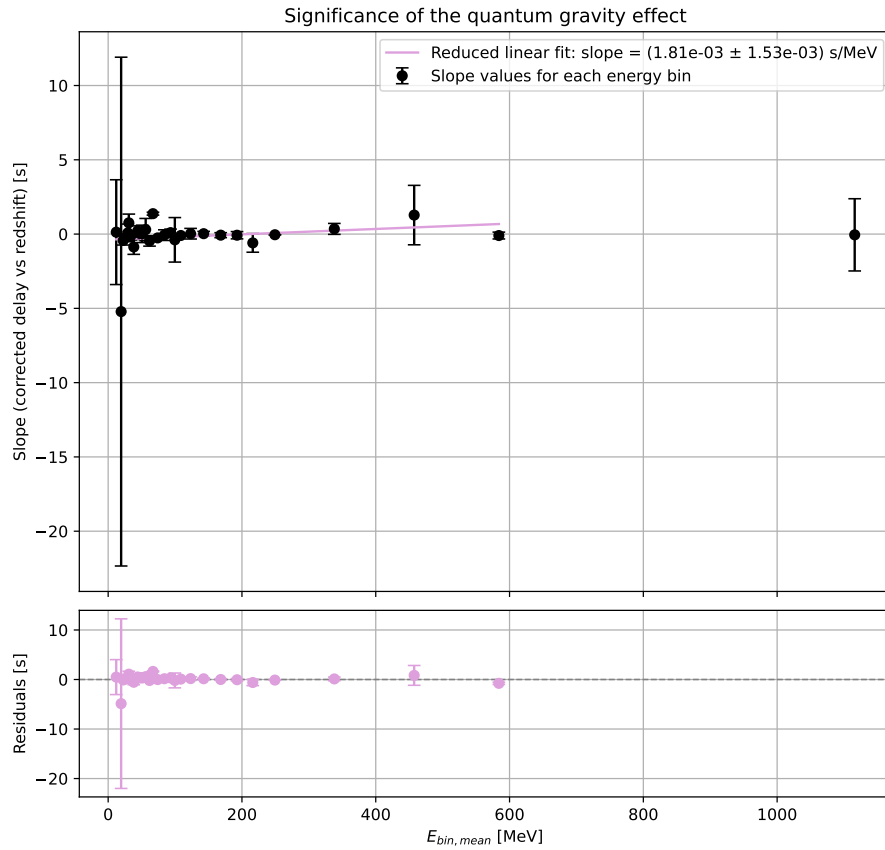
Figure 6.5: Final experimental result of slopes plotted as a function of mean bin energy, fitted with the linear regression, and excluding the last, highest-energy point from the linear fit. The uncertainty and the slope value slightly improved to $(1.81 \pm 1.53) \times 10^{-3}$ s/MeV. The result corresponds to a significance of approximately 1.2σ and therefore, also does not provide statistically significant evidence for a trend. The results of the corresponding χ^2 test worsened as follows: $\chi^2 = 404.73$, DoF $= 26$, and a reduced χ^2 value of $\chi^2/\text{DoF} = 15.57$.

6.2   Theory comparison

The essential step in adopting a position on the observability of quantum gravity-induced time delays is the comparison between our experimental results, presented in figure 6.4, and the theoretical predictions. Firstly, we calculated all τ_{QG} values using equation 1.10, adopting the parameters $n = 1$, $\eta = 1$ (subluminal scenario), $E_{QG} = E_{Pl} = 1.22 \times 10^{22}$ MeV, and cosmological parameters H_0, Ω_m and Ω_Λ were adopted from the work of Planck Collaboration et al. (2020). For each GRB and its corresponding energy interval, we set $E_l = 0$, while E_h was taken as the geometric mean of the lower and upper edges of the energy interval, and z was substituted with the GRB redshift. This approach allowed us to compute a theoretical delay τ_{QG} for each experimentally estimated delay. In order to enable a direct comparison, the theoretical delays were processed using the same methodology as the experimental ones. They were grouped into the same energy bins, plotted as a function of redshift for each bin, fitted with a linear model, and the resulting slopes were plotted as a function of the mean energy of each bin. This procedure allows us to identify possible deviations between the experimental measurements and the theoretical expectations, under identical processing conditions.

The theoretical analogy to table 6.3 is presented in table 6.4. Each energy bin includes information about the slope value and slope uncertainty, together with the number of theoretical delays used in each energy bin (identical to the number of delays used in the corresponding experimental part). Additionally, we provide three examples corresponding to the energy bins 28.57–30.38 MeV (figure 6.6), 64.09–70.01 MeV (figure 6.7), and 201.86–231.52 MeV (figure 6.8). In all cases, a clear increasing linear trend is observed, with the orders of theoretical delays ranging from 10^{-3} seconds to 10^{-2} seconds.
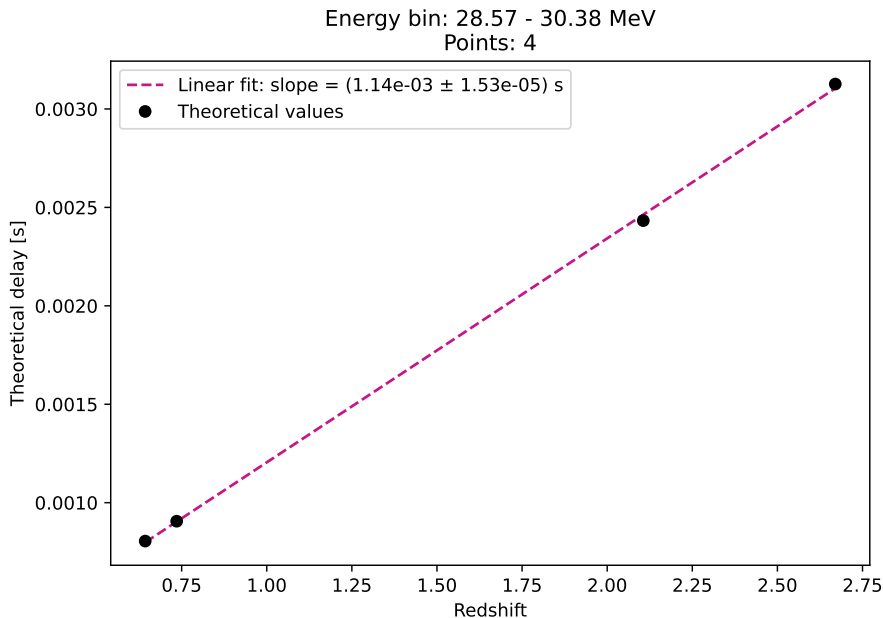
Figure 6.6: Theoretical delays for the energy bin 28.57–30.38 MeV plotted as a function of redshift. A clear increasing linear trend is observed, which differs significantly from the lack of a systematic trend in the experimental data presented in figure 6.1.
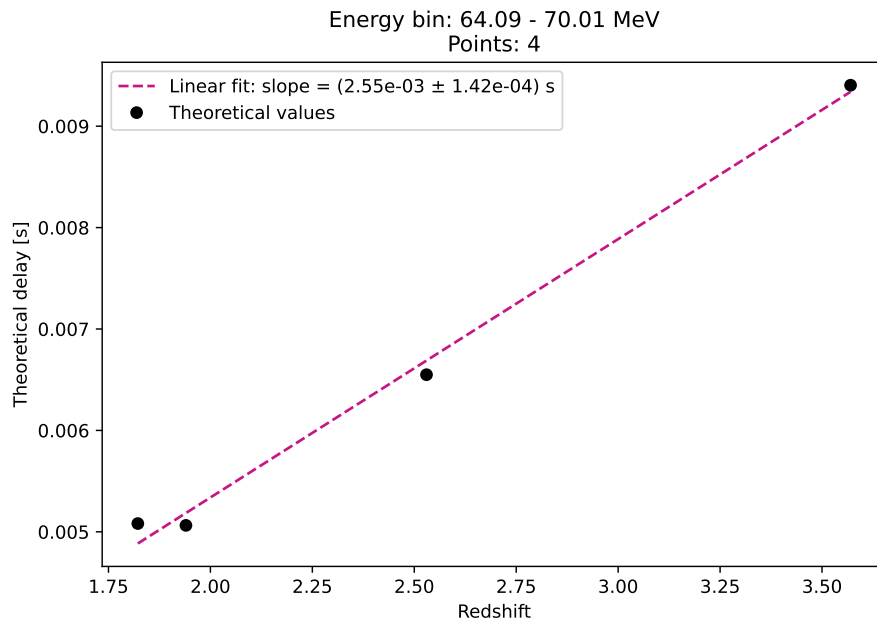
Figure 6.7: Theoretical delays for the energy bin 64.09–70.01 MeV plotted as a function of redshift. A clear increasing linear trend is observed, similar to figure 6.2. However, the orders of the theoretical and experimental delays differ significantly, with the experimental values being approximately two orders of magnitude in seconds larger than the theoretical predictions. Consequently, no conclusive evidence for quantum gravity-induced time delays is identified, suggesting that the observed delays are likely influenced by other factors.
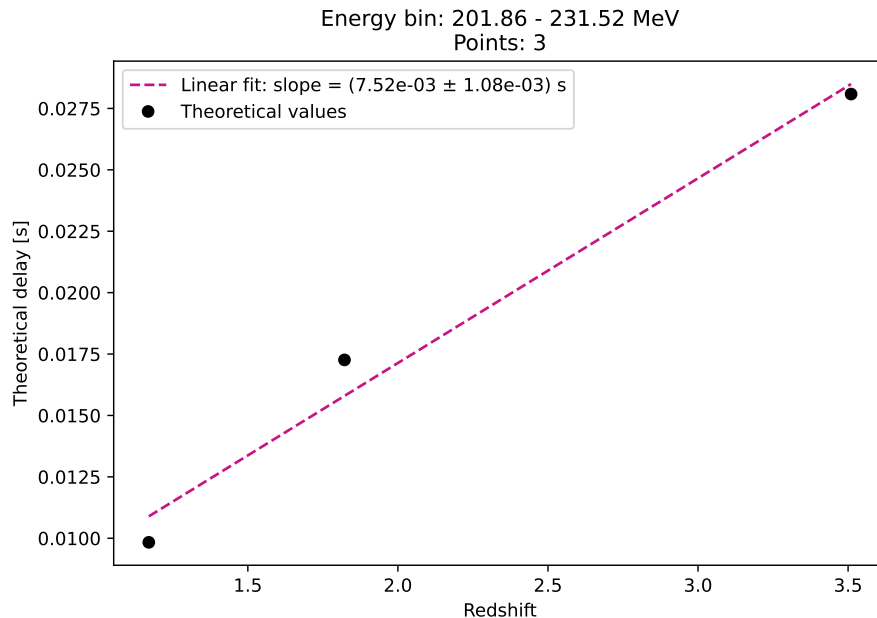

Figure 6.8: Theoretical delays for the energy bin 201.86–231.52 MeV plotted as a function of redshift. A clear increasing linear trend is observed, which is in contradiction with the experimental results shown in figure 6.3.

Table 6.4: A table of the selected 29 energy bins. For each bin, the table lists the slope obtained from a linear fit along with its corresponding uncertainty, as well as the number of theoretical delays included in the bin. These theoretical values were calculated from the relation 1.10.

Energy bin [MeV]	Slope [s]	Slope error [s]	Number of points
8.41–17.33	9.40×10^{-4}	2.23×10^{-4}	3
18.37–20.48	1.06×10^{-3}	5.37×10^{-4}	3
20.69–24.46	9.37×10^{-4}	9.07×10^{-5}	4
25.90–26.87	1.04×10^{-3}	2.54×10^{-5}	4
28.57–30.38	1.14×10^{-3}	1.53×10^{-5}	4
30.55–31.21	1.21×10^{-3}	2.88×10^{-5}	4
32.49–35.10	1.34×10^{-3}	8.48×10^{-5}	4
36.52–40.14	1.31×10^{-3}	1.47×10^{-4}	4
42.68–45.64	1.69×10^{-3}	1.05×10^{-4}	4
45.72–48.53	1.90×10^{-3}	5.95×10^{-5}	4
49.16–52.43	1.96×10^{-3}	1.08×10^{-4}	4
54.46–57.81	1.94×10^{-3}	1.17×10^{-4}	4
59.97–63.77	2.45×10^{-3}	1.60×10^{-4}	4
64.09–70.01	2.55×10^{-3}	1.42×10^{-4}	4
70.54–77.59	2.88×10^{-3}	6.38×10^{-5}	4
78.84–89.58	2.95×10^{-3}	3.84×10^{-4}	4
90.00–96.68	3.19×10^{-3}	6.05×10^{-5}	4
97.56–101.83	3.39×10^{-3}	2.78×10^{-4}	4
104.04–113.46	3.81×10^{-3}	6.12×10^{-5}	4
116.42–130.48	4.62×10^{-3}	3.12×10^{-4}	4
133.81–152.32	5.47×10^{-3}	1.56×10^{-4}	4
157.01–180.31	7.05×10^{-3}	4.49×10^{-4}	4
185.91–199.61	7.83×10^{-3}	2.88×10^{-4}	4
201.86–231.52	7.52×10^{-3}	1.08×10^{-3}	3
235.15–264.19	8.80×10^{-3}	3.32×10^{-5}	3
298.63–382.73	8.67×10^{-3}	2.02×10^{-3}	3
408.27–512.54	1.39×10^{-2}	9.20×10^{-4}	3
524.92–649.81	2.34×10^{-2}	4.41×10^{-3}	3
701.34–1775.67	9.23×10^{-2}	2.22×10^{-2}	3

In the final step of the theoretical part, the resulting slope values were plotted as a function of the mean energy of each bin, as shown in figure 6.9. Two linear fits were performed, one including all the theoretical slope values, and a second excluding the highest-energy point, as was similarly done in the experimental part. In both cases, the slope values are on the order of 10^{-5} s/MeV, with corresponding uncertainties in the order of 10^{-6} s/MeV. These values are approximately one order smaller than those obtained from the experimental data (or two orders smaller when considering the reduced linear fit).

The comparison between experimental and theoretical slopes indicates that additional effects are likely present in the observational data, potentially dominating over the time

delays predicted by quantum gravity. A more detailed discussion on the observability of quantum gravity-induced time delays is provided in the following section.

Although we adopted a linear quantum gravity correction, $n = 1$, which implies a linear dependence of the slope on energy, the distribution of the theoretically computed slope values showed a slight curvature, mostly because of the last, highest-energy bin. This motivated us to also apply a quadratic regression, which yielded a better fit to the theoretical trend. However, since our model assumes a linear energy dependence, the improved performance of the quadratic fit is likely a numerical artifact rather than a physically motivated discrepancy.
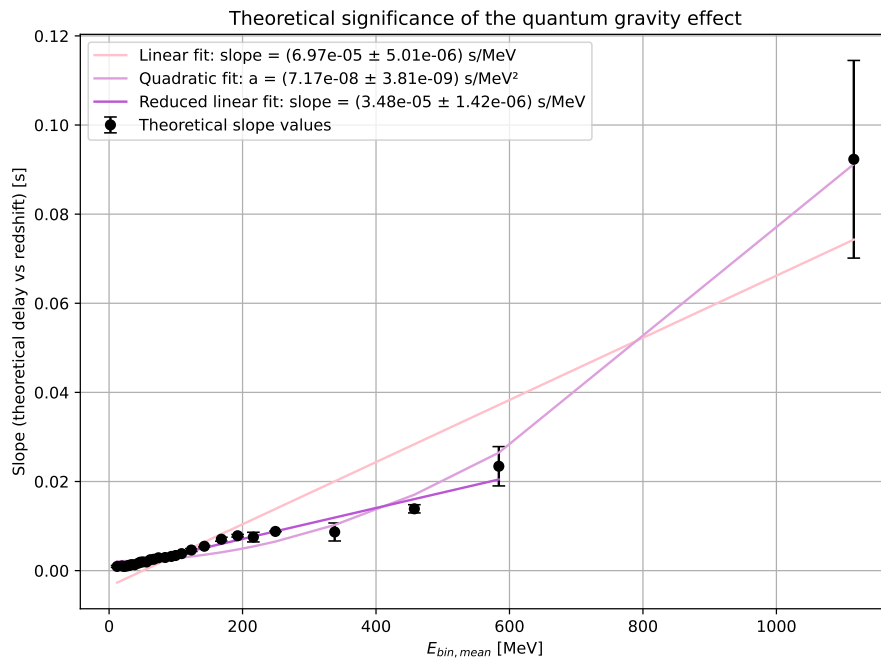

Figure 6.9: The theoretical slope values plotted as a function of mean bin energy. In total, three fits were applied to the slope values. The first, linear fit, yields a slope that is one order smaller than the corresponding experimental slope shown in 6.4. A reduced linear fit excluding the highest-energy point differs from the reduced experimental fit in figure 6.5 by two orders of magnitude in s/MeV. This comparison between theoretical predictions and experimental results leads to the conclusion that quantum gravity-induced time delays are not observable in the data. Moreover, the significant discrepancy in slope magnitudes suggests the possible presence of secondary effects dominating in the data. Although the quadratic coefficient a and its uncertainty are provided in the figure legend, the quadratic fit is not physically motivated, as the theoretical delays were computed assuming a linear dependence ($n = 1$).

6.3 Significance of the quantum gravity effect

We analyzed and estimated time delays between the Fermi-GBM and Fermi-LLE/Fermi-LAT instruments for a sample of 23 GRBs, using the HERMES delays software. The resulting time delays were investigated as a function of both redshift and energy, as shown in figure 6.4. The final slope obtained from the linear fit is $(7.00 \pm 9.01) \times 10^{-4}$ s/MeV,

corresponding to a statistical significance of 0.8σ. The reduced χ^2 value of the fit is $\chi^2/\mathrm{DoF} = 11.05$. Additionally, we excluded the last, highest energy bin from the analysis in figure 6.5. The final slope value improved to $(1.81 \pm 1.53) \times 10^{-3}$ s/MeV, corresponding to a statistical significance of 1.2σ. The reduced χ^2 value increased to $\chi^2/\mathrm{DoF} = 15.57$, indicating a worse fit quality. Considering both the low statistical significance and the results of the χ^2 tests, we conclude that our analysis does not provide statistically significant evidence supporting the existence of a quantum gravity-induced time delay effect.

Furthermore, we compared our experimental results to theoretical predictions derived from the generally accepted time delay relation 1.10, considering the first-order (linear) correction with $n = 1$. The theoretical significance of the quantum gravity effect is presented in figure 6.9. The resulting slope from the linear fit of the theoretical model is $(6.97 \pm 0.50) \times 10^{-5}$ s/MeV. When excluding the highest-energy point, the slope further decreases to $(3.48 \pm 0.14) \times 10^{-5}$ s/MeV. In comparison with the experimental slopes obtained from the Fermi data analysis, the theoretical predictions are approximately one order smaller, or even two orders smaller when excluding the highest-energy bin. Moreover, after comparing the 28.57–30.38 MeV, 64.09–70.01 MeV, and 201.86–231.52 energy bin examples, the theory expects a clear linear increase of time delays from orders of 10^{-3} seconds to 10^{-2} seconds, while the experimentally measured time delays exhibit a largely random distribution, and range in orders of seconds.

The outcome of the experiment may have multiple explanations. One of the potential sources of the observed time delays could arise from instrumental effects related to the Fermi detectors themselves. Nevertheless, it is important to emphasize that the Fermi Gamma-ray Space Telescope currently represents one of the most advanced and precise instruments available for the detection of high-energy astrophysical transients. The most possible explanation for the observed time delays, however, lies in the intrinsic lags of the gamma-ray bursts, as discussed in section 2.5.1. Due to their random nature and time scales in orders of seconds, intrinsic lags most possibly dominate in our dataset and directly prohibit us from observing any quantum gravity features.

Several possible approaches and methods for the future detectability of quantum gravity-induced time delays can be proposed. From an instrumentation perspective, improvements in the temporal resolution of detectors, along with increased sensitivity to a broader energy range, extending to very high energies in GeV, appear essential. Throughout our analysis, it became evident that, despite the Fermi telescope's energy coverage and time resolution, its ability to detect a sufficient number of photons at the highest energies was limited. This prevented us from enlarging our initial sample of GRBs, consequently limiting the statistical power of our study. The recently launched HERMES satellites will, hopefully, provide a breakthrough in the future. Regarding the issue of intrinsic lags, their removal from observational data remains unattainable, as their physical origin is still not understood by the scientific community. Nevertheless, we propose to enlarge the analyzed GRB sample to hundreds, or thousands of events. To reach a statistical significance of 3σ, compared to our current result of 0.8σ based on 29 energy bins, we estimate that approximately 408 energy bins would be required. Assuming an average of 4 delay measurements per bin, this corresponds to more than 1600 delays. For a discovery-level significance of 5σ, the required number of bins rises to approximately 1133, which would require more than 4500 delays. These estimates suggest that achieving higher statistical significance requires the

analysis of a substantially larger GRB sample. Moreover, due to the random nature of intrinsic lags, a sufficiently large sample would allow these random effects to average out, increasing the chances of detecting the underlying quantum gravity effect.

Although our results do not confirm the presence of quantum gravity-induced time delay effect, the thesis contributes to the information about the current limits for the detectability of quantum gravity features. The limitations of current observational techniques and the lack of understanding of a GRB inner engine prevent the author from making a more definitive statement about the phenomenology of quantum gravity.

Conclusions

The aim of the work was to investigate possible manifestations of quantum gravity theory, a theory striving to unify the two pillars of modern physics – Einstein's general relativity and quantum mechanics. Although numerous mathematical models have been proposed, they all share a common feature of introducing the Planck scale as the threshold at which the standard physical model breaks down and the quantum nature of space-time emerges. We introduced several phenomenological models that combine theoretical concepts with experimental approaches, despite the lack of information about the fundamental theory. Phenomenological models lead to the formulation of the Planck-scale modified dispersion relation. We outlined how the modified dispersion relation can result in potentially observable effects, including energy-dependent arrival time delays for cosmic messengers such as photons, the search for which was the main focus of this thesis.

In the second chapter of the work, we introduced gamma-ray bursts as promising astrophysical tools for studying quantum gravity. The reason for this lies in their immense energy, although not reaching the Planck scale, their cosmological distances allow any potential quantum gravitational effects to accumulate as GRB photons travel through space-time. After the classification of GRBs and the description of the fireball model, we also addressed the issue of intrinsic lags, originating at the GRB sources themselves and causing photons of different wavelengths to be emitted at different times. Even if the question of intrinsic lags remains unanswered to this day, and therefore cannot be subtracted from the data, we rely on their key distinguishing feature, which is that the quantum gravity-induced time delays are dependent on redshift, whereas intrinsic spectral lags are not.

The following chapter was dedicated to current GRB instruments. We reviewed both space-based and ground-based detectors, with particular focus on GRBAlpha, the Fermi Gamma-Ray Space Telescope, the HERMES-TP/SP mission, and ground-based Cherenkov telescopes. The capability of each telescope to search for quantum gravity-induced time delays was discussed, placing emphasis on the energy range detection capability, temporal resolution, and the (in)direct nature of the detection technique. Based on this comparison, we selected data from the Fermi telescope for use in the experimental part of this work.

The search for time delays between different energy bands in the Fermi GRB data was conducted using the HERMES delays software, based on the cross-correlation technique and repeated random splitting. A detailed description of the software, together with the specific approach to light curve construction and selection of a relation for a sufficient energy range width, was provided in the fourth chapter. In the next chapter, we presented the data analysis process. After a proper selection of all GRBs with known redshift detected by at least two of the three Fermi detectors since Fermi's launch in June 2008, until

September 2024, we selected the suitable energy ranges for each GRB and each pair of detectors, and conducted the analysis. It is important to emphasize that the initial dataset needed to be reduced due to several reasons, including GRBs being detected by only one of the three detectors, or due to the lack of data in chosen energy range widths, making a final number of 23 analyzed GRBs.

In the final chapter, we presented our experimental results. All experimentally obtained time delays were corrected for cosmological effects and grouped into energy bins. The final result contained experimental time delays plotted as a function of both redshift and mean bin energy, with linear regression applied. Two final plots were presented, one including all energy bins, and one excluding the last, highest energy bin. Finally, the experimental results were compared with theoretical values derived from the introduced quantum gravity time delay formula. Results show the lack of statistical significance, consequently providing no evidence for the presence of the quantum gravity-induced time delays in the data. The most plausible explanation for this outcome is the presence of intrinsic lags, which are orders of magnitude larger than the expected quantum gravity-induced time delays. However, since the origin of intrinsic lags is still not understood by the scientific community and cannot be subtracted from the data, for future studies, we propose to radically enlarge the sample of analyzed GRBs. Assuming that intrinsic lags are random in nature, a sufficiently large sample, on the order of hundreds or thousands of GRBs, could cause the intrinsic effects to average out, potentially revealing redshift-dependent time delays induced by quantum gravity.

Although no definitive evidence of quantum gravity-induced time delays was found in this work, our analysis has contributed to identifying key challenges that must be addressed in future studies within this young and evolving field, such as the need to better understand the formation of intrinsic lags, to explore the GRB inner engine in greater detail, and to improve instrumental capabilities. Furthermore, we have placed constraints on the possible magnitude of quantum gravity-induced delays, excluding the manifestation of such effects down to the order of seconds. While the true nature of space-time remains unknown, this work represents a small step forward along a path that humankind shall continue to explore, until one day, hopefully, it is finally understood.

Appendix A

Appendix A consists of four tables containing information regarding the GRBs with known redshifts detected from June 2008 until September 2024 by the Fermi Gamma-Ray Space Telescope. Each row includes the GRB name, the corresponding identifier in the bn format, the trigger time in Mission Elapsed Time (MET), right ascension and declination in degrees, redshift, and information regarding the detection and data availability from the LAT, GBM, and LLE instruments.

In two cases, GRB 181201A and GRB 210822A, the Fermi GBM did not detect the bursts, preventing the identification of the corresponding bn identifier and the trigger time in Mission Elapsed Time (MET). These entries are marked with a dash (–). For GRB 090102 and GRB 210822A, the trigger time is provided in UTC instead. In general, the sky positions were retrieved from Fermi-LAT GCN circulars. However, when unavailable, the positions were taken from Fermi-GBM circulars. The trigger time was also taken from the GCN circulars. In three cases, GRB 130925A, GRB 190829A, and GRB 201216C, the number of detected counts was below the trigger threshold, resulting in a reduced observed flux. These cases are marked in the LAT column as no (upper limit). In one instance, GRB 120711A, although the detection was announced in a Fermi-LAT GCN circular, the corresponding trigger time window contained no data. This case is marked in the LAT column as yes (no data).

In the cases of GRB 150403A and GRB 110721A, two redshift values were proposed in the reference paper. To represent the redshift in our analysis, we used the mean of the two values. The associated uncertainty was defined as half of the difference between the proposed values.

Table 7.5: Table of GRBs with known redshift detected by the Fermi Gamma-ray Space Telescope from its launch until the end of 2014. Each entry includes the GRB name, the corresponding identifier in the bn format, the trigger time in Mission Elapsed Time (MET), and the sky position (right ascension and declination) in degrees.

GRB name	bn name	Trigger time [MET]	RA [°]	DEC [°]
GRB 080916C	bn080916009	243216766	121.8	-61.3
GRB 081024B	bn081024891	246576161	322.9	+21.2
GRB 090102	bn090102122	02:55:30	128.20	+33.10
GRB 090323	bn090323002	259459364	190.69	+17.08
GRB 090328	bn090328401	259925808	90.87	-41.95
GRB 090510	bn090510016	263607783	333.400	-26.767
GRB 090902B	bn090902462	273582310	264.5	+26.5
GRB 090926A	bn090926181	275631628	353.56	-66.34
GRB 091003A	bn091003191	276237347	251.39	+36.58
GRB 091024	bn091024380	278067360	339.207	+56.874
GRB 091127	bn091127976	281057147	36.571	-18.954
GRB 100414A	bn100414097	292904423	191.59	+8.57
GRB 100724B	bn100724029	301624927	124.16	+74.42
GRB 100728A	bn100728095	301976252	88.743	-15.262
GRB 100728B	bn100728439	302005916	44.053	+0.280
GRB 110213A	bn110213220	319267033	43.004	+49.291
GRB 110721A	bn110721200	332916465	333.4	-39.0
GRB 110731A	bn110731465	333803371	280.39	-28.53
GRB 120624B	bn120624933	362269436	170.73	+9.48
GRB 120711A	bn120711115	363667496	94.7	-70.9
GRB 120729A	bn120729456	365252175	13.056	+49.940
GRB 130427A	bn130427324	388741629	173.139	+27.692
GRB 130518A	bn130518580	390578080	355.809	+47.641
GRB 130702A	bn130702004	394416326	216.4	+15.8
GRB 130925A	bn130925164	401774969	41.17877	-26.15300
GRB 131108A	bn131108862	405636118	156.47	+9.90
GRB 131231A	bn131231198	410157919	10.585	-1.845
GRB 140206B	bn140206275	413361375	315.26	-8.51
GRB 140619B	bn140619475	424869883	132.68	-9.66
GRB 141028A	bn141028455	436186489	322.70	-0.28

Table 7.6: Table of GRBs with known redshift detected by the Fermi Gamma-ray Space Telescope from 2015 until September 2024. Each entry includes the GRB name, the corresponding identifier in the bn format, the trigger time in Mission Elapsed Time (MET), and the sky position (right ascension and declination) in degrees.

GRB name	bn name	Trigger time [MET]	RA [°]	DEC [°]
GRB 150314A	bn150314205	448001693	125.40	+64.46
GRB 150403A	bn150403913	449790853	311.79	-62.76
GRB 150514A	bn150514774	453321308	74.85	-60.91
GRB 151027A	bn151027166	467611108	272.491	+61.381
GRB 160509A	bn160509374	484477130	310.1	+76.0
GRB 160623A	bn160623209	488350837	315.24	+42.27
GRB 160625B	bn160625945	488587220	308.3	+6.9
GRB 160821A	bn160821857	493504474	172.5	+43.0
GRB 170214A	bn170214649	508779271	256.33	-1.88
GRB 170405A	bn170405777	513110367	219.37	-25.23
GRB 171010A	bn171010792	529354855	66.74	-10.53
GRB 180703A	bn180703876	552344505	6.5	-67.1
GRB 180720B	bn180720598	553789304	0.58	-2.95
GRB 181020A	bn181020792	561754838	14.1	-47.3
GRB 181201A	–	–	319.28	-12.60
GRB 190114C	bn190114873	569192227	54.57	-26.99
GRB 190829A	bn190829830	588801358	45.6	-7.1
GRB 200524A	bn200524211	611989445	212.8	+61.0
GRB 200613A	bn200613229	613719013	153.03	+45.85
GRB 201020B	bn201020732	624908039	74.9	+77.0
GRB 201216C	bn201216963	629852850	17.9	+16.8
GRB 210619B	bn210619999	645839970	319.7	+33.9
GRB 210822A	–	09:18:18	304.6	+4.9
GRB 211023A	bn211023546	656687148	72.3	+85.3
GRB 220101A	bn220101215	662706616	1.52	+31.75
GRB 220527A	bn220527387	675335840	323.6	-14.9
GRB 220627A	bn220627890	678057665	201.2	-32.5
GRB 221009A	bn221009553	687014224	288.21	+19.73
GRB 230812B	bn230812790	713559497	250.1	+46.2
GRB 240825A	bn240825662	746293985	341.6	+5.9

Table 7.7: Table of GRBs with known redshift detected by the Fermi Gamma-ray Space Telescope from its launch until the end of 2014. Each entry includes the GRB name, redshift, and information regarding the detection and data availability from the LAT, GBM, and LLE instruments.

GRB name	Redshift	Fermi-LAT	Fermi-LLE	Fermi-GBM
GRB 080916C	4.35 ± 0.15 [1]	yes	yes	yes
GRB 081024B	2.56 ± 1.63 [2]	yes	yes	yes
GRB 090102	1.547 [3]	no	no	yes
GRB 090323	3.57 [4]	yes	yes	yes
GRB 090328	0.7354 ± 0.0003 [5]	yes	yes	yes
GRB 090510	0.903 ± 0.003 [6]	yes	yes	yes
GRB 090902B	1.822 [7]	yes	yes	yes
GRB 090926A	2.1062 ± 0.0004 [8]	yes	yes	yes
GRB 091003A	0.8969 [9]	yes	no	yes
GRB 091024	1.092 [10]	no	no	yes
GRB 091127	0.49 [11]	no	no	yes
GRB 100414A	1.368 [12]	yes	no	yes
GRB 100724B	1.00 [13]	yes	yes	yes
GRB 100728A	1.567 [14]	no	no	yes
GRB 100728B	2.106 [15]	no	no	yes
GRB 110213A	1.46 [16]	no	no	yes
GRB 110721A	1.94 ± 1.56 [17]	yes	yes	yes
GRB 110731A	2.83 [18]	yes	yes	yes
GRB 120624B	2.1974 ± 0.0002 [19]	yes	yes	yes
GRB 120711A	1.405 [20]	yes (no data)	no	yes
GRB 120729A	0.8 [21]	no	no	yes
GRB 130427A	0.338 ± 0.002 [22]	yes	yes	yes
GRB 130518A	2.49 [23]	yes	yes	yes
GRB 130702A	0.145 [24]	yes	no	yes
GRB 130925A	0.347 [25]	no (upper limit)	no	yes
GRB 131108A	2.4 [26]	yes	yes	yes
GRB 131231A	0.6439 [27]	yes	yes	yes
GRB 140206B	2.73 [28]	yes	yes	yes
GRB 140619B	2.67 [29]	yes	yes	yes
GRB 141028A	2.33 [30]	yes	yes	yes

Table 7.8: Table of GRBs with known redshift detected by the Fermi Gamma-ray Space Telescope 2015 until September 2024. Each entry includes the GRB name, redshift, and information regarding the detection and data availability from the LAT, GBM, and LLE instruments.

GRB name	Redshift	Fermi-LAT	Fermi-LLE	Fermi-GBM
GRB 150314A	1.758 [31]	yes	no	yes
GRB 150403A	1.91 ± 0.15 [32]	yes	yes	yes
GRB 150514A	0.807 [33]	yes	yes	yes
GRB 151027A	0.810 [34]	no	no	yes
GRB 160509A	1.17 [35]	yes	yes	yes
GRB 160623A	0.367 [36]	yes	no	yes
GRB 160625B	1.406 [37]	yes	yes	yes
GRB 160821A	0.4 [38]	yes	yes	yes
GRB 170214A	2.53 [39]	yes	yes	yes
GRB 170405A	3.510 [40]	yes	yes	yes
GRB 171010A	0.3285 [41]	yes	no	yes
GRB 180703A	0.6678 [42]	yes	no	yes
GRB 180720B	0.654 [43]	yes	yes	yes
GRB 181020A	2.935 [44]	yes	no	yes
GRB 181201A	0.45 [45]	yes	no	no
GRB 190114C	0.4245 ± 0.0005 [46]	yes	yes	yes
GRB 190829A	0.0785 [47]	no (upper limit)	no	yes
GRB 200524A	1.256 [48]	yes	no	yes
GRB 200613A	1.2277 ± 0.0011 [49]	yes	no	yes
GRB 201020B	0.804 [50]	yes	no	yes
GRB 201216C	1.10 [51]	no (upper limit)	no	yes
GRB 210619B	1.937 [52]	yes	no	yes
GRB 210822A	1.736 [53]	yes	no	no
GRB 211023A	0.3906 [54]	yes	no	yes
GRB 220101A	4.618 [55]	yes	yes	yes
GRB 220527A	0.857 [56]	yes	no	yes
GRB 220627A	3.08 [57]	yes	no	yes
GRB 221009A	0.15095 ± 0.00005 [58]	yes	no	yes
GRB 230812B	0.3602 ± 0.0006 [59]	yes	no	yes
GRB 240825A	0.659 [60]	yes	no	yes

References for Appendix A

1. Greiner, J., Clemens, C., Krühler, T., et al. 2009, Astronomy & Astrophysics, The redshift and afterglow of the extremely energetic gamma-ray burst GRB 080916C, 498, 1, 89. https://doi.org/10.1051/0004-6361/200811571

2. Aimuratov, Y., Ruffini, R., Bianco, C. L., et al. 2018, Fourteenth Marcel Grossmann Meeting - MG14, Analysis of the GRB 081024B, 2975. https://doi.org/10.1142/9789813226609_0374

3. Amati, L., Frontera, F., & Guidorzi, C. 2009, Astronomy & Astrophysics, Extremely energetic Fermi gamma-ray bursts obey spectral energy correlations, 508, 1, 173. doi:10.1051/0004-6361/200912788 https://doi.org/10.1051/0004-6361/200912788

4. Chornock, R., Perley, D. A., Cenko, S. B., et al. 2009, GRB Coordinates Network, Circular Service, No. 9028, #1 (2009), GRB 090323 Gemini-South redshift., 9028, 1. https://gcn.nasa.gov/circulars/9028

5. McBreen, S., Krühler, T., Rau, A., et al. 2010, Astronomy & Astrophysics, Optical and near-infrared follow-up observations of four Fermi/LAT GRBs: redshifts, afterglows, energetics, and host galaxies, 516, A71. https://doi.org/10.1051/0004-6361/200913734

6. Rau, A., McBreen, S., & Kruehler, T. 2009, GRB Coordinates Network, Circular Service, No. 9353, #1 (2009), GRB090510: VLT/FORS2 spectroscopic redshift., 9353, 1. https://gcn.nasa.gov/circulars/9353

7. Cucchiara, A., Fox, D. B., Tanvir, N., et al. 2009, GRB Coordinates Network, Circular Service, No. 9873, #1 (2009), GRB 090902B: Gemini-N absorption redshift., 9873, 1. https://gcn.nasa.gov/circulars/9873

8. Rau, A., Savaglio, S., Krühler, T., et al. 2010, The Astrophysical Journal, A Very Metal-poor Damped Lyman-α System Revealed Through the Most Energetic GRB 090926A, 720, 1, 862. https://doi.org/10.1088/0004-637X/720/1/862

9. Ackermann, M., Ajello, M., Asano, K., et al. 2013, The Astrophysical Journal Supplement Series, The First Fermi-LAT Gamma-Ray Burst Catalog, 209, 1, 11. https://doi.org/10.1088/0067-0049/209/1/11

10. Gruber, D., Greiner, J., von Kienlin, A., et al. 2011, Astronomy & Astrophysics, Rest-frame properties of 32 gamma-ray bursts observed by the Fermi Gamma-ray Burst Monitor, 531, A20. https://doi.org/10.1051/0004-6361/201116953

11. Cucchiara, A., Fox, D., Levan, A., et al. 2009, GRB Coordinates Network, Circular Service, No. 10202, #1 (2009), GRB 091127: Gemini-N redshift., 10202, 1. https://gcn.nasa.gov/circulars/10202

12. Urata, Y., Huang, K., Yamaoka, K., et al. 2012, Gamma-Ray Bursts 2012 Conference (GRB 2012), Energetic Fermi/LAT GRB100414A: Energetic and Correlations, 77. `https://doi.org/10.22323/1.152.0077`

13. Liu, T., Hou, S.-J., Xue, L., et al. 2015, The Astrophysical Journal Supplement Series, Jet Luminosity of Gamma-ray Bursts: the Blandford-Znajek Mechanism versus the Neutrino Annihilation Process, 218, 1, 12. `https://doi.org/10.1088/0067-0049/218/1/12`

14. Li, M.-H. & Lin, H.-N. 2015, The Astrophysical Journal, The Two-point Correlation Function of Gamma-Ray Bursts, 807, 1, 76. `https://doi.org/10.1088/0004-637X/807/1/76`

15. Lü, J., Zou, Y.-C., Lei, W.-H., et al. 2012, The Astrophysical Journal, Lorentz-factor-Isotropic-luminosity/Energy Correlations of Gamma-Ray Bursts and Their Interpretation, 751, 1, 49. `https://doi.org/10.1088/0004-637X/751/1/49`

16. D'Elia, V., Stratta, G., Kuin, N. P. M., et al. 2011, GCN Report, Swift Observation of GRB 110213A., 323, 1. `https://ui.adsabs.harvard.edu/abs/2011GCNR..323....1D/abstract`

17. Iyyani, S., Ryde, F., Axelsson, M., et al. 2013, Monthly Notices of the Royal Astronomical Society, Variable jet properties in GRB 110721A: time resolved observations of the jet photosphere, 433, 4, 2739. `https://doi.org/10.1093/mnras/stt863`

18. Ackermann, M., Ajello, M., Asano, K., et al. 2013, The Astrophysical Journal, Multiwave-length Observations of GRB 110731A: GeV Emission from Onset to Afterglow, 763, 2, 71. `https://doi.org/10.1088/0004-637X/763/2/71`

19. de Ugarte Postigo, A., Campana, S., Thöne, C. C., et al. 2013, Astronomy & Astrophysics, The obscured hyper-energetic GRB 120624B hosted by a luminous compact galaxy at z = 2.20, 557, L18. `https://doi.org/10.1051/0004-6361/201322065`

20. Giuliani, A. & Mereghetti, S. 2014, Astronomy & Astrophysics, A search for lines in the bright X-ray afterglow of GRB 120711A, 563, A6. `https://doi.org/10.1051/0004-6361/201321604`

21. Tanvir, N. R. & Ball, J. 2012, GRB Coordinates Network, Circular Service, No. 13532, #1 (2012), GRB 120729A Gemini-N redshift., 13532, 1. `https://gcn.nasa.gov/circulars/13532`

22. Xu, D., de Ugarte Postigo, A., Schulze, S., et al. 2013, GRB Coordinates Network, Circular Service, No. 14478, #1 (2013), GRB 130427A: NOT optical photometry and redshift., 14478, 1. `https://gcn.nasa.gov/circulars/14478`

23. Sanchez-Ramirez, R., Gorosabel, J., Castro-Tirado, A. J., et al. 2013, GRB Coordinates Network, Circular Service, No. 14685, #1 (2013), GRB 130518A: 10.4m GTC/OSIRIS redshift., 14685, 1. `https://gcn.nasa.gov/circulars/14685`

24. Schulze, S., Yaron, O., Sollerman, J., et al. 2021, The Astrophysical Journal Supplement Series, The Palomar Transient Factory Core-collapse Supernova Host-galaxy Sample. I. Host-galaxy Distribution Functions and Environment Dependence of Core-collapse Supernovae, 255, 2, 29. https://doi.org/10.3847/1538-4365/abff5e

25. Margutti, R., Guidorzi, C., Lazzati, D., et al. 2015, The Astrophysical Journal, Dust in the Wind: the Role of Recent Mass Loss in Long Gamma-Ray Bursts, 805, 2, 159. https://doi.org/10.1088/0004-637X/805/2/159

26. Giuliani, A., Mereghetti, S., Marisaldi, M., et al. 2014, A prompt extra component in the high energy spectrum of GRB 131108A, arXiv:1407.0238v1 https://doi.org/10.48550/arXiv.1407.0238

27. Cucchiara, A. 2014, GRB Coordinates Network, Circular Service, No. 15652, #1 (2014), GRB 131231A: gemini-south redshift., 15652, 1. https://gcn.nasa.gov/circulars/15652

28. Li, L. 2019, The Astrophysical Journal Supplement Series, Multipulse Fermi Gamma-Ray Bursts. I. Evidence of the Transition from Fireball to Poynting-flux-dominated Outflow, 242, 2, 16. https://doi.org/10.3847/1538-4365/ab1b78

29. Zhang, Z. B., Zhang, C. T., Zhao, Y. X., et al. 2018, Publications of the Astronomical Society of the Pacific, Spectrum-energy Correlations in GRBs: Update, Reliability, and the Long/Short Dichotomy, 130, 987, 054202. https://doi.org/10.1088/1538-3873/aaa6af

30. Xu, D., Levan, A. J., Fynbo, J. P. U., et al. 2014, GRB Coordinates Network, Circular Service, No. 16983, #1 (2014), GRB 141028A: VLT/X-shooter redshift of z=2.33., 16983, 1. https://gcn.nasa.gov/circulars/16983

31. de Ugarte Postigo, A., Fynbo, J. P. U., Thoene, C., et al. 2015, GRB Coordinates Network, Circular Service, No. 17583, #1 (2015), GRB 150314A: Redshift from OSIRIS/GTC., 17583, 1. https://gcn.nasa.gov/circulars/17583

32. Pugliese, V., Xu, D., Tanvir, N. R., et al. 2015, GRB Coordinates Network, Circular Service, No. 17672, #1 (2015), GRB 150403A: VLT/X-shooter redshift., 17672, 1. https://gcn.nasa.gov/circulars/17672

33. de Ugarte Postigo, A., Xu, D., Malesani, D., et al. 2015, GRB Coordinates Network, Circular Service, No. 17822, #1 (2015), GRB 150514A: VLT/X-shooter redshift., 17822, 1. https://gcn.nasa.gov/circulars/17822

34. Chand, V., Banerjee, A., Gupta, R., et al. 2020, The Astrophysical Journal, Peculiar Prompt Emission and Afterglow in the H.E.S.S.-detected GRB 190829A, 898, 1, 42. https://doi.org/10.3847/1538-4357/ab9606

35. Tanvir, N. R., Levan, A. J., Cenko, S. B., et al. 2016, GRB Coordinates Network, Circular Service, No. 19419, #1 (2016), GRB 160509A Gemini North redshift., 19419, 1. https://gcn.nasa.gov/circulars/19419

36. Malesani, D., de Ugarte Postigo, A., de Pasquale, M., et al. 2016, GRB Coordinates Network, Circular Service, No. 19708, #1 (2016), GRB 160623A: optical astrometry, photometry, and redshift., 19708, 1. https://gcn.nasa.gov/circulars/19708

37. Zhang, B.-B., Zhang, B., Castro-Tirado, A. J., et al. 2018, Nature Astronomy, Transition from fireball to Poynting-flux-dominated outflow in the three-episode GRB 160625B, 2, 69. https://doi.org/10.1038/s41550-017-0309-8

38. Zhang, X.-F., Liu, R.-Y., Zhang, H.-M., et al. 2025, The Astrophysical Journal, Constraints on Cosmic-Ray Acceleration in Bright Gamma-Ray Bursts with Observations of Fermi, 980, 2, 188. https://doi.org/10.3847/1538-4357/ada941

39. Kruehler, T., Schady, P., Greiner, J., et al. 2017, GRB Coordinates Network, Circular Service, No. 20686, #1 (2017), GRB 170214A: VLT/X-shooter spectroscopy and tentative redshift., 20686, 1. https://gcn.nasa.gov/circulars/20686

40. de Ugarte Postigo, A., Kann, D. A., Thoene, C. C., et al. 2017, GRB Coordinates Network, Circular Service, No. 20990, #1 (2017), GRB 170405A: Redshift from OSIRIS/GTC., 20990, 1. https://gcn.nasa.gov/circulars/20990

41. Zhang, Z. B., Zhang, C. T., Zhao, Y. X., et al. 2018, Publications of the Astronomical Society of the Pacific, Spectrum-energy Correlations in GRBs: Update, Reliability, and the Long/Short Dichotomy, 130, 987, 054202. https://doi.org/10.1088/1538-3873/aaa6af

42. Izzo, L., de Ugarte Postigo, A., Schady, P., et al. 2019, GRB Coordinates Network, Circular Service, No. 23889, #1 (2019/February-0), GRB 180703A: VLT/MUSE host galaxy redshift measurement., 23889, 1. https://gcn.nasa.gov/circulars/23889

43. Vreeswijk, P. M., Kann, D. A., Heintz, K. E., et al. 2018, GRB Coordinates Network, Circular Service, No. 22996, #1 (2018), GRB 180720B: VLT/X-shooter redshift., 22996, 1. https://gcn.nasa.gov/circulars/22996

44. Tanvir, N. R., Fynbo, J. P. U., de Ugarte Postigo, A., et al. 2019, Monthly Notices of the Royal Astronomical Society, The fraction of ionizing radiation from massive stars that escapes to the intergalactic medium, 483, 4, 5380. https://doi.org/10.1093/mnras/sty3460

45. Dainotti, M. G., Young, S., Li, L., et al. 2022, The Astrophysical Journal Supplement Series, The Optical Two- and Three-dimensional Fundamental Plane Correlations for Nearly 180 Gamma-Ray Burst Afterglows with Swift/UVOT, RATIR, and the Subaru Telescope, 261, 2, 25. https://doi.org/10.3847/1538-4365/ac7c64

46. Castro-Tirado, A. J., Hu, Y., Fernandez-Garcia, E., et al. 2019, GRB Coordinates Network, Circular Service, No. 23708, #1 (2019), GRB 190114C: refined redshift by the 10.4m GTC., 23708, 1. https://gcn.nasa.gov/circulars/23708

47. Sharma, V., Iyyani, S., & Bhattacharya, D. 2021, The Astrophysical Journal Letters, Identifying Black Hole Central Engines in Gamma-Ray Bursts, 908, 1, L2. https://doi.org/10.3847/2041-8213/abd53f

48. Li, L. 2023, The Astrophysical Journal Supplement Series, Revisiting the Spectral Energy Correlations of GRBs with Fermi Data. I. Model-wise Properties, 266, 2, 31. https://doi.org/10.3847/1538-4365/acc867

49. Fu, S.-Y., Xu, D., Lei, W.-H., et al. 2024, The Astrophysical Journal, Unveiling the Multifaceted GRB 200613A: Prompt Emission Dynamics, Afterglow Evolution, and the Host Galaxy's Properties, 974, 2, 221. https://doi.org/10.3847/1538-4357/ad6306

50. Kann, D. A., de Ugarte Postigo, A., Blazek, M., et al. 2020, GRB Coordinates Network, Circular Service, No. 28765, GRB 201020B: Redshift from GTC/OSIRIS, 28765, 1. https://gcn.nasa.gov/circulars/28765

51. Li, L. 2023, The Astrophysical Journal Supplement Series, Revisiting the Spectral Energy Correlations of GRBs with Fermi Data. I. Model-wise Properties, 266, 2, 31. https://doi.org/10.3847/1538-4365/acc867

52. Xiao, S., Xiong, S.-L., Wang, Y., et al. 2022, The Astrophysical Journal Letters, A Robust Estimation of Lorentz Invariance Violation and Intrinsic Spectral Lag of Short Gamma-Ray Bursts, 924, 2, L29. https://doi.org/10.3847/2041-8213/ac478a

53. Zhu, Z. P., Izzo, L., Fu, S. Y., et al. 2021, GRB Coordinates Network, Circular Service, No. 30692, GRB 210822A: NOT photometry and spectroscopy, 30692, 1. https://gcn.nasa.gov/circulars/30692

54. Li, L. 2023, The Astrophysical Journal Supplement Series, Revisiting the Spectral Energy Correlations of GRBs with Fermi Data. I. Model-wise Properties, 266, 2, 31. https://doi.org/10.3847/1538-4365/acc867

55. Li, L. 2023, The Astrophysical Journal Supplement Series, Revisiting the Spectral Energy Correlations of GRBs with Fermi Data. I. Model-wise Properties, 266, 2, 31. https://doi.org/10.3847/1538-4365/acc867

56. Li, L. 2023, The Astrophysical Journal Supplement Series, Revisiting the Spectral Energy Correlations of GRBs with Fermi Data. I. Model-wise Properties, 266, 2, 31. https://doi.org/10.3847/1538-4365/acc867

57. de Wet, S., Izzo, L., Groot, P. J., et al. 2023, Astronomy & Astrophysics, The ultra-long GRB 220627A at z = 3.08, 677, A32. https://doi.org/10.1051/0004-6361/202347017

58. Malesani, D. B., Levan, A. J., Izzo, L., et al. 2023, , The brightest GRB ever detected: GRB 221009A as a highly luminous event at z = 0.151, arXiv:2302.07891v2. https://doi.org/10.48550/arXiv.2302.07891

59. Hussenot-Desenonges, T., Wouters, T., Guessoum, N., et al. 2024, Monthly Notices of the Royal Astronomical Society, Multiband analyses of the bright GRB 230812B and the associated SN2023pel, 530, 1, 1. https://doi.org/10.1093/mnras/stae503

60. Martin-Carrillo, A., Schneider, B., Pugliese, G., et al. 2024, GRB Coordinates Network, Circular Service, No. 37293, GRB 240825A: VLT/X-shooter redshift, 37293, 1. https://gcn.nasa.gov/circulars/37293

Appendix B

Appendix B presents eight GRB examples from the LAT-GBM analysis and eight from the LLE-GBM analysis. For each GRB, three representative LAT/LLE energy ranges are shown. For every energy range, the corresponding cross-correlation function is displayed, along with the resulting histogram of delay values, centered around the estimated true delay.
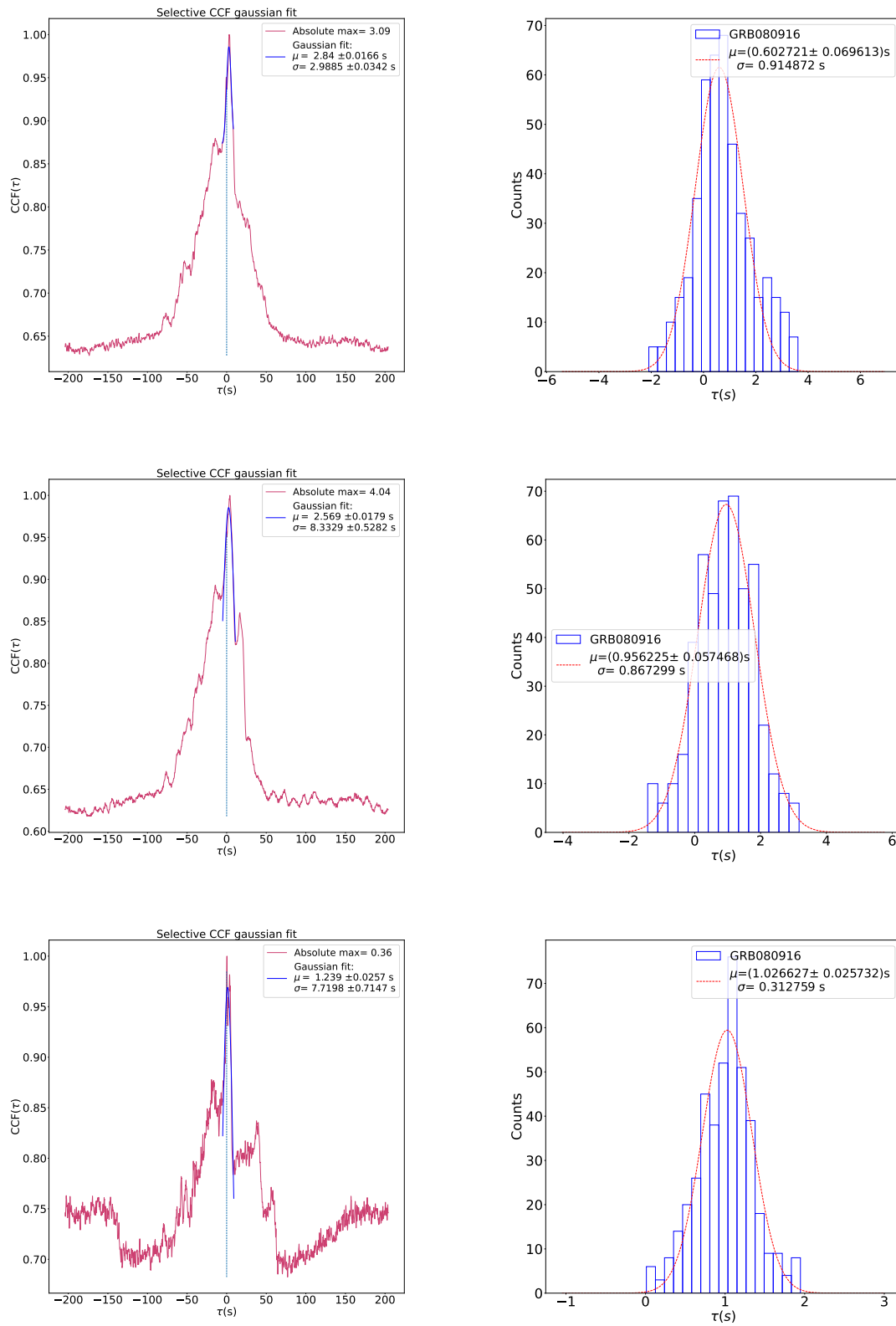
Figure 8.10: LAT-GBM analysis for GRB 080916C. LAT energy ranges used (top to bottom): 50.40–64.80 MeV, 107.12–137.72 MeV, 292.71–376.34 MeV.
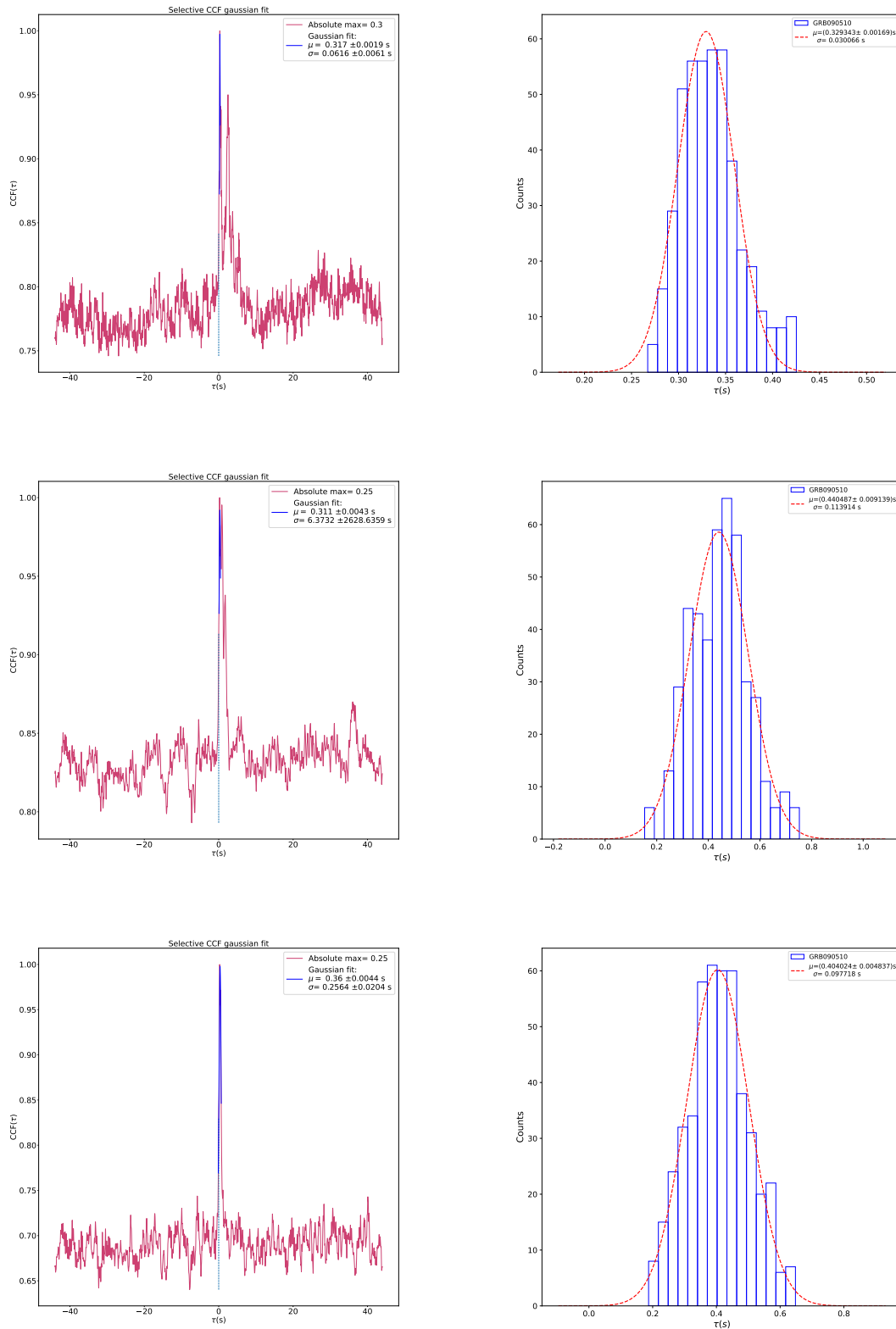
Figure 8.11: LAT-GBM analysis for GRB 090510. LAT energy ranges used (top to bottom): 52.58–67.61 MeV, 86.92–111.76 MeV, 237.53–305.39 MeV.
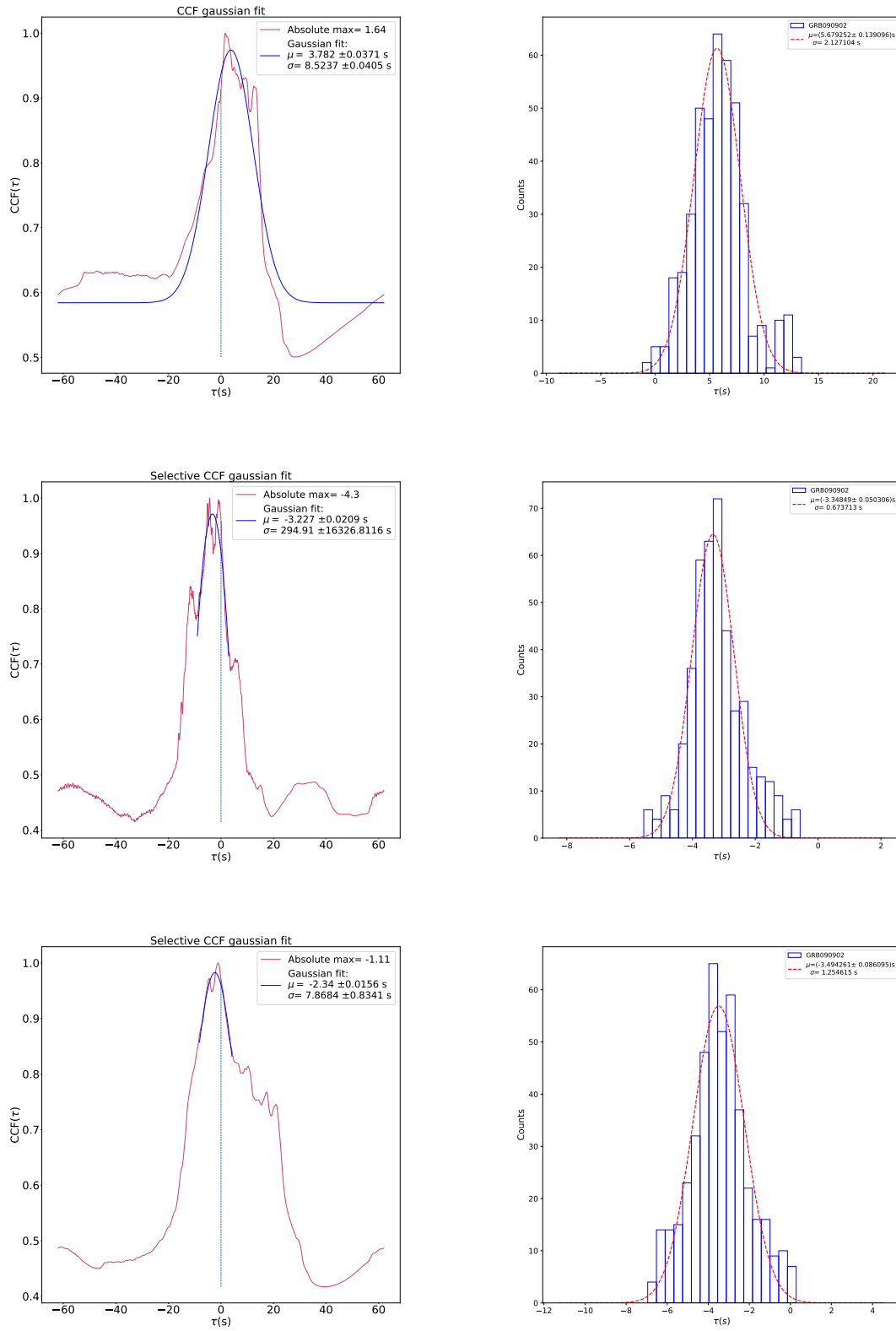
Figure 8.12: LAT-GBM analysis for GRB 090902B. LAT energy ranges used (top to bottom): 72.35–93.03 MeV, 119.61–153.78 MeV, 254.21–326.84 MeV.
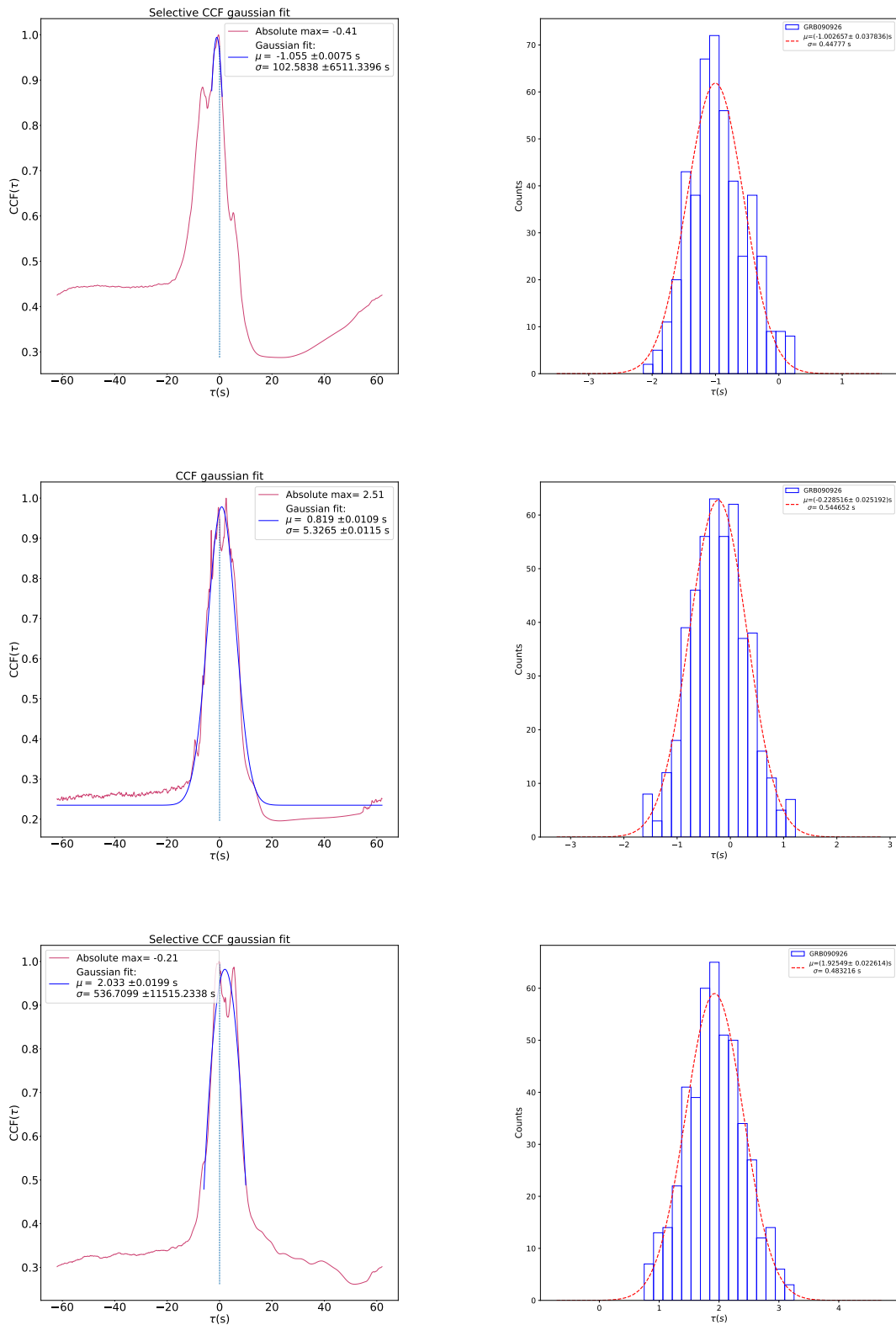
Figure 8.13: LAT-GBM analysis for GRB 090926. LAT energy ranges used (top to bottom): 39.89–51.29 MeV, 84.79–109.01 MeV, 180.20–231.69 MeV.
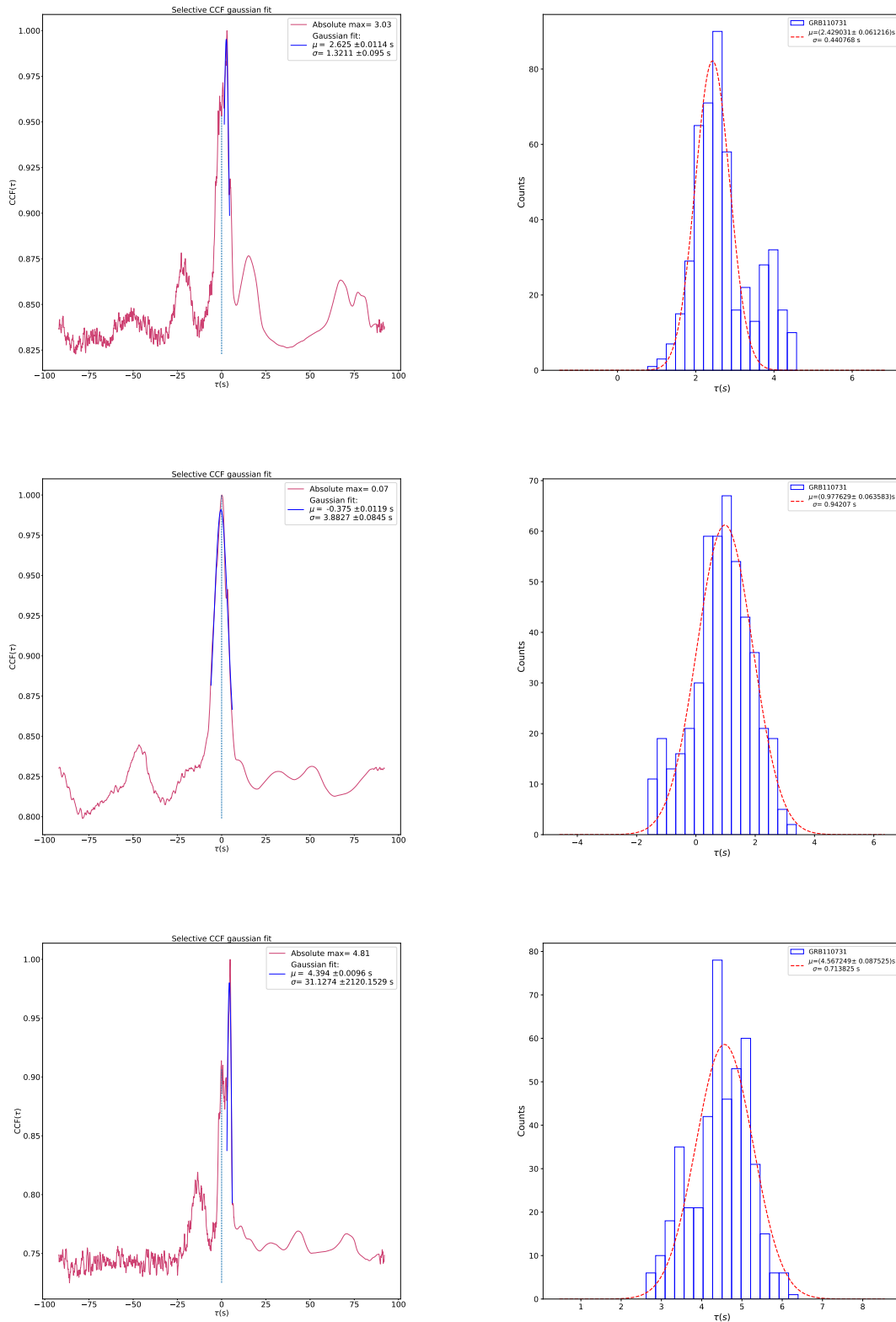
Figure 8.14: LAT-GBM analysis for GRB 110731A. LAT energy ranges used (top to bottom): 45.17–67.75 MeV, 67.75–101.63 MeV, 101.63–152.45 MeV.
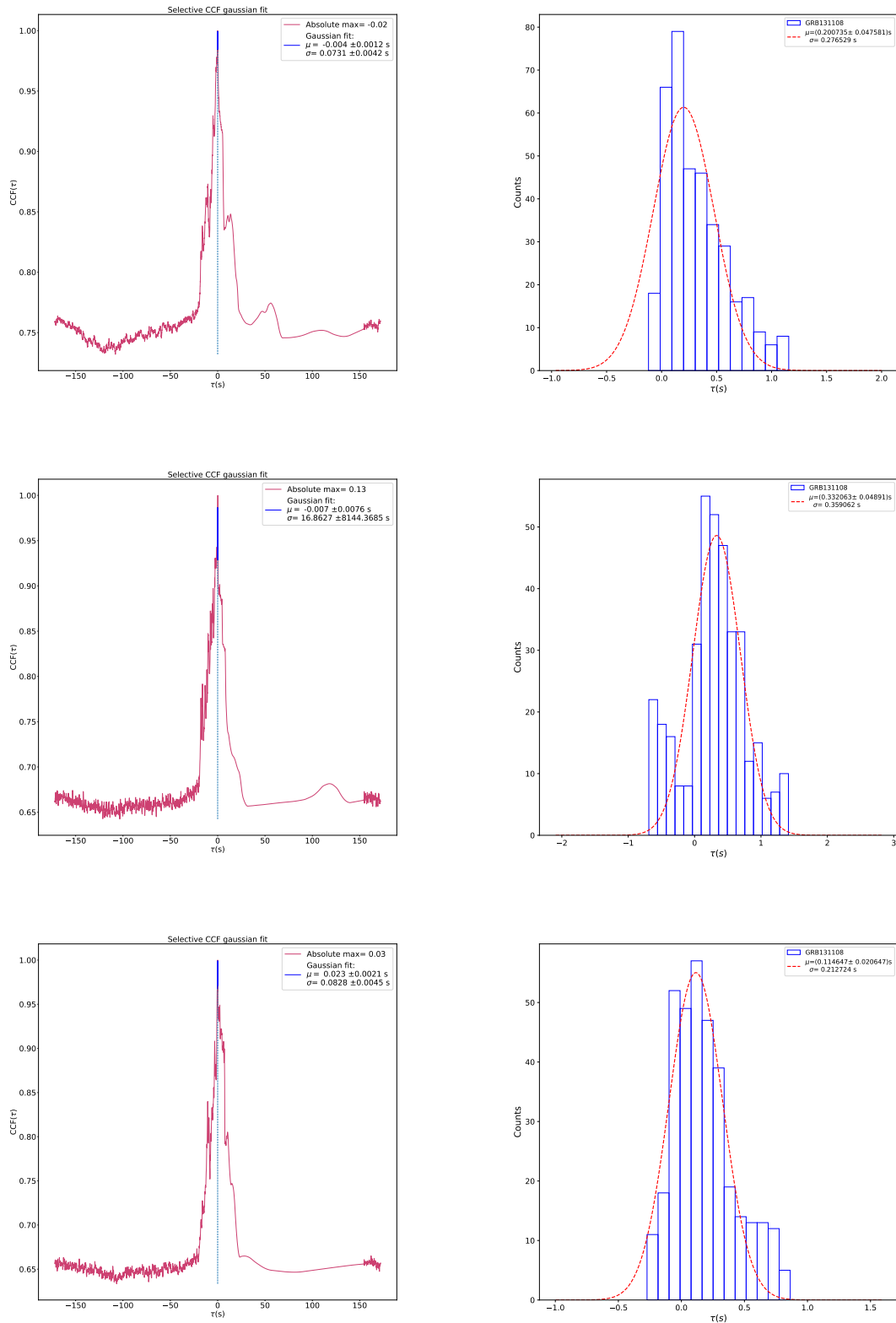
Figure 8.15: LAT-GBM analysis for GRB 131108A. LAT energy ranges used (top to bottom): 49.83–64.06 MeV, 105.90–136.16 MeV, 136.16–175.06 MeV.
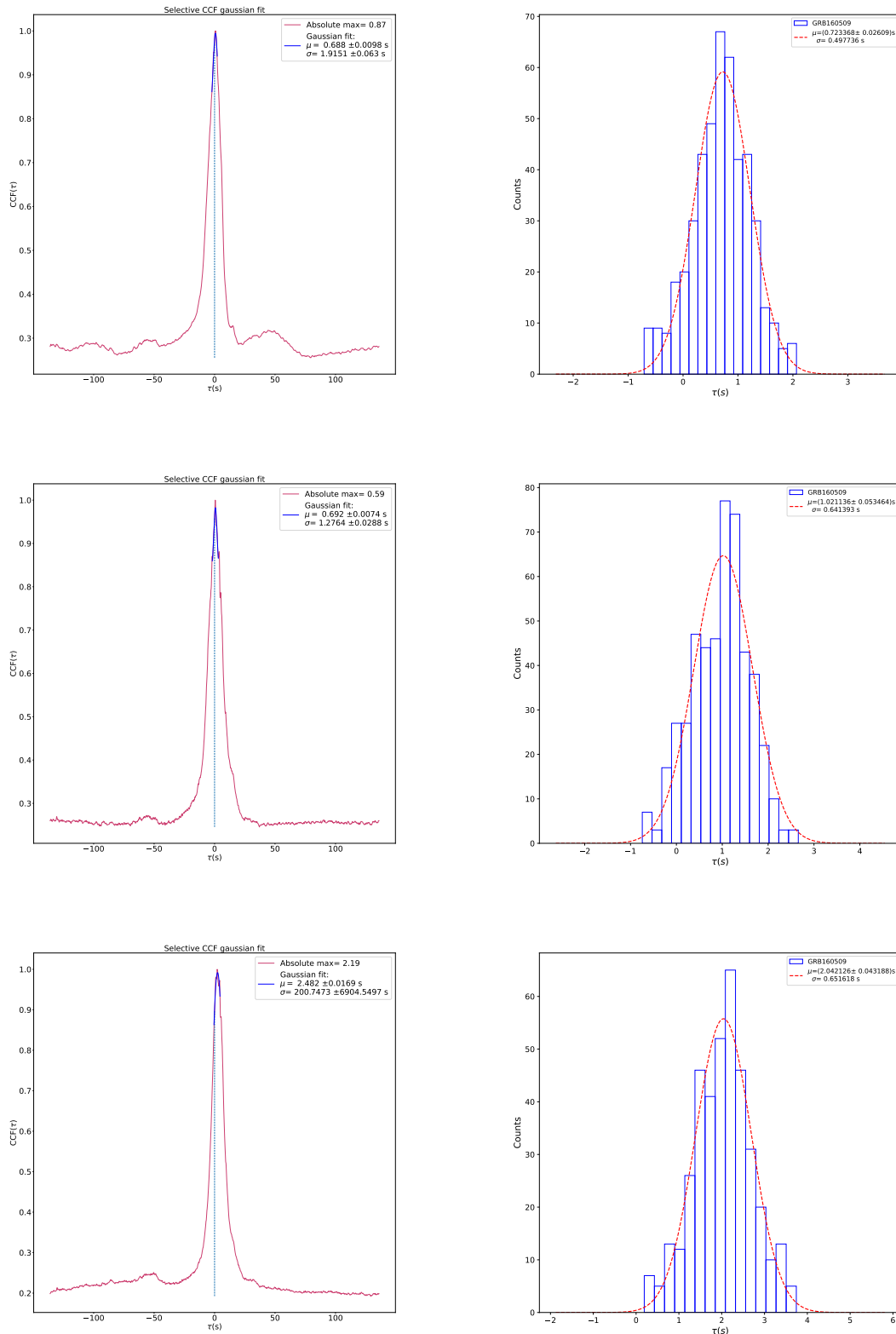
Figure 8.16: LAT-GBM analysis for GRB 160509A. LAT energy ranges used (top to bottom): 38.60–49.63 MeV, 63.81–82.04 MeV, 82.04–105.48 MeV.
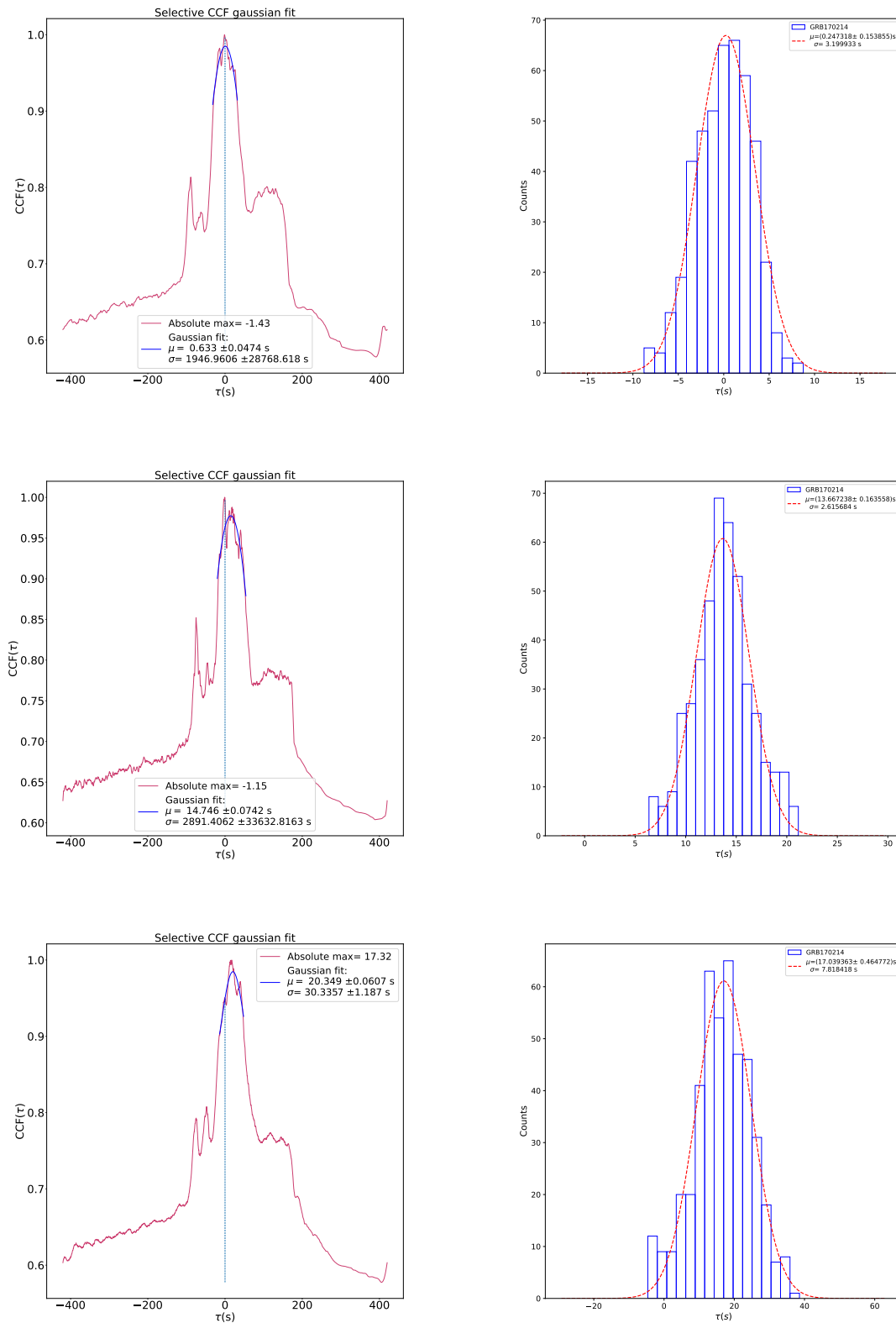
Figure 8.17: LAT-GBM analysis for GRB 170214A. LAT energy ranges used (top to bottom): 49.87–64.12 MeV, 106.00–136.28 MeV, 175.22–225.28 MeV.
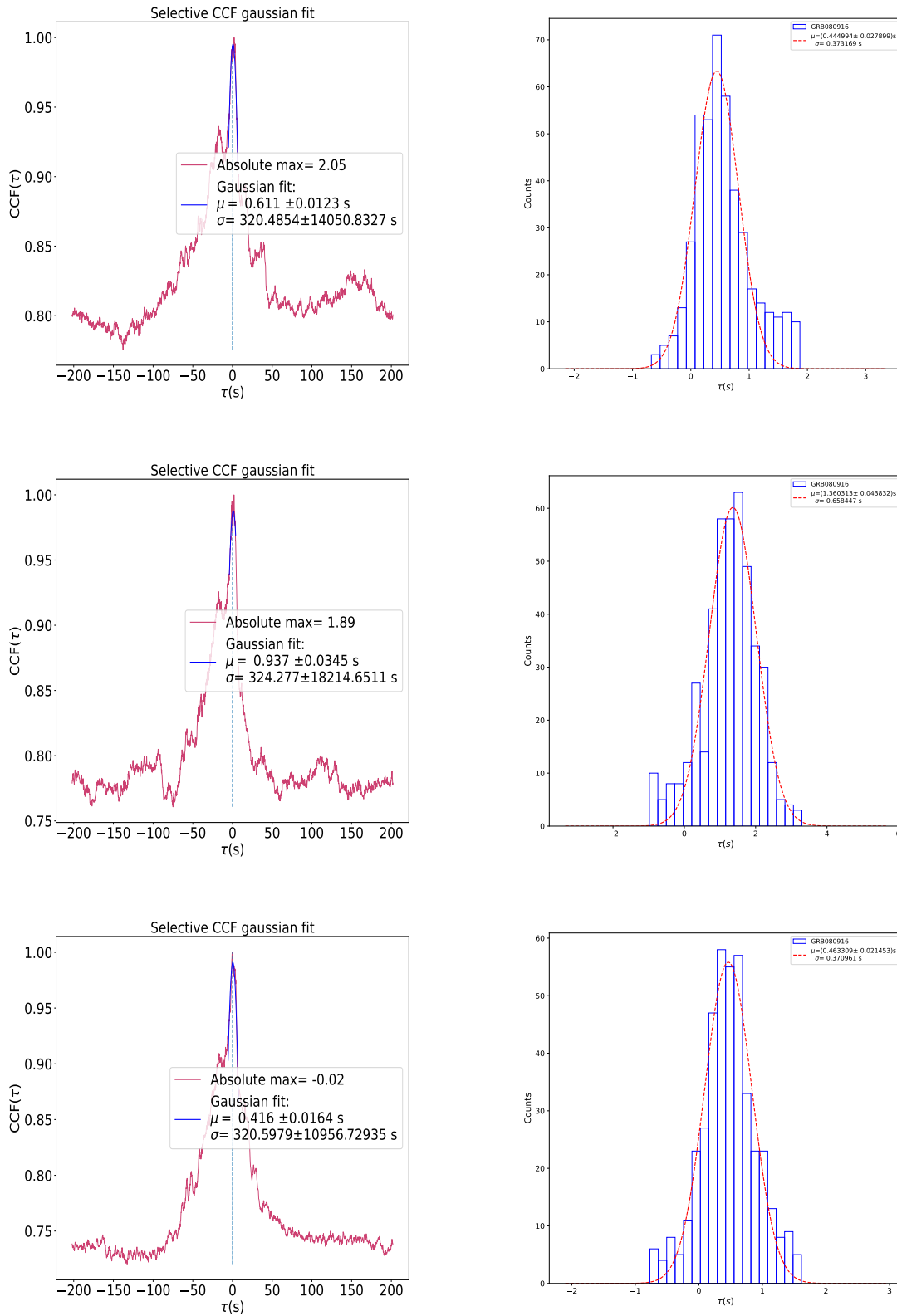
Figure 8.18: LLE-GBM analysis for GRB 080916C. LLE energy ranges used (top to bottom): 15.19–19.53 MeV, 25.11–32.28 MeV, 41.50–53.36 MeV.
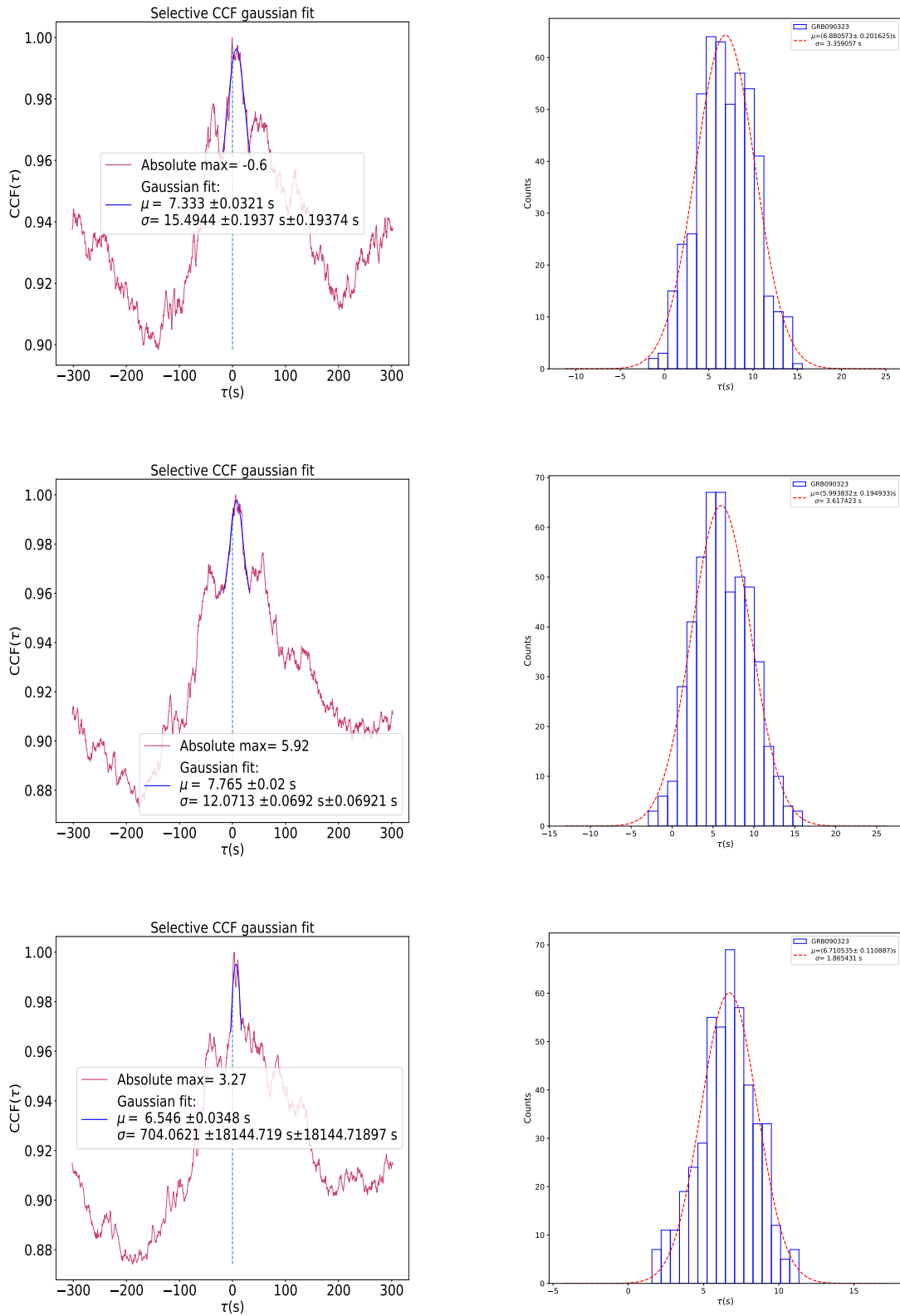
Figure 8.19: LLE-GBM analysis for GRB 090323. LLE energy ranges used (top to bottom): 10.51–13.51 MeV, 13.51–17.37 MeV, 17.37–22.33 MeV.
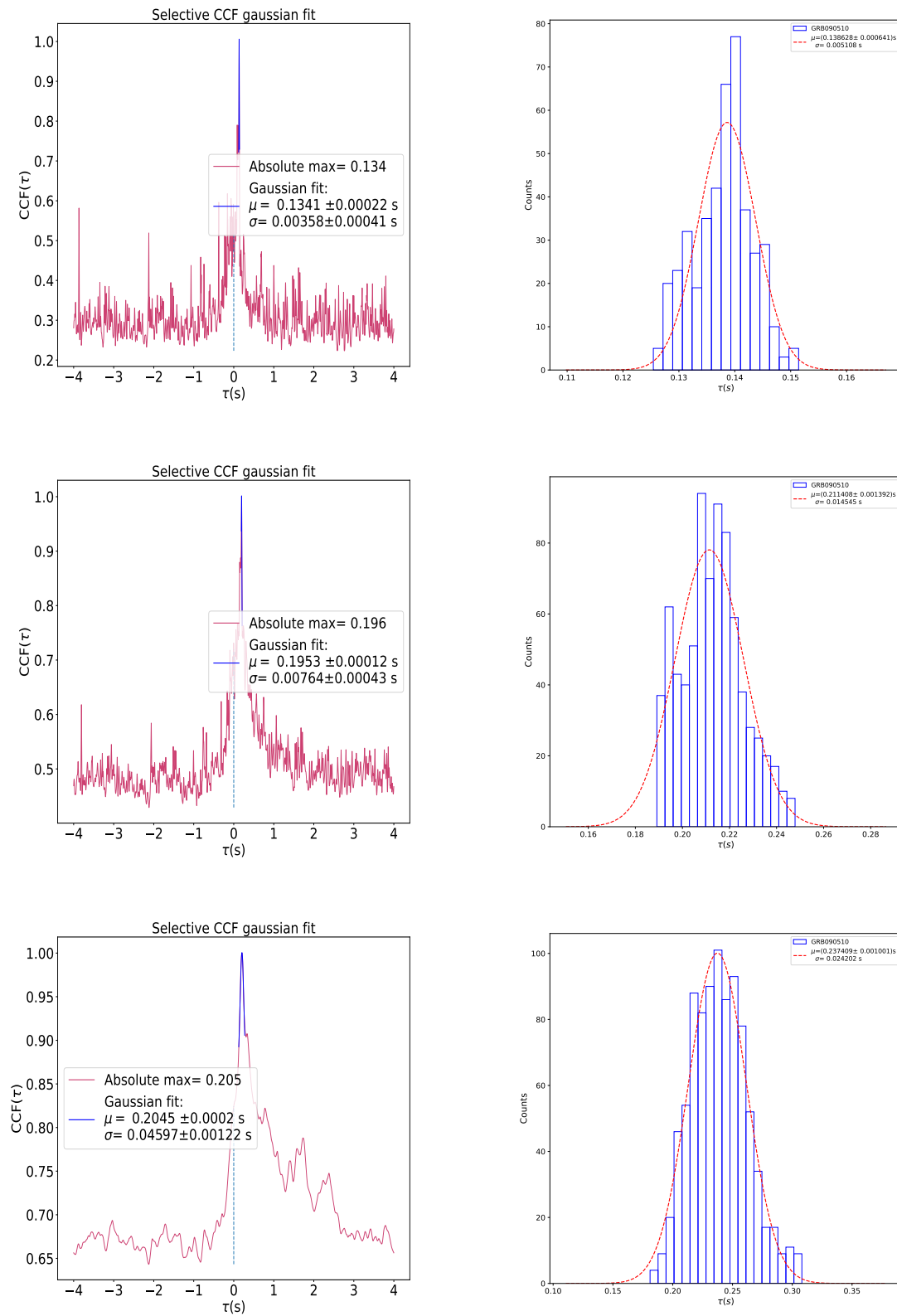
Figure 8.20: LLE-GBM analysis for GRB 090510. LLE energy ranges used (top to bottom): 12.31–15.05 MeV, 27.48–33.58 MeV, 61.31–74.94 MeV.
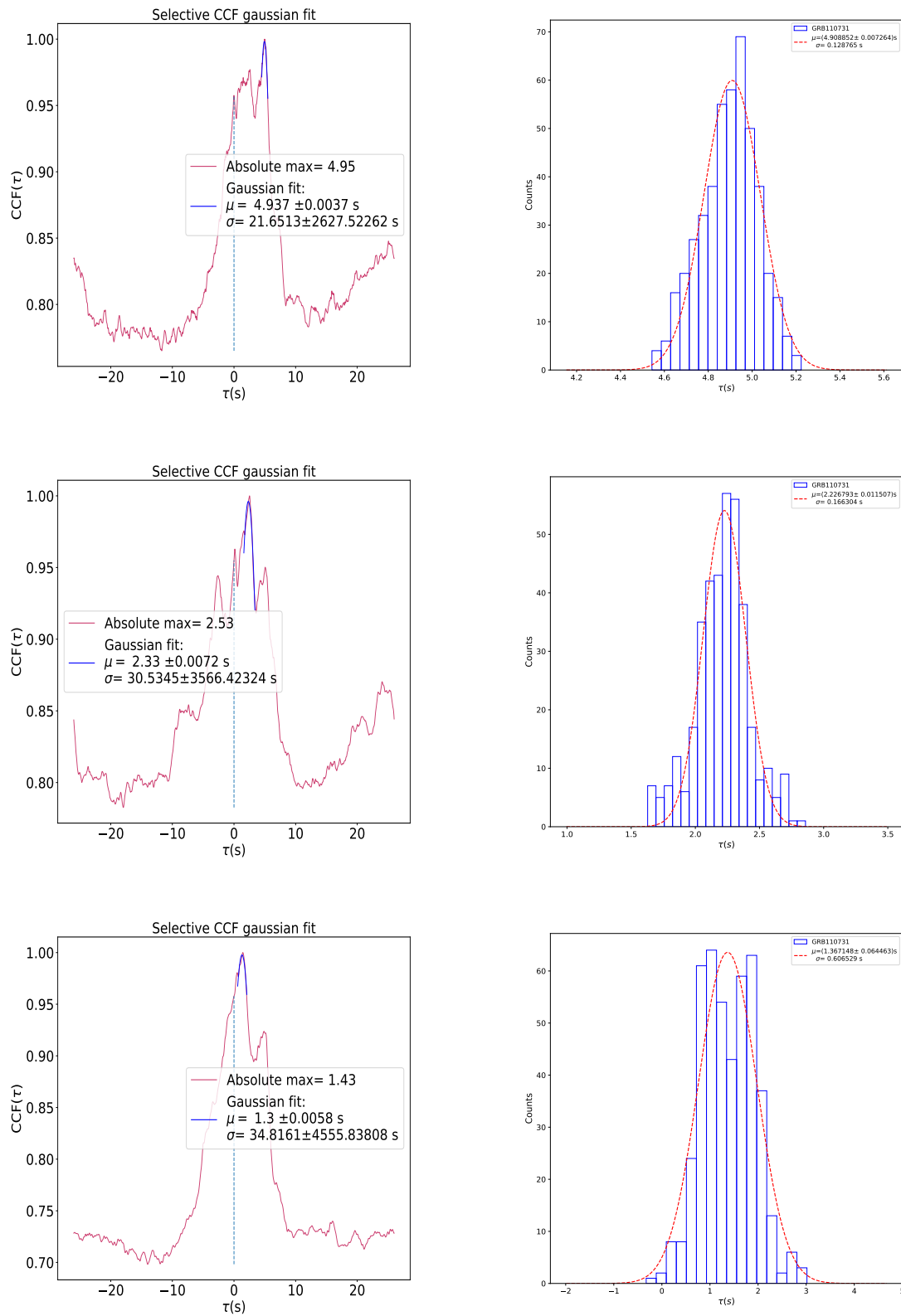
Figure 8.21: LLE-GBM analysis for GRB 110731A. LLE energy ranges used (top to bottom): 11.82–15.19 MeV, 19.54–25.12 MeV, 41.52–53.38 MeV.
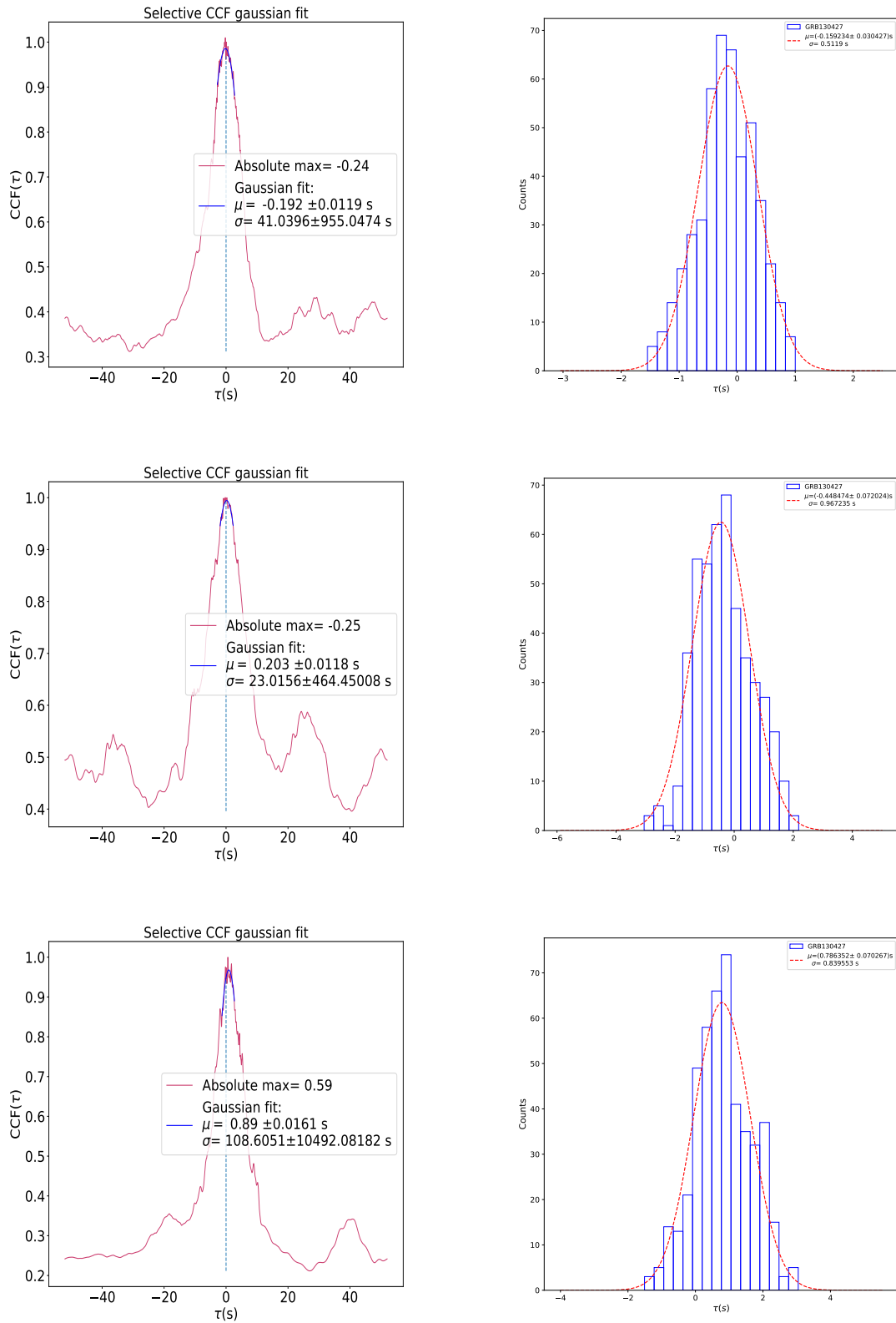
Figure 8.22: LLE-GBM analysis for GRB 130427A. LLE energy ranges used (top to bottom): 14.71–16.26 MeV, 24.27–26.82 MeV, 36.22–40.03 MeV.
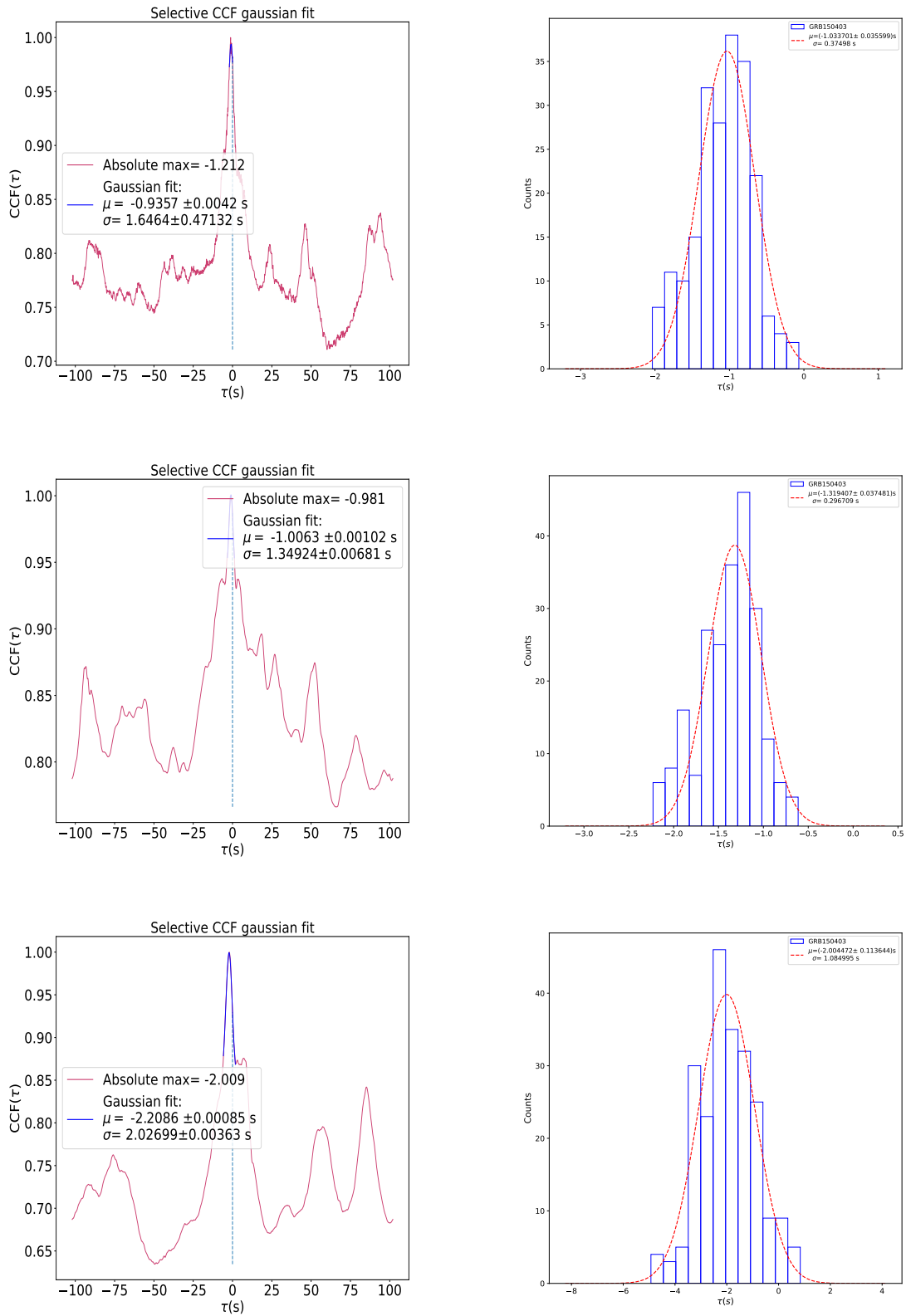
Figure 8.23: LLE-GBM analysis for GRB 150403A. LLE energy ranges used (top to bottom): 8.14–9.95 MeV, 12.17–14.87 MeV, 40.56–49.57 MeV.
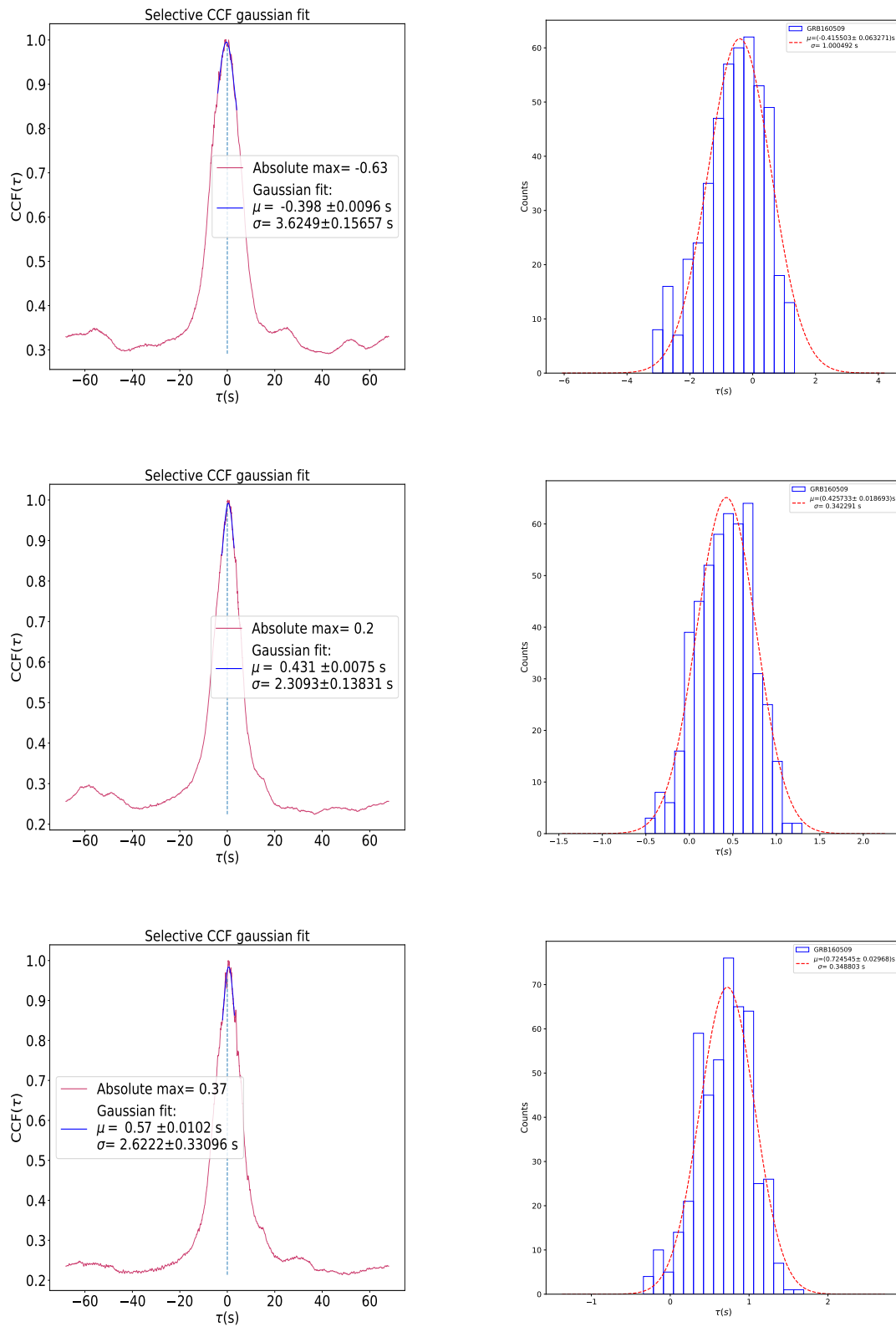
Figure 8.24: LLE-GBM analysis for GRB 160509A. LLE energy ranges used (top to bottom): 11.20–13.69 MeV, 25.00–30.55 MeV, 55.78–68.17 MeV.
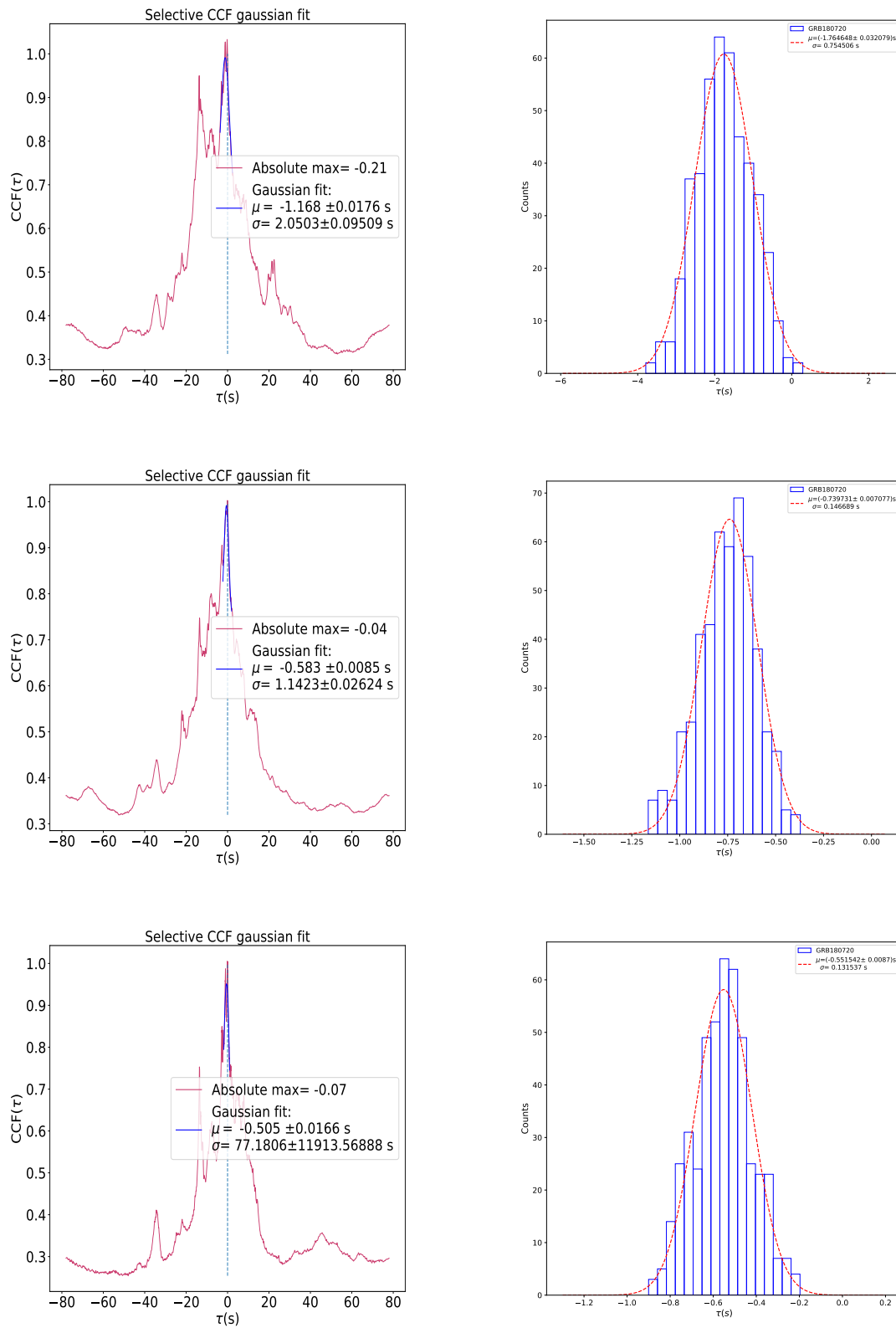
Figure 8.25: LLE-GBM analysis for GRB 180720B. LLE energy ranges used (top to bottom): 11.20–13.69 MeV, 25.00–30.56 MeV, 37.35–45.65 MeV.

Bibliography

Abbott, B. P., Abbott, R., Abbott, T. D., et al. 2016, Observation of Gravitational Waves from a Binary Black Hole Merger, 116, 6, 061102. https://doi.org/10.1103/PhysRevLett.116.061102

Abbott, B. P., Abbott, R., Abbott, T. D., et al. 2017, The Astrophysical Journal Letters, Gravitational Waves and Gamma-Rays from a Binary Neutron Star Merger: GW170817 and GRB 170817A, 848, 2, L13. https://doi.org/10.3847/2041-8213/aa920c

Abdalla, E., Abellán, G. F., Aboubrahim, A., et al. 2022, Journal of High Energy Astrophysics, Cosmology intertwined: A review of the particle physics, astrophysics, and cosmology associated with the cosmological tensions and anomalies, 34, 49. https://doi.org/10.1016/j.jheap.2022.04.002

Addazi, A., Alvarez-Muniz, J., Alves Batista, R., et al. 2022, Progress in Particle and Nuclear Physics, Quantum gravity phenomenology at the dawn of the multi-messenger era-A review, 125, 103948. https://doi.org/10.1016/j.ppnp.2022.103948

Ahumada, T., Singer, L. P., Anand, S., et al. 2021, Nature Astronomy, Discovery and confirmation of the shortest gamma-ray burst from a collapsar, 5, 917. https://doi.org/10.1038/s41550-021-01428-7

Alves Batista, R., Amelino-Camelia, G., Boncioli, D., et al. 2023, White Paper and Roadmap for Quantum Gravity Phenomenology in the Multi-Messenger Era, arXiv:2312.00409v3. https://doi.org/10.48550/arXiv.2312.00409

Alves Batista, R., Amelino-Camelia, G., Boncioli, D., et al. 2025, Classical and Quantum Gravity, White paper and roadmap for quantum gravity phenomenology in the multi-messenger era, 42, 3, 032001. https://doi.org/10.1088/1361-6382/ad605a

Amelino-Camelia, G., Ellis, J., Mavromatos, N. E., et al. 1998, Nature, Tests of quantum gravity from observations of γ-ray bursts, 395, 6701, 525. https://doi.org/10.1038/26793

Amelino-Camelia, G. 2002, Modern Physics Letters A, Quantum-Gravity Phenomenology, 17, 15-17, 899. https://doi.org/10.1142/S0217732302007612

Amelino-Camelia, G. & Ahluwalia, D. V. 2002, International Journal of Modern Physics D, Doubly-Special Relativity, 11, 10, 1643. https://doi.org/10.1142/S021827180200302X

Amelino-Camelia, G. 2005, Lecture Notes in Physics, Berlin Springer Verlag, Introduction to Quantum-Gravity Phenomenology, 669, 59. https://doi.org/10.1007/11377306_3

Amelino-Camelia, G., Freidel, L., Kowalski-Glikman, J., et al. 2011, Physical Review D, Principle of relative locality, 84, 8, 084010. https://doi.org/10.1103/PhysRevD.84.084010

Aptekar, R. L., Frederiks, D. D., Golenetskii, S. V., et al. 1995, Space Science Reviews, Konus-W Gamma-Ray Burst Experiment for the GGS Wind Spacecraft, 71, 1-4, 265. https://doi.org/10.1007/BF00751332

Asaoka, Y., Adriani, O., Akaike, Y., et al. 2019, Journal of Physics Conference Series, The CALorimetric Electron Telescope (CALET) on the International Space Station: Results from the First Two Years On Orbit, 1181, 1, 012003. https://doi.org/10.1088/1742-6596/1181/1/012003

Atwood, W. B., Abdo, A. A., Ackermann, M., et al. 2009, The Astrophysical Journal, The Large Area Telescope on the Fermi Gamma-Ray Space Telescope Mission, 697, 2, 1071. https://doi.org/10.1088/0004-637X/697/2/1071

Band, D., Matteson, J., Ford, L., et al. 1993, The Astrophysical Journal, BATSE Observations of Gamma-Ray Burst Spectra. I. Spectral Diversity, 413, 281. https://doi.org/10.1086/172995

Barbón, J. L. F. 2004, European Physical Journal C, String theory, 33, s67. https://doi.org/10.1140/epjcd/s2003-03-009-5

Berger, E. 2014, Annual Review of Astronomy and Astrophysics, Short-Duration Gamma-Ray Bursts, 52, 43. https://doi.org/10.1146/annurev-astro-081913-035926

Bernardini, M. G., Cordier, B., & Wei, J. 2021, Galaxies, The SVOM Mission, 9, 4, 113. https://doi.org/10.3390/galaxies9040113

Beurle, K., Bewick, A., Mills, J. S., et al. 1981, International Cosmic Ray Conference, Gamma-Ray Burst Measurements at Low Fluxes, 1, 88. https://articles.adsabs.harvard.edu/pdf/1981ICRC...17a..88B

Bigongiari, C., Bastieri, D., Galante, N., et al. 2004, Nuclear Instruments and Methods in Physics Research A, The MAGIC telescope reflecting surface, 518, 1-2, 193. https://doi.org/10.1016/j.nima.2003.10.058

Bigongiari, C. 2005, International Europhysics Conference on High Energy Physics, HEP2005, The MAGIC telescope, 20. https://doi.org/10.48550/arXiv.astro-ph/0512184

Burderi, L., Di Salvo, T., Riggio, A., et al. 2020, Proceedings of SPIE, GrailQuest and HERMES: hunting for gravitational wave electromagnetic counterparts and probing space-time quantum foam, 11444, 114444Y. https://doi.org/10.1117/12.2561779

Burns, E., Svinkin, D., Fenimore, E., et al. 2023, The Astrophysical Journal Letters, GRB 221009A: The Boat, 946, 1, L31. https://doi.org/10.3847/2041-8213/acc39c

Cañas-Herrera, G., Contigiani, O., & Vardanyan, V. 2020, Physical Review D, Cross-correlation of the astrophysical gravitational-wave background with galaxy clustering, 102, 4, 043513. https://doi.org/10.1103/PhysRevD.102.043513

Chakrabarti, A., Chaudhury, K., Sarkar, S. K., et al. 2018, Journal of High Energy Astrophysics, Spectral evolution of GRBs with negative spectral lag using Fermi GBM observations, 18, 15. https://doi.org/10.1016/j.jheap.2018.01.002

Chen, L., Lou, Y.-Q., Wu, M., et al. 2005, The Astrophysical Journal, Distribution of Spectral Lags in Gamma-Ray Bursts, 619, 2, 983. https://doi.org/10.1086/426774

Cheng, L. X., Ma, Y. Q., Cheng, K. S., et al. 1995, Astronomy & Astrophysics, The time delay of gamma-ray bursts in the soft energy band., 300, 746. https://articles.ads abs.harvard.edu/pdf/1995A%26A...300..746C

Clifton, T., Ferreira, P. G., Padilla, A., et al. 2012, Physics Reports, Modified gravity and cosmology, 513, 1, 1. https://doi.org/10.1016/j.physrep.2012.01.001

Connes, A. 2007, Quantum Spaces: Poincaré Seminar 2007, Non-commutative Geometry and the Spectral Model of Space-time, 53, 203. https://doi.org/10.1007/978-3-7643-8522-4_5

Costa, E., Frontera, F., Heise, J., et al. 1997, Nature, Discovery of an X-ray afterglow associated with the γ-ray burst of 28 February 1997, 387, 6635, 783. https://doi.org/10.1038/42885

Das, S. & Vagenas, E. C. 2009, Canadian Journal of Physics, Phenomenological implications of the generalized uncertainty principle, 87, 3, 233. https://doi.org/10.1139/P08-105

Ding, G. Q., Zhang, W. Y., Wang, Y. N., et al. 2016, Monthly Notices of the Royal Astronomical Society, The cross-correlation analysis in Z source GX 349+2, 455, 3, 2959. https://doi.org/10.1093/mnras/stv2459

Doplicher, S., Fredenhagen, K., & Roberts, J. E. 1995, Communications in Mathematical Physics, The quantum structure of spacetime at the Planck scale and quantum fields, 172, 1, 187. https://doi.org/10.1007/BF02104515

Ďuríšková, M. 2023, Vacuum dispersion effect on GRB, Bachelor's thesis, Masaryk University, Faculty of Science, Brno. https://is.muni.cz/th/jjj4x/

Duriskova, M., Dafcikova, M., Ripa, J., et al. 2025, GRB Coordinates Network, Circular Service, No. 39255, GRB 250204B: GRBAlpha detection, 39255, 1. https://gcn.na sa.gov/circulars/39255

Einstein, A. 1915, Sitzungsberichte der Königlich Preussischen Akademie der Wissenschaften, Die Feldgleichungen der Gravitation, 844. https://articles.ads abs.harvard.edu/pdf/1915SPAW.......844E

Ellis, J., Farakos, K., Mavromatos, N. E., et al. 2000, The Astrophysical Journal, A Search in Gamma-Ray Burst Data for Nonconstancy of the Velocity of Light, 535, 1, 139. https://doi.org/10.1086/308825

Evangelista, Y., Fiore, F., Fuschino, F., et al. 2020, Proceedings of SPIE, The scientific payload on-board the HERMES-TP and HERMES-SP CubeSat missions, 11444, 114441T. https://doi.org/10.1117/12.2561018

Event Horizon Telescope Collaboration, Akiyama, K., Alberdi, A., et al. 2019, The Astrophysical Journal Letters, First M87 Event Horizon Telescope Results. I. The Shadow of the Supermassive Black Hole, 875, 1, L1. https://doi.org/10.3847/2041-8213/ab0ec7

Faurobert, M., Ricort, G., & Aime, C. 2012, Astronomy & Astrophysics, A cross-correlation method for measuring line formation heights in the solar photosphere, 548, A80. https://doi.org/10.1051/0004-6361/201219640

Ferrigno, C. 2025, GRB Coordinates Network, Circular Service, No. 39563, INTEGRAL: end of scientific operations, 39563, 1. https://gcn.nasa.gov/circulars/39563

Fiore, F., Burderi, L., Lavagna, M., et al. 2020, Proceedings of SPIE, The HERMES-technologic and scientific pathfinder, 11444, 114441R. https://doi.org/10.1117/12.2560680

Fishman, G. J., Meegan, C. A., Watts, J. W., et al. 1978, The Astrophysical Journal Letters, New limits on gamma-ray bursts., 223, L13. https://doi.org/10.1086/182716

Fishman, G. J., Meegan, C. A., Wilson, R. B., et al. 1991, Gamma-ray Bursts, BATSE observations of gamma-ray bursts, 265, 13. https://doi.org/10.1063/1.42813

Frail, D. A., Kulkarni, S. R., Sari, R., et al. 2001, The Astrophysical Journal Letters, Beaming in Gamma-Ray Bursts: Evidence for a Standard Energy Reservoir, 562, 1, L55. https://doi.org/10.1086/338119

Galbraith, W. & Jelley, J. V. 1953, Nature, Light Pulses from the Night Sky associated with Cosmic Rays, 171, 4347, 349. https://doi.org/10.1038/171349a0

Garay, L. J. 1995, International Journal of Modern Physics A, Quantum Gravity and Minimum Length, 10, 2, 145. https://doi.org/10.1142/S0217751X95000085

Gaug, M., Garrido, D., & MAGIC Collaboration 2017, 35th International Cosmic Ray Conference (ICRC2017), Constraining Lorentz invariance violations using the Crab pulsar TeV emission, 301, 704. https://doi.org/10.22323/1.301.0704

Gehrels, N., Chincarini, G., Giommi, P., et al. 2004, The Astrophysical Journal, The Swift Gamma-Ray Burst Mission, 611, 2, 1005. https://doi.org/10.1086/422091

Giuliani, A., Mereghetti, S., Fornari, F., et al. 2008, Astronomy & Astrophysics, AGILE detection of delayed gamma-ray emission from GRB 080514B, 491, 2, L25. https://doi.org/10.1051/0004-6361:200810737

Gueta, O. 2022, 37th International Cosmic Ray Conference, The Cherenkov Telescope Array: layout, design and performance, 885. https://doi.org/10.22323/1.395.0885

Guzman, A., Pliego, S., Bayer, J., et al. 2020, Proceedings of SPIE, The Payload Data Handling Unit (PDHU) on-board the HERMES-TP and HERMES-SP CubeSat Missions, 11444, 1144450. https://doi.org/10.1117/12.2562325

Holder, J., Atkins, R. W., Badran, H. M., et al. 2006, Astroparticle Physics, The first VERITAS telescope, 25, 6, 391. https://doi.org/10.1016/j.astropartphys.2006.04.002

Hořava, P. 2009, Physical Review D, Quantum gravity at a Lifshitz point, 79, 8, 084008. https://doi.org/10.1103/PhysRevD.79.084008

Huang, Y., Hu, S., Chen, S., et al. 2022, GRB Coordinates Network, Circular Service, No. 32677, LHAASO observed GRB 221009A with more than 5000 VHE photons up to around 18 TeV, 32677, 1. https://gcn.nasa.gov/circulars/32677

Jacob, U. & Piran, T. 2008, Journal of Cosmology and Astroparticle Physics, Lorentz-violation-induced arrival delays of cosmological particles, 2008, 1, 031. https://doi.org/10.1088/1475-7516/2008/01/031

Junior, E. L. B., Rodrigues, M. E., & de S. Silva, M. V. 2020, Nuclear Physics B, Regular black holes in Rainbow Gravity, 961, 115244. https://doi.org/10.1016/j.nuclphysb.2020.115244

Klebesadel, R. W., Strong, I. B., & Olson, R. A. 1973, The Astrophysical Journal Letters, Observations of Gamma-Ray Bursts of Cosmic Origin, 182, L85. https://doi.org/10.1086/181225

Kocevski, D., Vianello, G., Omodei, N., et al. 2012, GRB Coordinates Network, Circular Service, No. 13452, #1 (2012), GRB 120711A: Fermi LAT detection., 13452, 1. https://gcn.nasa.gov/circulars/13452

Kouveliotou, C., Norris, J. P., Cline, T. L., et al. 1987, The Astrophysical Journal Letters, SMM Hard X-Ray Observations of the Soft Gamma-Ray Repeater 1806-20, 322, L21. https://doi.org/10.1086/185029

Kouveliotou, C., Meegan, C. A., Fishman, G. J., et al. 1993, The Astrophysical Journal Letters, Identification of Two Classes of Gamma-Ray Bursts, 413, L101. https://doi.org/10.1086/186969

Kowalski-Glikman, J. & Nowak, S. 2003, Classical and Quantum Gravity, Doubly special relativity and de Sitter space, 20, 22, 4799. https://doi.org/10.1088/0264-9381/20/22/006

Kováčik, S. & Prešnajder, P. 2013, Journal of Mathematical Physics, The velocity operator in quantum mechanics in noncommutative space, 54, 10, 102103. https://doi.org/10.1063/1.4826355

Kováčik, S., Ďuríšková, M., & Rusnák, P. 2025, International Journal of Modern Physics A, Phenomenology of the dispersion law in a three-dimensional quantum space, 40, 1, 2450154. https://doi.org/10.1142/S0217751X24501549

Kulkarni, S. R., Djorgovski, S. G., Ramaprakash, A. N., et al. 1998, Nature, Identification of a host galaxy at redshift z = 3.42 for the γ-ray burst of 14 December 1997, 393, 6680, 35. https://doi.org/10.1038/29927

Levy, C., Sol, H., & Bolmont, J. 2022, 37th International Cosmic Ray Conference, Modeling intrinsic time-lags in flaring blazars in the context of Lorentz Invariance Violation searches, 907. https://doi.org/10.22323/1.395.0907

Li, H. & Ma, B.-Q. 2023, Astroparticle Physics, Lorentz invariance violation induced threshold anomaly versus very-high energy cosmic photon emission from GRB 221009A, 148, 102831. https://doi.org/10.1016/j.astropartphys.2023.102831

Lyutikov, M. & Blandford, R. 2003, Gamma Ray Bursts as Electromagnetic Outflows, arXiv:astro-ph/0312347v1. https://doi.org/10.48550/arXiv.astro-ph/0312347

Maggiore, M. 1993, Physics Letters B, A generalized uncertainty principle in quantum gravity, 304, 1-2, 65. https://doi.org/10.1016/0370-2693(93)91401-8

Majhi, B. R. & Vagenas, E. C. 2013, Physics Letters B, Modified dispersion relation, photon's velocity, and Unruh effect, 725, 4-5, 477. https://doi.org/10.1016/j.physletb.2013.07.039

Matthews, J. 2005, Astroparticle Physics, A Heitler model of extensive air showers, 22, 5-6, 387. https://doi.org/10.1016/j.astropartphys.2004.09.003

Meegan, C. A., Fishman, G. J., Wilson, R. B., et al. 1991, International Astronomical Union Circulars, Gamma-Ray Bursts, 5358, 2. https://ui.adsabs.harvard.edu/abs/1991IAUC.5358....2M

Meegan, C., Lichti, G., Bhat, P. N., et al. 2009, The Astrophysical Journal, The Fermi Gamma-ray Burst Monitor, 702, 1, 791. https://doi.org/10.1088/0004-637X/702/1/791

Metzger, M. R., Djorgovski, S. G., Kulkarni, S. R., et al. 1997, Nature, Spectral constraints on the redshift of the optical counterpart to the γ-ray burst of 8 May 1997, 387, 6636, 878. https://doi.org/10.1038/43132

Mészáros, A. & Řípa, J. 2019, High-mass X-ray Binaries: Illuminating the Passage from Massive Binaries to Merging Compact Objects, Gamma-ray bursts: A brief survey of the diversity, 346, 383. https://doi.org/10.1017/S1743921319000036

Misner, C. W., Thorne, K. S., & Wheeler, J. A. 1973, Gravitation, W. H. Freeman and Company, San Francisco. `https://ui.adsabs.harvard.edu/abs/1973grav.book.....M`

Massachusetts Institute of Technology. 2008, Signal Processing – Continuous and Discrete, Lecture 22, Department of Mechanical Engineering. `https://ocw.mit.edu/courses/2-161-signal-processing-continuous-and-discrete-fall-2008/resources/lecture_22/`

Mostafa, M. & HAWC Collaboration 2016, APS April Meeting Abstracts, The High Altitude Water Cherenkov Observatory, 2016, E13.005. `https://ui.adsabs.harvard.edu/abs/2016APS..APRE13005M`

Niedermaier, M. & Reuter, M. 2006, Living Reviews in Relativity, The Asymptotic Safety Scenario in Quantum Gravity, 9, 1, 5. `https://doi.org/10.12942/lrr-2006-5`

Norris, J. P., Marani, G. F., & Bonnell, J. T. 2000, The Astrophysical Journal, Connection between Energy-dependent Lags and Peak Luminosity in Gamma-Ray Bursts, 534, 1, 248. `https://doi.org/10.1086/308725`

Norris, J. P., Scargle, J. D., & Bonnell, J. T. 2001, Gamma-ray Bursts in the Afterglow Era, Short Gamma-Ray Bursts Are Different, 40. `https://doi.org/10.1007/10853853_9`

Pál, A., Ohno, M., Mészáros, L., et al. 2020, Proceedings of SPIE, GRBAlpha: a 1U Cube-Sat mission for validating timing-based gamma-ray burst localization, 11444, 114444V. `https://doi.org/10.1117/12.2561351`

Pál, A., Ohno, M., Mészáros, L., et al. 2023, Astronomy & Astrophysics, GRBAlpha: The smallest astrophysical space observatory. I. Detector design, system description, and satellite operations, 677, A40. `https://doi.org/10.1051/0004-6361/202346182`

Peng, Z. Y., Yin, Y., Bi, X. W., et al. 2011, Astronomische Nachrichten, Spectral lag of gamma-ray bursts caused by the intrinsic spectral evolution and the curvature effect, 332, 1, 92. `https://doi.org/10.1002/asna.201011474`

Perez, A. 2013, Living Reviews in Relativity, The Spin-Foam Approach to Quantum Gravity, 16, 1, 3. `https://doi.org/10.12942/lrr-2013-3`

Piran, T. 1999, Physics Reports, Gamma-ray bursts and the fireball model, 314, 6, 575. `https://doi.org/10.1016/S0370-1573(98)00127-6`

Piran, T. 2004, Reviews of Modern Physics, The physics of gamma-ray bursts, 76, 4, 1143. `https://doi.org/10.1103/RevModPhys.76.1143`

Planck, M. 1900, Annalen der Physik, Ueber irreversible Strahlungsvorgänge, 306, 1, 69. `https://doi.org/10.1002/andp.19003060105`

Planck Collaboration, Aghanim, N., Akrami, Y., et al. 2020, Astronomy & Astrophysics, Planck 2018 results. VI. Cosmological parameters, 641, A6. https://doi.org/10.1051/0004-6361/201833910

Pühlhofer, G., Leuschner, F., & Salzmann, H. 2023, Handbook of X-ray and Gamma-ray Astrophysics, H.E.S.S.: The High Energy Stereoscopic System, 142. https://doi.org/10.1007/978-981-16-4544-0_69-1

Qin, Y.-P., Zhang, Z.-B., Zhang, F.-W., et al. 2004, The Astrophysical Journal, Characteristics of Profiles of Gamma-Ray Burst Pulses Associated with the Doppler Effect of Fireballs, 617, 1, 439. https://doi.org/10.1086/425335

Rastinejad, J. C., Fong, W., Kilpatrick, C. D., et al. 2021, The Astrophysical Journal, Probing Kilonova Ejecta Properties Using a Catalog of Short Gamma-Ray Burst Observations, 916, 2, 89. https://doi.org/10.3847/1538-4357/ac04b4

Řípa, J., Takahashi, H., Fukazawa, Y., et al. 2023, Astronomy & Astrophysics, The peak flux of GRB 221009A measured with GRBAlpha, 677, L2. https://doi.org/10.1051/0004-6361/202346128

Rovelli, C. 1998, Living Reviews in Relativity, Loop Quantum Gravity, 1, 1, 1. https://doi.org/10.12942/lrr-1998-1

Ryde, F. 2005, The Astrophysical Journal Letters, Is Thermal Emission in Gamma-Ray Bursts Ubiquitous?, 625, 2, L95. https://doi.org/10.1086/431239

Sakamoto, T., Hill, J. E., Yamazaki, R., et al. 2007, The Astrophysical Journal, Evidence of Exponential Decay Emission in the Swift Gamma-Ray Bursts, 669, 2, 1115. https://doi.org/10.1086/521640

Sanna, A., Burderi, L., Di Salvo, T., et al. 2020, Proceedings of SPIE, Timing techniques applied to distributed modular high-energy astronomy: the H.E.R.M.E.S. project, 11444, 114444X. https://doi.org/10.1117/12.2561758

Sari, R., Piran, T., & Narayan, R. 1998, The Astrophysical Journal Letters, Spectra and Light Curves of Gamma-Ray Burst Afterglows, 497, 1, L17. https://doi.org/10.1086/311269

Saridakis, E. N., Lazkoz, R., Salzano, V., et al. 2021, Modified Gravity and Cosmology: An Update by the CANTATA Network, eds. E. N. Saridakis, R. Lazkoz, V. Salzano, P. V. Moniz, S. Capozziello, J. Beltrán Jiménez, M. De Laurentis, & G. J. Olmo, Springer International Publishing, Cham. https://doi.org/10.1007/978-3-030-83715-0

Sarkar, S. 2002, Modern Physics Letters A, Possible Astrophysical Probes of Quantum Gravity, 17, 15-17, 1025. https://doi.org/10.1142/S0217732302007521

Schaefer, B. E. 2004, The Astrophysical Journal, Explaining the Gamma-Ray Burst Lag/Luminosity Relation, 602, 1, 306. https://doi.org/10.1086/380898

Shen, R.-F., Song, L.-M., & Li, Z. 2005, Monthly Notices of the Royal Astronomical Society, Spectral lags and the energy dependence of pulse width in gamma-ray bursts: contributions from the relativistic curvature effect, 362, 1, 59. https://doi.org/10.1111/j.1365-2966.2005.09163.x

Singh, K. P., Tandon, S. N., Agrawal, P. C., et al. 2014, Proceedings of SPIE, ASTROSAT mission, 9144, 91441S. https://doi.org/10.1117/12.2062667

Surya, S. 2019, Living Reviews in Relativity, The causal set approach to quantum gravity, 22, 1, 5. https://doi.org/10.1007/s41114-019-0023-1

Tam, P. H. T., Li, K. L., & Kong, A. K. H. 2012, GRB Coordinates Network, Circular Service, No. 13444, #1 (2012), GRB 120711A: Fermi LAT detection., 13444, 1. https://gcn.nasa.gov/circulars/13444

Terzić, T., Kerszberg, D., & Strišković, J. 2021, Universe, Probing Quantum Gravity with Imaging Atmospheric Cherenkov Telescopes, 7, 9, 345. https://doi.org/10.3390/universe7090345

Thompson, D. J. & Wilson-Hodge, C. A. 2022, Handbook of X-ray and Gamma-ray Astrophysics, Fermi Gamma-Ray Space Telescope, 29. https://doi.org/10.1007/978-981-16-4544-0_58-1

Tridon, D. B., Schweizer, T., Goebel, F., et al. 2010, Nuclear Instruments and Methods in Physics Research A, The MAGIC-II gamma-ray stereoscopic telescope system, 623, 1, 437. https://doi.org/10.1016/j.nima.2010.03.028

Tsvetkova, A., Frederiks, D., Golenetskii, S., et al. 2017, The Astrophysical Journal, The Konus-Wind Catalog of Gamma-Ray Bursts with Known Redshifts. I. Bursts Detected in the Triggered Mode, 850, 2, 161. https://doi.org/10.3847/1538-4357/aa96af

Veres, P., Burns, E., Bissaldi, E., et al. 2022, GRB Coordinates Network, Circular Service, No. 32636, GRB 221009A: Fermi GBM detection of an extraordinarily bright GRB, 32636, 1. https://gcn.nasa.gov/circulars/32636

Wald, R. M. 1984, General Relativity, University of Chicago Press, Chicago. https://doi.org/10.7208/chicago/9780226870373.001.0001

Wang, C.-W., Xiong, S.-L., & GECAM Team 2024, GRB Coordinates Network, Circular Service, No. 35520, GRB 240112A: GECAM detection of a burst, 35520, 1. https://gcn.nasa.gov/circulars/35520

Wei, J.-J. & Wu, X.-F. 2021, Frontiers of Physics, Testing fundamental physics with astrophysical transients, 16, 4, 44300. https://doi.org/10.1007/s11467-021-1049-x

Winkler, C., Courvoisier, T. J.-L., Di Cocco, G., et al. 2003, Astronomy & Astrophysics, The INTEGRAL mission, 411, L1. https://doi.org/10.1051/0004-6361:20031288

Woosley, S. E. 1993, The Astrophysical Journal, Gamma-Ray Bursts from Stellar Mass Accretion Disks around Black Holes, 405, 273. https://doi.org/10.1086/172359

Zajaček, M., Czerny, B., Martinez-Aldama, M. L., et al. 2020, The Astrophysical Journal, Time-delay Measurement of Mg II Broad-line Response for the Highly Accreting Quasar HE 0413-4031: Implications for the Mg II-based Radius-Luminosity Relation, 896, 2, 146. https://doi.org/10.3847/1538-4357/ab94ae

Zhang, B. 2025, Journal of High Energy Astrophysics, On the duration of gamma-ray bursts, 45, 325. https://doi.org/10.1016/j.jheap.2024.12.013

Zhang, B. 2014, International Journal of Modern Physics D, Gamma-Ray Burst Prompt Emission, 23, 2, 1430002. https://doi.org/10.1142/S021827181430002X

Zhu, J. & Ma, B.-Q. 2023, Journal of Physics G Nuclear Physics, Light speed variation from GRB 221009A, 50, 6, 06LT01. https://doi.org/10.1088/1361-6471/accebb

Electronic sources

[e1] en.es-static.us (March 3, 2025)

[e2] iopscience.iop.org (March 4, 2025)